^{222}Rn activity in soil gas as an indicator of active creep processes on geological faults

Dissertation

Zur Erlangung des Doktorgrades der Naturwissenschaften im Fachbereich
Geowissenschaften der Universität Hamburg

vorgelegt von

Nadine M. Künze
aus
Freiburg im Breisgau

Hamburg

2012

Als Dissertation angenommen vom Fachbereich Geowissenschaften der Universität Hamburg

Aufgrund der Gutachten von Prof. Dr. Claus-Dieter Reuther

Dr. Margarita Koroleva

Hamburg, den 26.06.2012

Prof. Dr. Jürgen Oßenbrügge

Leiter des Fachbereichs Geowissenschaften

Zusammenfassung

Die Messung von ^{222}Rn-Aktivitäten in der Bodenluft findet verbreitet Anwendung in der Auffindung, Identifizierung und Lokalisierung aktiver geologischer Störungen. Erhöhte ^{222}Rn-Konzentrationen in der Bodenluft sind mit seismischen Ereignissen sowie Kriechprozessen an Verwerfungen korrelierbar. In der vorliegenden Dissertation wurden ^{222}Rn-Messungen in der oberflächennahen Bodenluft in Nordspanien und Norddeutschland durchgeführt, um genetisch unterschiedliche Bruchstrukturen im Untergrund zu detektieren. Die gewählten Strukturen wurden im Rahmen dieser Dissertation erstmals auf ihre ^{222}Rn-Aktivität untersucht.

Im südlichen Kantabrischen Gebirge, NW Spanien, wurden zwei Messkampagnen durchgeführt. In der ersten Messkampagne (Sommer) wurde die ^{222}Rn-Aktivität in der Bodenluft über der seismisch aktiven Ventaniella Störung (VF) und der seismisch inaktiven Sabero-Gordón Störung (SGF) gemessen. Beide Verwerfungen zeigen erhöhte ^{222}Rn-Aktivitäten. Über der seismisch inaktiven SGF wurden im Vergleich zur VF unerwartet hohe ^{222}Rn-Aktivitäten festgestellt. In der zweiten Messkampagne (Herbst) fand eine detaillierte Untersuchung eines Segmentes der SGF statt. Im Arbeitsgebiet Nordspanien wurde ferner eine quantitative Paläospannungsanalyse durchgeführt, die auf der Aufnahme und Analyse von Störungsflächen und assoziierten kinematischen Indikatoren wie Harnischen beruht, um die Deformationsgeschichte der untersuchten Strukturen bis zur Gegenwart zu erfassen. Die resultierenden Richtungen der jüngsten horizontalen kompressiven Hauptspannung sind N–S bis NW–SE orientiert. Unter den ermittelten rezenten und bekannten aktuellen Spannungen ist die SGF potentiell aktiv. Die Ergebnisse dieser Arbeit weisen die SGF als aktive aseismische Verwerfung aus.

In Schleswig-Holstein sind auf der deutschen ^{222}Rn-Karte lokal erhöhte ^{222}Rn-Konzentrationen verzeichnet, die bisher auf Radionuklid-reiche, glaziale Ablagerungen der Weichselzeit zurückgeführt wurden. Der Beitrag aktiver tektonischer Strukturen zum ^{222}Rn-Signal in der Bodenluft wurde bisher jedoch nicht erforscht. Deshalb wurde die ^{222}Rn-Aktivität in der Bodenluft gezielt über den Randbereichen aktiver Salzstrukturen gemessen. Um den Einfluss glazialer Ablagerungen abzugrenzen, wurden ^{222}Rn-Aktivitäten von Bodenluftproben eines Bereichs hoher glazialer Granitvorkommen als Referenzwerte bestimmt. Die ^{222}Rn-Profile, die über den aktiven Salzstrukturen Bad Segeberg-Sülberg und Siek erstellt wurden, zeigen Zonen höherer ^{222}Rn-Aktivität verglichen mit den Aktivitäten, die durch glaziale Ablagerungen hervorgerufen werden.

Neben ^{222}Rn-Messungen in der Bodenluft wurden in beiden Arbeitsgebieten die petrophysikalischen Eigenschaften des Bodens sowie die meteorologischen Bedingungen bestimmt und dokumentiert. Die Ergebnisse dieser Arbeit zeigen keine Korrelation der ^{222}Rn-Werte mit den petrophysikalischen

Größen und meteorologischen Bedingungen. Durch zeitlich versetzte Messungen am gleichen Ort konnten Zonen erhöhter Konzentrationen wiederholt detektiert werden. Ein geringfügiger Versatz der ^{222}Rn-Maximumpositionen, sowie eine Variation in der Höhe der ^{222}Rn-Konzentrationen deuten auf einen strukturell induzierten Beitrag zum gemessenen Signal hin. Deformation führt zu einer Vergrößerung der Gesteinsoberfläche und damit zu erhöhter ^{222}Rn-Emanation. Aseismische Bewegungen können im Falle der SGF zur Bildung erhöhter Wegsamkeiten führen, die eine erhöhte Gasmigration ermöglichen und somit hohe ^{222}Rn-Gehalte in der oberflächen-nahen Bodenluft verursachen. Die Hypothese der aseismischen Bewegung der SGF wird von den Ergebnissen der quantitativen Paläospannungsanalyse untermauert.

Für drei repräsentative ^{222}Rn-Profile, die über der SGF und der Bad Segeberg-Sülberg Salzstruktur beprobt wurden, wurden zusätzlich die Mutternuklidgehalte (^{226}Ra) im Boden bestimmt. Der Verlauf der ^{222}Rn- und der ^{226}Ra-Aktivitäten über den untersuchten Strukturen zeigt sowohl korrelierende also auch nicht-korrelierende Trends. Die Ergebnisse legen nahe, dass die Definition von ^{222}Rn-Anomalien anhand des geochemischen Grenzwerts, der auf der ^{226}Ra-Konzentration des Bodens und den petrophysikalischen Bodeneigenschaften beruht, überdacht werden muss.

Im Rahmen dieser Dissertation wurden relevante Prozesse, die zu erhöhten ^{222}Rn-Konzentrationen im Bereich von Salzstockrandstrukturen beitragen, in einem theoretischen Modell zusammengefasst. Die Ergebnisse dieser Dissertation geben einen ersten Ansatz hinsichtlich des Beitrags aktiver Salztektonik zur ^{222}Rn-Aktivität in der Bodenluft. Die Daten, die im Laufe dieser Dissertation erhoben wurden, untermauern die Anwendbarkeit von ^{222}Rn-Messungen um tektonisch aktive Strukturen im Untergrund, die sich durch aseismisches Kriechen bewegen, zu erfassen.

Abstract

The measurement of ^{222}Rn activity in soil gas is frequently applied for the detection, identification and localization of active geological faults. Elevated concentrations of ^{222}Rn in soil gas are known to be associated with seismic activity and creep processes on faults. In this thesis, ^{222}Rn in soil gas surveys were successfully applied to trace subsurface geological fractures beneath unconsolidated sediments. The genetically different tectonic structures under investigation are located in northern Spain and in northern Germany. For neither research area information on ^{222}Rn activity regarding the investigated structures existed.

In the southern Cantabrian Mountains, NW Spain, the ^{222}Rn in soil gas signal was measured across the seismic active Ventaniella Fault (VF) and the seismic inactive Sabero-Gordón Fault (SGF). During a first survey in summer 2010, both faults were found to be traceable by elevated ^{222}Rn in soil gas signals. Unexpectedly, the SGF showed higher ^{222}Rn activity compared to the VF. During a second survey in autumn 2010 detailed sampling across SGF was conducted and zones of elevated ^{222}Rn activity were shown to be consistent throughout time.

A quantitative palaeostress analysis based on fault-striae data was carried out in the research area in northern Spain in order to unravel the deformation history of fault development. The most recent maximum horizontal compression direction is oriented N–S to NW–SE and coincides with the actual main stress orientation reported for the Iberian Peninsula, that is about NW–SE. Under such stress orientations, movements of the SGF are very probable and the SGF must be considered as active aseismic fault.

In Schleswig-Holstein, locally elevated ^{222}Rn concentrations in soil gas occur as shown on the German ^{222}Rn-map. The occurrence of the elevated concentrations has been ascribed to the deposited radionuclide rich moraine boulder material, but the contribution of active subsurface structures has not been investigated so far. Therefore, ^{222}Rn in soil gas activity was measured across the margins of two active salt diapirs. Reference samples were taken from a region known for its granitic moraine boulder deposits in order to quantify the influence of the glacial deposits on the measured signals. The ^{222}Rn activities resulting from profile sampling across the Bad Segeberg-Sülberg salt structure and the Siek salt dome margin are evidently higher than the signals induced by the glacial deposits.

Along with ^{222}Rn in soil gas measurements petrophysical soil parameters and meteorological conditions were documented during the samplings. No correlation with ^{222}Rn in soil gas values was found. Slight spatial shifts in the position of the zones of maximum ^{222}Rn activity in soil gas across the investigated subsurface structures as well as the change in magnitude of the ^{222}Rn activities sampled at different dates on the same site indicate that the signals are caused by structural conditions.

Deformation processes increase the surface of components, thus leading to enhanced ^{222}Rn emanation. Active genesis of pathways for gas migration driven by aseismic fault slip is proposed as mechanism provoking the elevated ^{222}Rn in soil gas signals reported from the SGF. The hypothesis of active slip on the SGF is supported by the quantitative palaeostress analysis based on fault-striae data carried out in the research area.

For three representative soil gas profiles from both research areas the trends in mother and daughter nuclide distribution (^{226}Ra and ^{222}Rn, respectively) were compared. The comparison of ^{222}Rn in soil gas concentrations with ^{226}Ra in soil activities is not clear-cut and both, correlated trends and non-correlated trends are observed. These results indicate that the validity of structural ^{222}Rn signal determination by geochemical thresholds based on ^{226}Ra activity has to be reconsidered.

In the present thesis, a theoretical model was developed which summarises the relevant processes contributing to enhanced ^{222}Rn activity in soil gas at the margins of active salt structures. This work provides a first approach regarding the halokinetic contribution to the ^{222}Rn in soil gas occurrence. The data collected during this thesis support the successful application of ^{222}Rn measurements to detect different active geological subsurface structures, even active structures that move slowly by aseismic creep.

Contents

1 Introduction

In nature three isotopes of the element radon (Rn) occur, ^{219}Rn (actinon); ^{220}Rn (thoron) and ^{222}Rn (radon) (Fig. 1.1). Actinon and thoron have an extremely short half life of 3.96 s and 55.6 s, respectively, whereas ^{222}Rn has a half life period of 3.82 days. ^{222}Rn belongs to the ^{238}U decay chain and forms by α-decay from its mother nuclide ^{226}Ra (Fig. 1.1). It is a chemically inert, radioactive, water-soluble, odor- and colorless gas. The primary source of ^{222}Rn in the natural environment provides the radionuclide content in soil and rocks. ^{222}Rn concentration in soil gas increases with depth (Jönsson, 1995; Kristiansson and Malmqvist, 1984) until a constant level at certain depth is reached, which depends on the soil´s properties and moisture content. In shallow depths (< 1 m) atmospheric dilution and exogene factors have an impact on the ^{222}Rn concentration in soil gas. Due to their migration ability ^{222}Rn isotopes reach the upper layers of the soil and contribute as a substantial part to radiation environment of humans (Tanner, 1964).

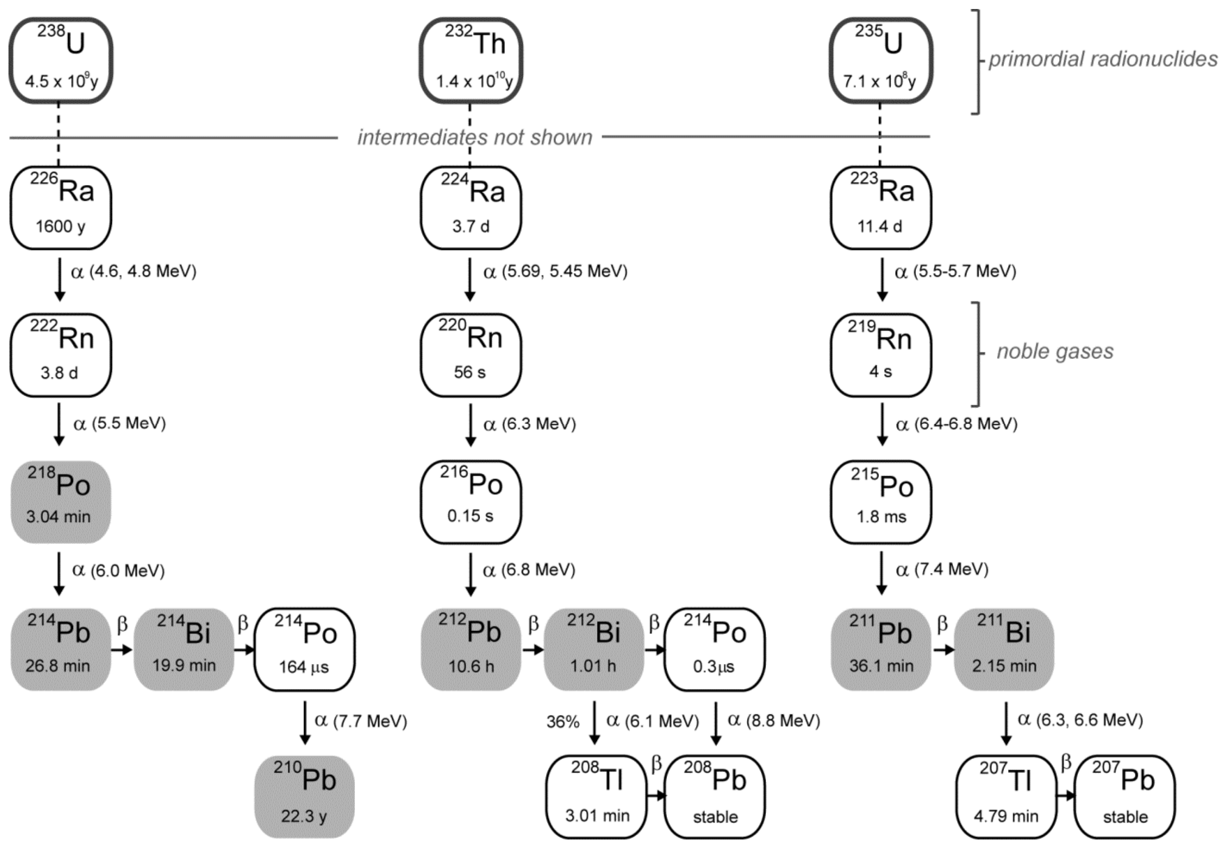

Fig. 1.1: Decay series of ^{238}U, ^{235}U and ^{232}Th; half life and primary decay mode are shown for each isotope; the inhalation of isotopes highlighted in grey is harmful; modified after Nazaroff (1992).

In 1988, ^{222}Rn has been classified as human carcinogen by the International Agency for Research on Cancer (IARC) (George, 2007; ICRP, 2007; WHO, 2009). The recognition of ^{222}Rn as a health hazard has encouraged international research programs to access areas bearing high ^{222}Rn risks. In geosciences, ^{222}Rn is used as a tracer. Understanding the behaviour of ^{222}Rn and detecting its concentrations provide important insights into a range of processes that are of primary interest, from geological and geophysical approaches via the exploration of uranium deposits through to radiation protection.

In this thesis, the traceability of potentially active faults and active salt structures by ^{222}Rn in soil gas activity is investigated. The major part of this introduction gives a review of the occurrence of ^{222}Rn in soil gas, influencing factors and the application of ^{222}Rn in soil gas measurements in earth sciences. Section 1.6 summarises the proceedings from the discovery of ^{222}Rn to its recognition as human carcinogen and the progress of European guidelines for protection against ^{222}Rn.

1.1 ^{222}Rn release in the geological environment

The radionuclide content in the soil provides the primary source for ^{222}Rn in soil gas activity. ^{222}Rn in soil gas is generated by α-recoil of ^{226}Ra. Emanation is the process by which ^{222}Rn leaves the solids and reaches the pore space. The amount of emanation or emanating power is influenced by a range of conditions which are outlined below. Of primary importance is the distribution of the direct parent nuclide ^{226}Ra in the soil, i.e. the location of ^{226}Ra in grains or at the surface of components. The emanation is limited due to the recoil range of ^{222}Rn atoms, which is about 20–70 nm (Monnin and Seidel, 1992). As a result, only ^{226}Ra atoms located within this range from the grain boundary contribute to the fraction of ^{222}Rn which can escape from the solid. Morawska and Phillips (1993) found that for a grain without inner porosity the theoretical emanation coefficient is much lower, assuming a uniform ^{226}Ra distribution compared to the assumption of surface distribution of ^{226}Ra. Despite reaching the pore space, ^{222}Rn atoms can penetrate into the adjacent grains. A synoptic depiction of the possible emanation scenario is given in Fig. 1.2. The results of Greeman and Rose (1996) imply that in soil about half of the emanated ^{222}Rn reaches the pore space via direct recoil, whereas diffusion and track etching account for the second half. According to Nazaroff (1992), the escape of ^{222}Rn by diffusion from intact grains is negligible.

Further, the emanation is strongly dependent on the bulk density of the soil, the total porosity, as well as the water content. The emanating power is dimensionless and varies between 0 (no ^{222}Rn escapes) and 1 (all ^{222}Rn escapes) (Bossew, 2003). Typical values for the emanating power in soils and fine grained materials vary from 0.02 to 0.5 (Greeman and Rose, 1996; Tanner, 1964). The average value for the emanation coefficient is about 0.2 (Nazaroff, 1992) or 0.25 (Gómez-Escobar et al., 1999). The emanation rate is sensitive to physical forces such as pressure and stress (Martinelli, 1993).

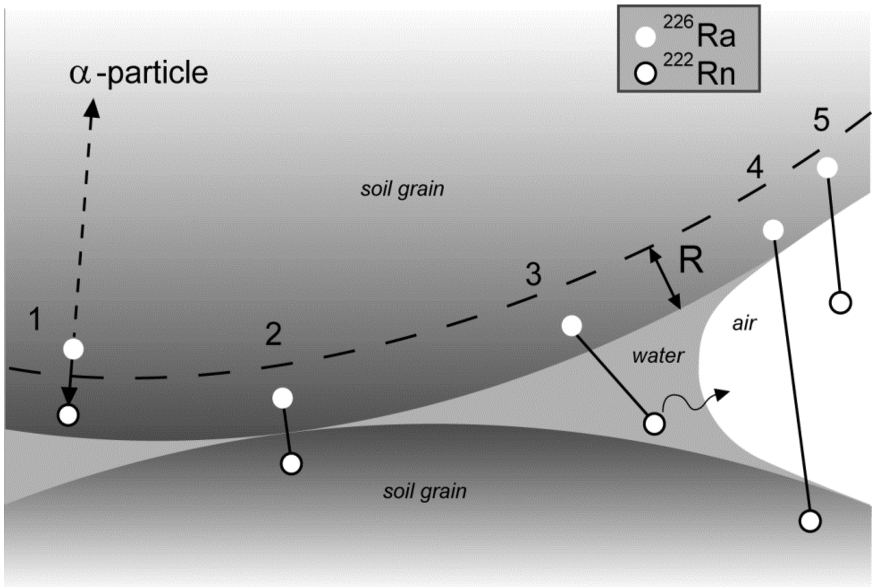

Fig. 1.2: Schematic sketch of the possible emanation scenarios in a solid-water-air system; R = maximum recoil range; case 1) ^{222}Rn remains inside the grain; case 2) ^{222}Rn reaches the adjacent grain; case 3) ^{222}Rn atom reaches the water filled pore space, possibly reaching the air filled pore space by diffusion; case 4) recoil energy is large, ^{222}Rn crosses the air filled pore space and penetrates into the adjacent grain; case 5) ^{222}Rn atom reaches the air filled pore space; modified after Greeman and Rose (1996), Kemski et al. (1996a) and Tanner (1980).

In several cases the calculated emanation coefficients differ from the measured ones (Nazaroff, 1992). Approaches to explain this discrepancy are based on the assumption that ^{226}Ra is distributed at the grain surfaces (Krishnaswami and Seidemann, 1988) or that chemical corrosion and radiation damage due to decay processes lead to damages in the crystalline structures of the grains, thus enhancing the escape ways for ^{222}Rn (Nazaroff, 1992). In addition to the paths presented in Fig. 1.2, fractured grains provide further accesses to the pore space (Kemski et al., 1996a).

It is generally known that ^{222}Rn emanation increases with decreasing grain size (Markkanen and Arvela, 1992; Morawska and Jeffries, 1994). This is explained by the recoil theory and by the fact that the smaller the grain size, the larger the surface area which is available for ^{226}Ra adsorption (Megumi and Mamuro, 1974). A further contribution is the accumulation of radionuclide rich heavy minerals in the small grain size fraction due to weathering processes and sedimentation (Kemski, 1993).

The water content in the soil influences the emanation. In pores filled with water, the recoil range is smaller, thus preventing the penetration of escaping ^{222}Rn into the adjacent grains (Tanner, 1964). Water molecules further occupy adsorption places at mineral surfaces thus reducing the fraction of ^{222}Rn which adsorbs onto grains (Kemski, 1993). According to Markkanen and Arvela (1992) the water content effects ^{222}Rn emanation in dependency of the grain size, i.e. high water content in clay leads to enhanced ^{222}Rn emanation, whereas gravel needs less water content to fill the pore space.

Once having reached the pore space, ^{222}Rn can migrate not only by diffusion processes but also by advective and convective processes, thus moving away from its source (Fig. 1.3). This ability to migrate complicates the direct correlation between ^{222}Rn in soil gas and the radionuclide content in the soil. The inertness of ^{222}Rn inhibits chemical reactions and the short half life constraints the migration distances. These special characteristics make ^{222}Rn so important in earth sciences acting as a natural tracer for different processes.

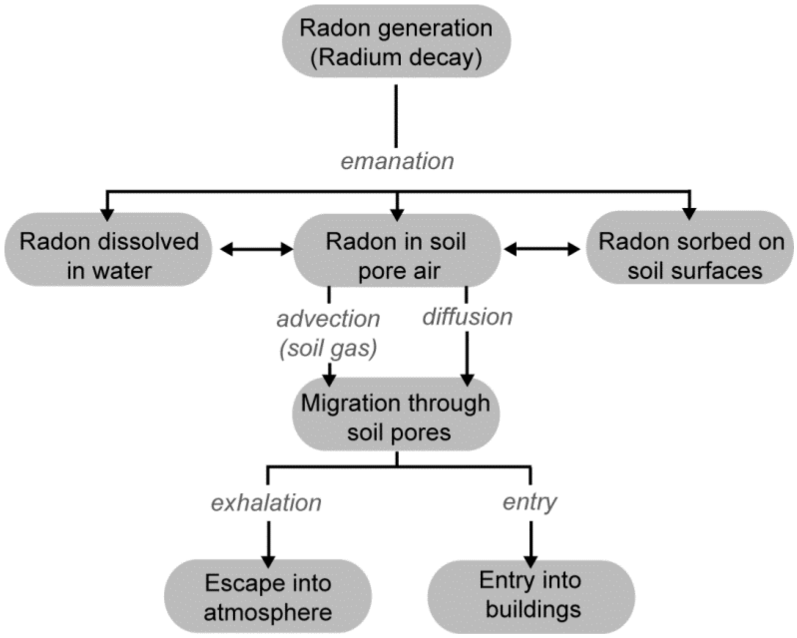

Fig. 1.3: ^{222}Rn release, migration and exhalation or entry, modified after Nazaroff (1992).

Gas movements in the subsurface originate basically in concentration and pressure gradients (Etiope and Martinelli, 2002). The movement of gas molecules to equalize concentration gradients is the process of diffusion which is described by Fick´s law. In a one dimensional form along a *z*-axis it can be expressed as:

$$F = -D_m \frac{dC}{dz} \tag{1}$$

where D_m is the molecular diffusion coefficient (m^2/s), dC is the variation of gas concentration (kg/m^3) along the distance dz (m). The diffusion coefficient is a constant of the particular gas which changes with the medium in which the motion occurs and is dependent on temperature and pressure. With respect to soil and rock pores, the diffusion coefficients in water and air are of importance. Three types of diffusion coefficients exist which describe three different processes: molecular diffusion of gas in a fluid (described by equation 1), interstitial diffusion of gas in a medium, which will be described below (equation 2) and the global diffusion of gas in a medium, which will not be discussed further. The interstitial diffusion is described by the effective diffusion coefficient:

$$D_e = D_m n \tag{2}$$

where n is the effective porosity of the medium (%). The global diffusion includes the porosity as well as the tortuosity of the medium. According to Nazaroff (1992), D_e for ^{222}Rn in soil of low moisture content is 0.03 cm^2/s, whereas in open air the diffusion coefficient is about 4 times larger.

For a long time diffusion was the mechanism thought to be responsible for the motion of ^{222}Rn in the ground (Kristiansson and Malmqvist, 1984). Diffusion as moving mechanism does not allow a migration of ^{222}Rn exceeding 10 m before the concentration of ^{222}Rn is significantly reduced by decay (Etiope and Martinelli, 2002; Kristiansson and Malmqvist, 1984).

The migration due to pressure gradients is termed advection. In the literature the term “convection” is often used as synonym for advection (Keller et al., 1992; Kemski, 1993) but it refers to a pressure gradient which is induced by geothermal gradients (Etiope and Martinelli, 2002). The general term “transport” (Tanner, 1964) finds application to describe migration by advection. Migration due to pressure gradients necessitates the presence of a certain amount of the particular gas species. The amount of ^{222}Rn in the subsurface is too small to flow autonomously by advection. Advective movement of ^{222}Rn is therefore dependent on a carrier gas such as CO_2 that is present in the required amounts (Etiope and Martinelli, 2002). The migration width related to advective ^{222}Rn transport is reported to be in the range of tens of meters.

Diffusive and advective migration of ^{222}Rn may occur simultaneously whereas diffusion may take place alone (Monnin and Seidel, 1992). After the migration through soil ^{222}Rn escapes into the atmosphere (exhalation) or may enter into buildings (Fig. 1.3).

1.2 Exogene influences on ^{222}Rn concentrations in soil gas

The ^{222}Rn concentration in soil gas near the surface i.e. at the soil-atmosphere interface is influenced by meteorological conditions as reported by King and Minissale (1994) and Washington and Rose (1992). Moisture content of soil is strongly dependent on both precipitation rates and events, and petrophysical soil parameters. The ^{222}Rn emanation in soil was found to increase up to a certain point with moisture content (Sundal et al., 2004). A dependency between moisture content of the soil and ^{222}Rn activity in soil gas has been reported in e.g. Menetrez and Mosley (1996) and Papastefanou (2010).

The atmospheric pressure is found to correlate negatively with the ^{222}Rn concentration in soil gas (e.g. Kraner, 1964; Rigby and La Pointe, 1993). Schery et al. (1982) investigated the transport of ^{222}Rn from fractured rocks and their results display the negative correlation of the ^{222}Rn signal with barometric pressure changes.

Temperature has further influence on ^{222}Rn in soil gas concentrations. At increasing temperature conditions, ^{222}Rn in the gas phase of the soil increases. Considering an annual behaviour, ^{222}Rn concentration in soil gas should be higher during summer. Temperature differences between the atmosphere and the soil gas have an influence on gas migration.

The factors presented above are changing seasonally, accordingly a seasonal variation of ^{222}Rn in soil gas concentration occurs (e.g. King and Minissale, 1994; Klusman and Webster, 1981; Washington and Rose, 1992). Washington and Rose (1992) quantified the seasonal variability of ^{222}Rn in soil gas in soils of Pennsylvania, and reported lower ^{222}Rn values in winter, having only 10–50% of the ^{222}Rn activity measured during summer. Nevertheless, the results of the annual ^{222}Rn surveys at different sites do not reveal unequivocal trends, as ^{222}Rn concentration is dependent on the geographic location of the sampling sites (King and Minissale, 1994). For example snow cover, soil frost and high moisture content constitute a sealing between soil gas and atmospheric air thus increasing ^{222}Rn concentration in soil gas due to inhibited dilution (Kovach, 1945).

1.3 Application of ^{222}Rn measurements in earth sciences

Variations of ^{222}Rn concentrations in soil gas and groundwater along with seismic and volcanic activity have been reported in numerous publications (e.g. Ghosh et al., 2009; Heinicke and Koch, 2000; Papastefanou, 2010; Segovia, 1991). Of special interest is the applicability of ^{222}Rn as premonitory measure of geophysical events. The correlation between changes in ^{222}Rn activity and seismicity started in Japan and the first results were published by Okabe (1956). Subsequently, real time monitoring of seismic and volcanic areas was carried out all over the world. A comprehensive review of the literature published in the research area of ^{222}Rn as seismic precursor is given in Ghosh et al. (2009). Analogously there are numerous observations of enhanced ^{222}Rn signals that are correlatable with volcanic activity (e.g. Ahmed Khan, 1991; Baubron, 1991; Segovia, 1991; Segovia et al., 1997). The elevated ^{222}Rn concentrations occurring along with geophysical events are thought to have either a deep-lying origin or a local, surface near one. In the case of volcanic eruptions degassing of magma provides the deep-lying source. In the case of seismic activity the local source of ^{222}Rn is explained by the displacement by pore fluids that are triggered by geophysical activity (Monnin and Seidel, 1991). The distant source or "deep origin" is stated to be the crushing of U-rich minerals of the bedrock (Monnin and Seidel, 1991). Even though in seismic and volcanic relevancies there are evidences for correlation with near surface ^{222}Rn in soil gas or water, other environmental influences as climatic conditions complicate the application of ^{222}Rn measurements in predicting geophysical hazard. A detailed review about the use of geochemical instabilities in the field of earthquake prediction is given in Bernard (2001).

A further field of application of ^{222}Rn measurements is the detection, identification and localization of geological faults by ^{222}Rn measurements, which emerged due to the investigation of seismic events with ^{222}Rn concentration changes. A vast number of publications is available, discussing the detection of active faults by applying ^{222}Rn in soil gas measurements. It is very likely that ^{222}Rn is the most frequently utilized gas for mapping purposes (Toutain and Baubron, 1999). The increase of ^{222}Rn

activity in soil gas related to active fault zones at different sites has been reported in e.g. Al-Hilal and Al-Ali (2010); Amponsah et al. (2008); Baubron et al. (2002); Font et al. (2008); González-Díez et al. (2009); Ioannides et al. (2003); Kemski (1993); Kemski et al., (1992); King et al., (1996); Lombardi and Voltattorni, (2010); Papastefanou (2010); Seminsky and Bobrov (2009); Swakón et al., (2004); Tanner (1980), and is a subject of interest for researchers in risk analysis and mapping of active fault areas (Burton et al., 2004; González-Díez et al., 2009; Ielsch et al., 2010). The source of ^{222}Rn detected above active faults and the use of ^{222}Rn as a tool to detect active faults have been discussed by various researchers, analogous to the occurrence of ^{222}Rn with seismic activity. The correspondence between active faults and leaking of soil gas into the surface originated the hypothesis that faults and fractures provide pathways for fluid flow. According to Ciotoli et al. (1999) even in clayey basins where tectonic faults are not apparent at the surface, the detection of gas leaks provides an important tool to identify neotectonic activity. Although reported from numerous sites around the world, enhanced ^{222}Rn release related to active tectonic faults still entails controversial and critical concepts- particularly regarding the source of ^{222}Rn. The involvement of changes in the stress/strain field causing geochemical anomalies was first proposed by King (1978), and nowadays the scientific community widely agrees with it as source mechanism (Fleischer, 1981; King, 1986; Toutain and Baubron, 1999).

The question for ^{222}Rn sources and effectivity of ^{222}Rn as indicator for geodynamic purposes stimulated an investigation of ^{222}Rn release under applied stresses, which revealed promising results. Holub and Brady (1981) investigated the emanation of an U-bearing granitic rock under uniaxial stress and recorded the emanation and microcrack activity. They reported an increase in ^{222}Rn emanation with initiating crack growth. Their results correlate with the observations from ^{222}Rn activity related to seismic activity, i.e. decrease in ^{222}Rn emanation when stresses acting are too low to produce microcracking of rock and increase in ^{222}Rn emanation when rock fails. Small changes in applied stress produce significant changes in ^{222}Rn emanation (Holub and Brady, 1981). Mollo et al. (2011) and Tuccimei et al. (2010) investigated ^{222}Rn emissions from tuff and phonolite samples under increasing deformation. The porous tuff showed a decrease in ^{222}Rn emission due to the closure of macropores at the end of the elastic phase. The porosity decreased further after the failure due to the closure of macro- and micropores but the new surfaces created due to failure led to an increase in ^{222}Rn emission (Tuccimei et al., 2010). However, the ^{222}Rn emission of the damaged phonolite showed no changes until the development of fractures, which led to an increase of ^{222}Rn emission (Mollo et al., 2011). These results support the hypothesis that the driving forces of geochemical instabilities are changes in the stress and strain field (Toutain and Baubron, 1999).

The effects of stress variations on ^{222}Rn emanation are crucial for the interpretation of ^{222}Rn emissions occurring in active tectonic areas. Models explaining the behaviour of rocks before an earthquake occurs agree that at a certain period, a region of cracks develops (Ghosh et al., 2009; Martinelli, 1993). The “Crack avalanche model” expresses that a cracked focal rock zone will generate during increasing tectonic stresses and the shape and volume of this zone will change slowly with time (Ghosh et al., 2009; Martinelli, 1993). Other models as the “Dilatancy diffusion model” include rock-fluid interaction to explain not only the enhanced release but also the behaviour of present fluids in the subsurface. In a porous, cracked and saturated rock, increasing tectonic stresses lead to the extension of cracks near the pores. Water will diffuse from the surrounding rocks into the newly formed cracks drying the rock adjacent to the pore thereby inducing a decrease of pore pressure in the preparation zone. At the end of the diffusion period, the return of pore pressure and crack increase causes the main rupture (Ghosh et al., 2009; Martinelli, 1993; Scholz et al., 1973). Generally, the mechanisms proposed involve tectonically induced movements of crustal fluids or enhanced rock-fluid interaction at newly created rock surfaces (King, 1993). The occurrence of changes in ^{222}Rn concentrations at large distances (> 100 m) from the supposed source region necessitated consideration of fluid driven phenomena (Mogro-Campero and Fleischer, 1977; Toutain and Baubron, 1999).

The either distant or local source of ^{222}Rn signals measured in the surface soil was discussed in several publications and is of high relevance especially in the field of active fault localization, ^{222}Rn signals related to earthquakes and the localization of uranium deposits. Due to the relatively short half life of ^{222}Rn and the slowness of the diffusive migration the source of ^{222}Rn concentrations in soil gas was expected to originate at short distances from the sampling point (e.g. Monnin and Seidel, 1991). As mentioned above numerous publications reported long distance transport of ^{222}Rn in several environments and investigation fields (e.g. Fleischer, 1981; Fleischer and Mogro-Campero, 1978, 1979; Kristiansson and Malmqvist, 1982, 1984; Mogro-Campero et al., 1980). The possibly distant source of ^{222}Rn was discussed when changes in ^{222}Rn concentrations correlated with seismic events that occurred at distances of several kilometers from the measurement points (Fleischer, 1981; Mogro-Campero et al., 1980). The processes that lead to enhanced ^{222}Rn concentrations in soil gas or water due to earthquakes correspond to the processes that are important for active fault detection. Within the discussion on the either distant or local source of ^{222}Rn it is important to bear in mind that the actual subjects of discussion are rather the different mechanism leading to anomalous concentrations in soil gas (Toutain and Baubron, 1999). Many authors advocate that the ^{222}Rn source resides in a rather small region (e.g. Monnin and Seidel, 1991). Nonetheless, rate of transport of ^{222}Rn plays an important role (Monnin and Seidel, 1991). Increasing stress increases the flow rate of pore fluids, thereby enhancing ^{222}Rn transport equally with enhanced release through newly created surfaces due to cracking. Ghosh et al. (2009) explain that ^{222}Rn signals coinciding with earthquakes are not supposed to originate in the focal zones. Proposed processes are the local release of ^{222}Rn or local flow which transports ^{222}Rn to equalize concentration discrepancies generally within a few meters (Ghosh et al., 2009). King (1993) proposed that gas anomalies are the result of broad scale episodic strain changes in the crust which may be induced by magma intrusion or episodic fault-creep events below the seismogenic area. According to the author´s model, changes may be amplified along pre-existing fault zones. Despite different mechanisms that cause elevated ^{222}Rn concentrations or, more generally, account for geochemical anomalies – the reported occurrence of such phenomena have in common a unique driving force: changes in the stress field (Toutain and Baubron, 1999).

Geological faults have an impact on geochemical anomalies for different reasons. Faults on their own provide least strength zones constituted by fractured material, gouge and fluids. According to Bernard (1992), instabilities in crustal fluids are associated with active tectonic regions. Faulting triggers fluid flow. In turn, fluids have an impact on faulting as they influence the strength of a fault. Sibson (1992, 1994) describes the dynamic interplay of faulting and fluid flow including rupturing, increasing permeability and destruction of permeability and fluid flow in terms of the fault-valve behaviour (Fig. 1.4). Especially active faults are suitable for gas leakage, as gas migration is facilitated by increased soil permeability (Bernard, 1992; Toutain and Baubron, 1999). The presence of fault gouge is thought to alter soil gas composition as gouge usually is enriched by trace elements and radionuclides (Lyle, 2007; Sugisaki et al., 1980). King et al. (1996) measured ^{222}Rn in soil gas across a creeping fault and suggested that the presence of fault gouge leads to a low permeability zone, visualised in the ^{222}Rn profile as twin peak feature. Adjacent to the impermeable zone of fault gouge, elevated ^{222}Rn concentrations occur due to the presence of fractured rock. Muir Wood (1994) and Seminsky and Bobrov (2009) proposed that soil gas anomalies are dependent on the fault type (i.e. reverse or normal faults). The above cited references imply that active faults are connected with geochemical anomalies. These anomalies may derive directly from the depth or may be generated by the rocks constituting the hanging wall and footwall of the fault (Toutain and Baubron, 1999). Changes in permeability and porosity characteristics of the faulted zone due to self sealing of fractures or weathering processes influence the geochemical signal. Yet small strains induce geochemical anomalies. Pre-existing faults may amplify the anomalies if former stresses were near the critical levels and pore fluids are abundant (King, 1986; King 1993). This model allows far field effects in terms of distant stress centers causing geochemical anomalies. Bernard (2001) introduces the term “transients” for precursory phenomena that are related to unstable processes, such as fault creep and episodic fluid flow. The author proposes that instabilities stated to occur premonitory to earthquakes are coupled among each other (earthquakes-creep transients-fluid transients).

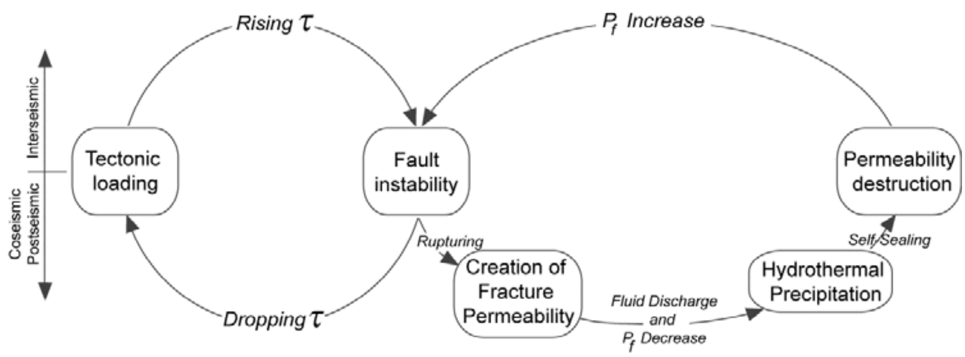

Fig. 1.4: Fault valve activity, P_f = fluid pressure within a rock mass, τ = shear stress, adopted from Sibson (1992).

Regarding the long-distance transport of ^{222}Rn, several mechanisms were proposed. Kristiansson and Malmqvist (1982) brought forth the theory of geogas upflow through waterfilled fractures and ^{222}Rn transport by microbubbles. The experiments of Varhegyi et al. (1992) of microbubble transport of ^{222}Rn in water or water-saturated media proved the validity of the theory even for migration distances exceeding 100 m. Heinicke and Koch (2000) investigated the role of bubble advection reacting on seismic activity and revealed hydrogeochemical anomalies related to earthquakes induced due to slug flow of CO_2 in water filled faults, with velocities up to 7–8 cm/s (Etiope and Martinelli, 2002). This high velocity allows deep source ^{222}Rn to reach the surface. Etiope and Lombardi (1995) describe high ^{222}Rn in soil gas values in faulted low-Ra clay and for an explanation they took into consideration the carrier effect of ascending microbubbles. On their rise microbubbles collect radionuclides from the geological formations, hence leading to a release at the groundwater surface and consequently to an accumulation of ^{222}Rn and its precursors. Etiope and Lombardi (1996) observed the transport of radioactive particles through sand after bubbling the test column with air. According to these authors, elevated ^{222}Rn in soil gas occurrence caused by ascending microbubbles does not require a local source accumulation. The role of ^{226}Ra transport by microbubbles is not completely investigated yet, but some authors reported gas flow as main transport mechanism for ^{226}Ra (Spivak et al., 2008).

1.4 Active faults

In the field of fault localization the term "active fault" needs further explanation. Active faults are faults characterised by active slip, usually determined by seismic signals. The term "possibly active faults" appears repeatedly in the geoscientific literature. It refers to faults that are located in parts of the earth´s crust that are considered to be stable in terms of seismicity (González-Díez et al., 2009). Nevertheless, earthquakes related to faults that were previously considered to be inactive have been reported (e.g. Crone et al., 1997), which implies the need for the identification of such faults. González-Díez et al. (2009) proposed the term "latent state" for such faults. Sudden motion along a fault is expressed by earthquakes. On pre-existing faults, "stick-slip" frictional instability is responsible for slip of these faults, thus initiating earthquakes (Brace and Byerlee, 1966; Fagereng and Toy, 2011). Elastic strain accumulates in the rocks surrounding the fault and failure occurs once shear stress on the fault exceeds its frictional strength (Fagereng and Toy, 2011; Reid, 1911). Stress may further be released by the formation of new faults. The strength of a single fault can vary as the surfaces may heal after rupture. The occurrence of aseismic slip (= fault creep) instead of seismic slip is attributed to low frictional strength of a fault, low values of normal stress acting on a fault and the presence of elevated pore fluid pressures (http://funnel.sfsu.edu/creep/; Van der Pluijm, 2011). According to Van der Pluijm (2011), weak fault behaviour is caused by high fluid pressures or by the presence of lubricant. Especially the presence of clay minerals weakens the fault and promotes aseismic creep (Van der Pluijm, 2011). Slow movement (= aseismic slip) along faults does not emit seismic waves and signals are too small to be detected with borehole strainmeters (Roeloffs, 1999). However, changes in ^{222}Rn emissions similar to changes in the electrical or magnetic fields are known to have a potential as natural amplifiers of deformation processes (Roeloffs, 1999; Toutain and Baubron, 1999).

In order to use ^{222}Rn as a tool for identifying active faults, it has to be ensured that inactive faults are not traceable by elevated ^{222}Rn signals in the soil cover. Lombardi and Voltattorni (2010) applied soil gas surveys across faults in a seismically quiescent region in the southern part of Sardinia Island and found no relevant ^{222}Rn signals, proposing that gas channeling from depth is prevented by self-sealed inactive faults. The fault under investigation was characterised as blind fault, which terminates in unconsolidated sediments near the surface. Tanner (1964) reported that in unconsolidated ground, fissure systems seal themselves in about a week´s time, thus evidence is given that elevated ^{222}Rn signals related to faults require the faults recurrent activity whether it is seismic or aseismic. Bense et al. (2003) investigated the deformation processes in fault zones occurring in unconsolidated sediments. The deformation mechanism of unconsolidated sediments in shallow depths is particulate flow, which disaggregates the grain fabrics. The damaged zone is likely to be a zone of enhanced fluid flow (Bense et al., 2003).

In a seismically rather stable area, faulting may further be induced by salt tectonics. Apart from constituting important characteristics for oil and gas deposits, an intense investigation was carried out in the recent years to assess the suitability of salt structures in the field of nuclear waste deposition. The generation of a salt diapir requires the existence of a fault or weakness zone. Salt tectonics is mostly based on an interplay between tectonic stresses, buoyancy of the salt and the effects of changes of the sedimentary load. Salt structures in "active state" are driven by buoyancy (Vendeville and Jackson, 1992a, b). The strain rates reported from salt diapirism driven by buoyancy are of 10^{-12} to 10^{-15} s^{-1} (Keken et al., 1993), Jackson and Talbot (1986) reported strain rates for the deformation of rock salt varying between 10^{-8} and $10^{-16}s^{-1}$. Differential loading, extrusion of salt and active tectonics may lead to even higher strain rates with respect to halokinesis in the shallow crust (Keken et al., 1993). According to Hauksson (1981) ^{222}Rn anomalies in well water occur at strain rates of 10^{-12} to 10^{-17} s^{-1}. ^{222}Rn emissions related to very small strain rates have been reported associated with earth tides. Thus, assuming the presence of pathways for gas migration along with fluids constituting the carriers, ^{222}Rn concentrations in soil gas should change due to salt movement. Depending on stress state and strain rates, the sediments covering salt structures can deform either in a brittle or viscous way (Poliakov et al., 1996).

1.5 Identification of components constituting ^{222}Rn signal in soil gas – possibilities

Different approaches for the differentiation of the advective and diffusive ^{222}Rn in soil gas signal have been established. According to Ciotoli et al. (1999) and Kemski (1993) the ^{222}Rn in soil gas concentrations exceeding a threshold value are stemming from deeper strata and reach the surface soil gas due to the presence of structural pathways. In general there are two approaches to ensure the structural contribution to the measured signal.

First, the definition of a geochemical threshold value, which may be obtained by the consideration of regional ^{222}Rn activities of the particular geological formations, often represented as ^{222}Rn maps; by average values calculated of concentrations beneath maxima values (King et al., 1996) and by the application of statistical methods (Baubron et al., 2002). These thresholds are used, if no information about radionuclide content of the investigated soils is available.

The second approach is the determination of the geochemically induced ^{222}Rn concentration based on U or Ra determination in the particular soils (e.g. Ciotoli et al., 1999; Kemski, 1993). For the calculation of the diffusive ^{222}Rn component the petrophysical soil parameters must be included (soil bulk density, effective porosity and the emanation coefficient of the soil species) and the Ra concentration in soil must be determined. Knowing the U concentration, the Ra concentration can be assessed by the equivalent concentration (2 ppm U = 25 Bq/kg Ra (Ciotoli et al., 1999)). Another approach constitutes the measurement of carrier gases or other trace element gases along with ^{222}Rn in soil gas measurements, which confirms the presence of a gas leak.

1.6 Rn discovery and recognition of imposed health risk

Rn was discovered 1900 by the German chemist Friedrich E. Dorn and called “Radium emanation”. As early as the 16th century, G. Agricola, a German physician and geologist noticed the frequency of lung disease occurring among miners in Schneeberg, in the Erzgebirge in Sachsen, Germany (Cothern and Smith, 1987). In the 17th century similar effects came up in the mines of Joachimsthal in Bohemia, Czech Republic. In both mines copper, iron, silver ores and, since 1880, pitchblende were exploited. In 1879 two German physicians, Hartung and Hesse could identify that the so called “Bergkrankheit” was the cause of most of the deaths among Schneeberg miners which later could be identified as lung cancer (Cothern and Smith, 1987). In 1921, Margaret Uhlig was the first who suggested that “Radium emanation” could be the cause for lung cancer incidence (Cothern and Smith, 1987). It was not until 1988, however, that Rn was identified as human carcinogen by IARC (International Agency for Research on Cancer) (George, 2007; ICRP, 2007; WHO, 2009). Nowadays it is well known that Rn is the second cause of lung cancer after smoking. According to the WHO (2009) “Handbook of indoor Radon” 3–14 % of lung cancers may be attributed to Rn inhalation. The short lived progenies of Rn, radioactive isotopes of polonium, bismuth and lead are attached to dust particles and aerosols. Once they reach the respiratory tract the decay and emission of α-radiation damages the cells (http://www.bfs.de/de/ion/wirkungen/radon_ges.html). Further, Rn contributes about 70% of natural radiation exposure and about 55% of the annual radiation dose to the population (George, 2007). The “Handbook of indoor Radon” provides an overview of the major aspects concerning Rn and health. The International Commission on Radiological Protection (ICRP) published recommendations for protection against Rn in 1993, setting the annual effective dose level at around 10 mSv for Rn (ICRP, 1993).

1.6.1 European guidelines for protection against ^{222}Rn

Due to the Euratom Treaty the European Atomic Energy Community is intended to establish uniform safety standards with the aim to protect the health of workers and general public. Based on the “2007 Recommendations of the International Commission on Radiological Protection” (ICRP, 2007) the European Commission (EC) (European Atomic Energy Community (EURATOM)) proposed a new council directive for European Union radiation protection in 2011 (Council directive 2011/0254; http://ec.europa.eu/energy/nuclear/radiation_protection/doc/com_2011_0593.pdf). In the citizens’ summary of this proposal for a council directive, it is stressed that highest doses to the general public are due to the inhalation of Rn in dwellings. Binding requirements for the Member States include the protection against indoor Rn (Council directive 2011/0254; http://ec.europa.eu/energy/nuclear/radiation_protection/doc/com_2011_0593.pdf). The directive is expected to come into effect in 2012, and the Member States are bound to implement the new requirements and to renew current national law until 2014. The Commission of the European Communities 1990 set reference levels and effective dose equivalents to control the exposure to indoor Rn (Ripa di Meana, 1990). For existing buildings, an annual average Rn gas concentration of 400 Bq/m^3 should not be exceeded, which corresponds to an effective dose equivalent of 20 mSv per year (Ripa di Meana, 1990). For future constructions a design level of an annual average Rn gas concentration of 200 Bq/m^3 is aimed for. According to the reference levels published by the ICRP (2007), in the actual directive the EC recommends 200 Bq/m^3 for dwellings and new buildings with public access. For existing buildings, the reference value of annual average Rn gas concentration is 300 Bq/m^3 (Council directive 2011/0254, http://ec.europa.eu/energy/nuclear/radiation_protection/doc/com_2011_0593.pdf). The reference level for working places is 1000 Bq/m^3. European pooled residential case-control studies showed, that the risk of lung cancer increased by 16% per 100 Bq/m^3 increase in measured indoor Rn (Darby et al., 2005).

2 Objectives of this thesis

In the present thesis, measurements of ^{222}Rn activity in soil gas were conducted across different geological structures located in northern Spain and northern Germany. The research area in Spain is treated in Chapter 3, Chapter 4 and Chapter 7, while Chapters 5 and 7 deal with the research area in northern Germany.

The research area in Spain provides a broad range of geological structures in a region with outcrops of Palaeozoic to Quaternary sediments. Several moderate seismic events have been reported associated with main faults (e.g. López-Fernandez et al. 2004, 2008); on the other hand, numerous faults exist that do not show recent seismic activity. The Sabero-Gordón Fault (SGF) extends about 50 km in an E–W direction, parallel to the Cantabrian Mountain margin (Fig. 2.1). The fault´s character and structural influence are still a matter of debate.

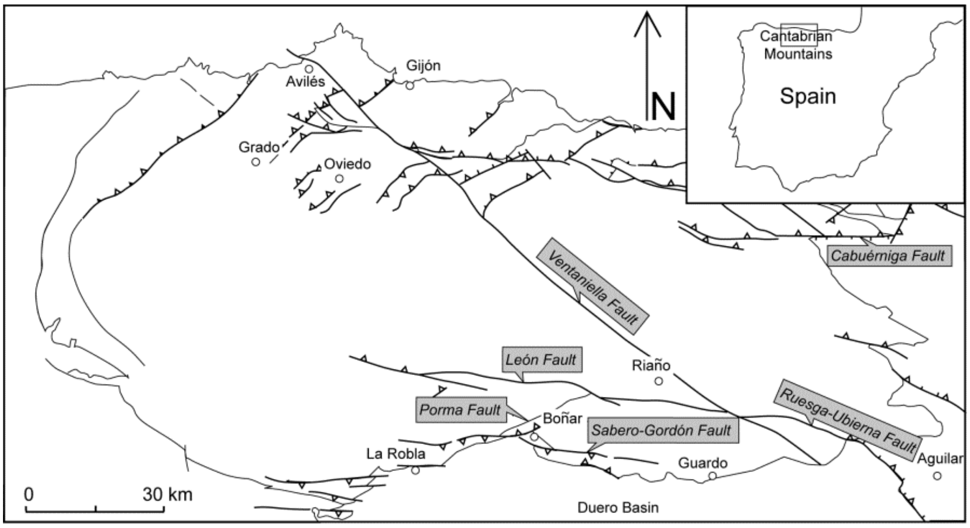

Fig. 2.1: Simplified map of the Cantabrian Zone showing the location of the main faults (modified after Alonso et al., 1996).

Some authors characterise the SGF, including other major structural lines such as the Ventaniella and León Fault (Fig. 2.1), as fractures generated in late Hercynian times with multiple reactivations (Heward and Reading, 1980). The timing of reactivation or reactivations remains unclear, but the geological map of Boñar shows a displacement of Tertiary formations caused by movement on the SGF (Alonso et al., 1990). However, no seismic activity has recently been reported for the SGF. The Ventaniella Fault (VF) extends to about 140 km in a NW–SE direction, crossing the entire Cantabrian Mountain range (Fig. 2.1). Reference to the official geological maps of the region indicates that the VF cuts all previous structures including the Tertiary sedimentary succession (Arthaud and Matte, 1975; Julivert, 1971). Along the fault, seismic activity is continually reported (Alonso et al., 2007; López-Fernández et al., 2004, 2008) particularly northeast of Avilés and near Riaño. In 1989, a 3.7 magnitude earthquake was recorded near El Puerto de Ventaniella (López-Fernández et al., 2004). During the GASPI project 1999–2002 it was found that the seismic events related to the VF near Riaño were of the average magnitude 2 (López-Fernández et al., 2004). The current stress state of the Iberian Peninsula is generally characterised by NW–SE horizontal compression (Jabaloy et al., 2002; Müller et al., 1992; Zoback, 1992) which would favour dextral slip of the fault.

The samplings conducted in northern Spain took place in summer and autumn 2010. Traces perpendicular to the faults were sampled. ^{222}Rn activities in soil gas across the VF and SGF were compared. Based on the unexpected high ^{222}Rn activity measured across the SGF, a detailed soil gas survey was undertaken during the autumn measurement program accompanied by structural field work across segments of the SGF. The aim of this second survey was to reveal if ^{222}Rn activity in soil gas shows consistent trends in time and space and to gather the potential seasonal effect (Chapter 3).

Information about the recent crustal stress orientations in the Cantabrian Mountains is scarce. With respect to Mesozoic to recent deformations little has been published about palaeostress analysis based on fault-striae data in the Cantabrian Zone. Possibly, this is due to the predominant outcrop of Palaeozoic rocks and the complex geological history of the Cantabrian Mountains. The regional main faults cutting the area of investigation display the intricate geological evolution. The main faults were generated during the Variscan Orogeny as well as Mesozoic extensional tectonics and were reactivated during Cenozoic times. Evidence of active deformation of the Variscan basement is given by the recorded seismic events. In order to obtain information about the recent crustal stress orientations in the areas of investigation (SGF, VF), a quantitative palaeostress analysis was carried out (Chapter 4).

The investigation of the ^{222}Rn activity in soil gas in Germany progressed with the development of a national ^{222}Rn map which was published 1998 by the University of Bonn (Kemski et al., 1999). The occurrence of elevated ^{222}Rn in soil gas concentrations in Schleswig-Holstein has been ascribed to the radionuclide rich moraine boulder material deposits, but the contribution of subsurface structures has not been investigated so far. Therefore, ^{222}Rn in soil gas activity was measured across the margins of two active salt diapirs (Schmitz, 1984).

Soil gas- and soil sampling was carried out in springtime and summer 2011. The areas under investigation across the salt structures Siek-Witzhave and Segeberg-Sülberg (Fig. 2.2) were chosen after the examination of the data published in “Geotektonischer Atlas von Nordwestdeutschland und dem deutschen Nordsee-Sektor” (Baldschuhn et al., 2001) and available seismic sections (Wiederhold et al., 2003). The sites had to comply with the following requirements: salt structure beneath the surface or salt tectonic related faults, reaching the surface. Reference samples were taken from a region known for its granitic moraine boulder deposits in order to obtain

^{222}Rn reference values for moraine boulder material (Chapter 5).

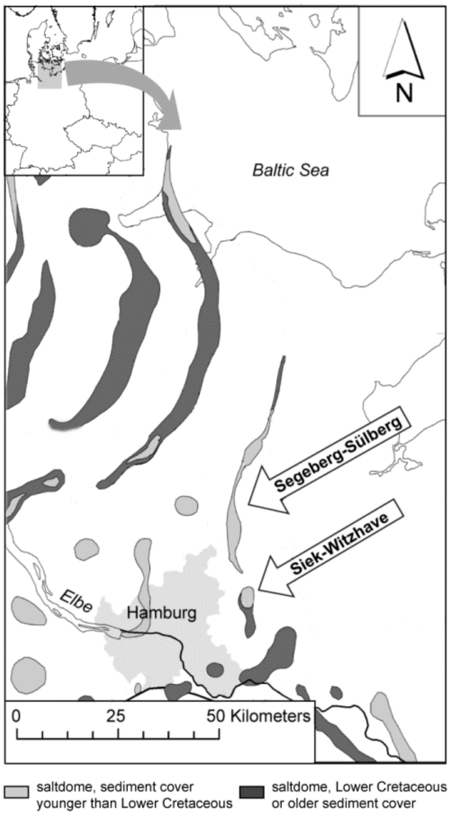

Fig. 2.2: Geographical overview of northern Germany showing the location of the salt structures Siek-Witzhave and Segeberg-Sülberg (modified after Baldschuhn et al., 2001).

The ^{222}Rn signal in surface soil gas may be influenced by meteorological parameters, thus, throughout the samplings conducted, air moisture, temperature and atmospheric pressure were recorded. Additionally, soil samples were collected to determine petrophysical parameters as well as ^{226}Ra activity and to assess their influence on the ^{222}Rn in soil gas concentration. A summary of Ra behaviour in the environment is given in Chapter 6. Measurement of ^{226}Ra was conducted in order to calculate the diffusive component of ^{222}Rn in soil gas activity (Chapter 7). The soil gas samples of each profile were collected at the same date in order to ensure the comparability of the results. To minimize the atmospheric influence the sampling depth for all profile measurements was taken to be at 100 cm. Vertical sampling was conducted with each profile to obtain information about the vertical distribution of ^{222}Rn in soil gas.

The results of this thesis are summarised in four individual chapters (Chapter 3, 4, 5 and 7) that are published in peer-reviewed scientific journals, under review or prepared to be submitted for publication:

Chapter 3:

Künze, N., Koroleva, M., Reuther, C.-D. (2012). ^{222}Rn activity in soil gas across selected fault segments in the Cantabrian Mountains, NW Spain. Radiation Measurements 47, 389-399.

Chapter 4:

Künze, N. Palaeostress patterns in the southern Cantabrian Mountains, NW Spain. Manuscript in preparation.

Chapter 5:

Künze, N., Koroleva, M., Reuther, C.-D. Soil gas ^{222}Rn concentration in northern Germany and its relationship with geological subsurface structures. Under review in Journal of Environmental Radioactivity (submission date: 06.02.2012).

Chapter 7:

Künze, N., Koroleva, M., Reuther, C.-D. ^{226}Ra and ^{222}Rn in soil concentrations: trends across different geological structures in northern Spain and northern Germany. Manuscript in preparation.

3 ^{222}Rn activity in soil gas across selected fault segments in the Cantabrian Mountains, NW Spain

Published 2012 in Radiation Measurements 47

Abstract

^{222}Rn activity in soil gas was measured across fault segments of the seismic active Ventaniella Fault and the seismic inactive Sabero-Gordón Fault in the Cantabrian Mountains, NW Spain, in order to investigate the variability of the ^{222}Rn concentration. The sampling took place in summer and autumn 2010. During the autumn measurement program, an additional ^{222}Rn soil gas mapping was carried out in the Sabero-Gordón research area. Zones of elevated ^{222}Rn activity in the soil gas were identified by background ^{222}Rn values of the geological formations used for mapping and local background values from ^{222}Rn values outside the elevated ^{222}Rn activity zones. Unexpectedly, the Sabero-Gordón Fault showed higher ^{222}Rn activity, up to 441 kBq/m^3, compared to the ^{222}Rn activity of the Ventaniella Fault which had a maximum of 106 kBq/m^3. Comparison of the results shows that the values measured in summer are about 5 times higher than the autumn values. This difference is not reflected in petrophysical soil parameters or meteorological conditions documented during the field measurements. Based on the results of our work we conclude that the magnitude of ^{222}Rn concentration in soil gas is not an indicator of local seismic activity of the investigated faults. For the studied segment of the aseismic Sabero-Gordón Fault we suggest active genesis of pathways for gas migration driven by aseismic fault slip causing the elevated ^{222}Rn activity in soil gas.

3.1 Introduction

^{222}Rn is a daughter product of ^{226}Ra and belongs to the decay series of ^{238}U (Tanner, 1964). Due to the ubiquity of its parent nuclides, the release of ^{222}Rn, a radioactive inert gas with a half life of 3.82 days, takes place in every geological environment. The short half life enables ^{222}Rn as a convenient tracer in geosciences and its distribution in soil gas is used in several applications. In this paper we report ^{222}Rn soil gas measurements across two faults in the Cantabrian Mountains, NW Spain. The increase of ^{222}Rn activity in the soil gas related to active fault zones at different sites has been reported in Al-Hilal and Al-Ali (2010); Amponsah et al. (2008); Baubron et al. (2002); Font et al. (2008); González-Díez et al. (2009); Ioannides et al. (2003); Kemski (1993); Kemski et al. (1992); King et al. (1996); Lombardi and Voltattorni (2010); Papastefanou (2010); Seminsky and Bobrov (2009); Swakón et al. (2004); Tanner (1980) and is a subject of interest for researchers in risk analysis and mapping of active fault areas (Burton et al., 2004; González-Díez et al., 2009). ^{222}Rn measurements in soil gas are further applied to the detection and prediction of seismic (King, 1986; Mogro-Campero et al., 1980; Papastefanou, 2010; Toutain and Baubron, 1999) and volcanic activity (Baubron, 1991; Crenshaw et al., 1982).

Since the beginning of the 20th century it has been recognised that the inhalation of short-lived ^{222}Rn progenies leads to an increase in lung cancer incidents, well known from uranium miners (George, 2007; Quindós Poncela et al., 2004a). The entry of ^{222}Rn into houses involves a health risk. For this reason, mapping of the ^{222}Rn indoor occurrence and the geogene ^{222}Rn potential was emphasized in the last decades (Appleton and Miles, 2010; Dubois et al., 2010; Ielsch et al., 2010; Kemski et al., 1996b, 2001). In Spain, national ^{222}Rn surveys began in 1988 with indoor measurements (Dubois, 2005; Quindós et al., 1991). Quindós Poncela et al. (2004b) presented the resulting ^{222}Rn map as well as a predicted indoor ^{222}Rn map based on the natural gamma radiation map of Spain (Marna Project). Based on these results ^{222}Rn surveys were initiated in the surroundings of Spanish nuclear power plants (Quindós Poncela et al., 2003; Sainz Fernandez et al., 2008), old uranium mines (Quindós Poncela et al., 2004a) and regions with noticeably high indoor ^{222}Rn concentrations (Quindos et al., 2005; Sainz et al., 2009). Additionally, Soto et al. (1995) measured ^{222}Rn in Spanish spas. So far, the ^{222}Rn activity in NW Spain was surveyed in natural spring water to determine the activity of latent faults (González-Díez et al., 2009). In the last decade, repeated moderate seismic activity was recorded in the Cantabrian Mountains, mainly associated with the Ventaniella Fault (VF) in the Riaño area (López-Fernández et al., 2004, 2008). During the first measurement program (June 2010) we carried out measurements of ^{222}Rn in soil gas in order to determine if the seismic activity of the VF is revealed in the ^{222}Rn activity within the soil gas. Traces perpendicular to the fault strikes were chosen. In order to compare the results we measured the ^{222}Rn activity above the Sabero-Gordón Fault (SGF). No seismic activity is reported in the area and therefore the fault is regarded as an aseismic fault, for which we expected a lower ^{222}Rn activity compared to the seismic active VF. During the second measurement program (September and October 2010) we focused mainly on a detailed investigation of the SGF area to confirm the elevated activities of ^{222}Rn across the SGF, which had been measured during the summer measurement program.

The objectives of this paper are (1) to report the ^{222}Rn activity related to a seismic active fault (VF) and an aseismic fault (SGF); (2) to conduct ^{222}Rn mapping according to Kemski et al. (1996b) in order to get a general idea of the ^{222}Rn background inside the research area and to identify potential structurally caused ^{222}Rn anomalies and (3) to show a potential relationship between petrophysical parameters and ^{222}Rn activity in soil gas.

3.2 Geological setting

The Cantabrian Mountains in NW Spain developed during the Variscan and Alpine Orogenies and an extensional regime in Mesozoic times. The Cantabrian Zone (Lotze, 1945) constitutes the core of the Ibero-Armorican Arc and represents the foreland thrust and fold belt of the Iberian Variszides (Fig. 3.1). The Cantabrian Zone consists mainly of Palaeozoic sediments which have been deformed by thin skinned tectonics (Bastida et al., 1984; Julivert, 1971; Marcos and Pulgar, 1982). The main deformation phase began in Namurian times (Hemleben and Reuther, 1980; Reuther, 1977) and proceeded until the upper Stephanian (Julivert, 1971). After the post-Variscan strike-slip regime and the Mesozoic extensional regime which gave rise to the generation of normal faults, the Alpine N–S compression caused further uplift of the Cantabrian Mountains and thrusting above the synorogenic Duero Basin. New folds and faults were generated and the pre-existing Variscan and Mesozoic faults were reactivated, e.g. the SGF and the Ubierna Fault in the southern mountain range and the Cabuérniga Fault in the north (Alonso et al., 1996). The internal structure of the geological units remained relatively undeformed (Gallastegui, 2000). Structurally, this can be explained by fault-bend-folding associated with the main thrust of the mountain range above the Duero Basin (Alonso et al., 1996). This main thrust is visible in the seismic profiles; the outcrop is mainly covered by younger Tertiary sediments except in vicinity of the River Cea (Pulgar et al., 1999). As a result of the uplift the dip of the Cretaceous and Tertiary sediments of the northern Duero Basin was steepened and the sediments were folded (Alonso et al., 1996; Evers, 1967; Hemleben and Reuther, 1980; Koopmans, 1962; Marín et al., 1995). In the vicinity of Boñar additional folding along the southern mountain margin was caused by the SGF (Gallastegui, 2000).

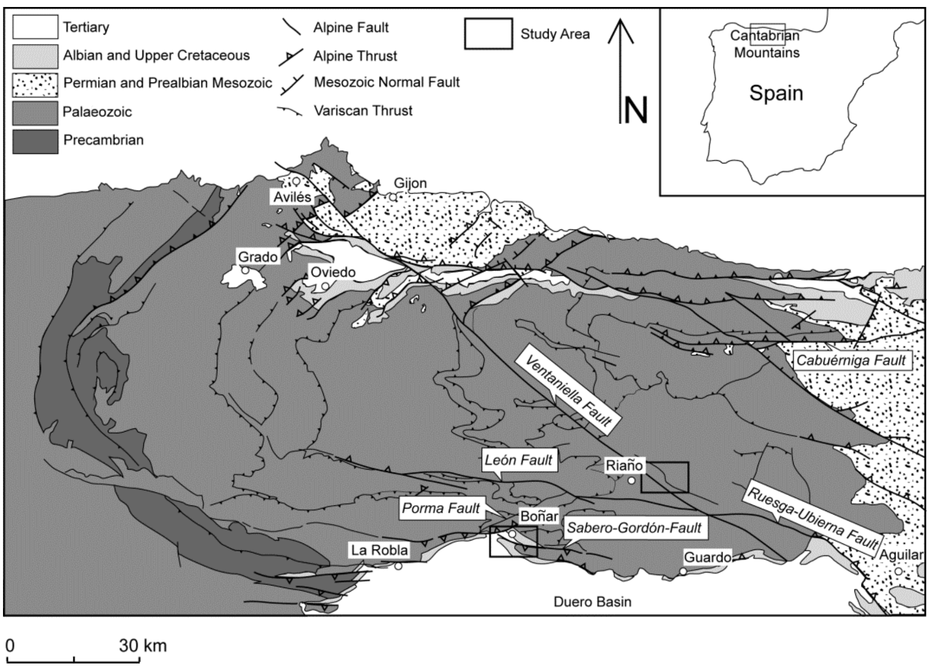

Fig. 3.1: Simplified geological map of the Cantabrian Zone showing the location of the research areas (modified after Alonso et al., 1996).

The major faults in the Cantabrian Zone are described by Julivert et al. (1981) as well as Lepvrier and Martínez-García (1990). The major faults in the Cantabrian Zone can be grouped according to their strike direction into E–W striking faults (León Fault and SGF), NW–SE striking faults (VF) and NE–SW striking faults (e.g. Porma Fault). In this work we investigated segments of the VF and the SGF, whose research histories are outlined in the following subsections.

3.2.1 Ventaniella Fault

The Ventaniella Fault (VF) extends by about 140 km in an NW–SE direction, crossing the entire Cantabrian Mountain range. Reference to the official geological maps of the region indicates that the VF cuts all previous structures including the Tertiary sedimentary succession (Arthaud and Matte, 1975; Julivert, 1971). The fault was first described by Julivert (1960) as a dextral decrochement fault (strike-slip-fault) of late Hercynian (Permian) age, which has been reactivated several times (Julivert, 1971; Lepvrier and Martínez-García, 1990). Alonso et al. (2007) describe the VF as an Alpine fault whereas Aller et al. (2002) attribute the generation of the fault to the Mesozoic opening of the Bay of Biscay. Along the fault, seismic activity is continually reported (Alonso et al., 2007; López-Fernández et al., 2004; 2008) particularly northeast of Avilés and near Riaño. In 1989, a 3.7 magnitude earthquake was recorded near El Puerto de Ventaniella (López-Fernández et al., 2004). During the GASPI project 1999–2002 it was found that the seismic events related to the VF near Riaño were of the average magnitude 2 (López-Fernández et al., 2004).

3.2.2 Sabero-Gordón Fault

The Sabero-Gordón Fault (SGF) extends in an E–W direction, parallel to the Cantabrian Mountain margin. The fault´s character and structural influence are still matters of discussion. The SGF was first mentioned by Evers (1967) as a facies boundary between thicker Devonian sediments in the north compared to the Devonian deposits in the south. Some authors characterise the SGF, including other major structural lines such as the Ventaniella (Cardaño) and León Fault, as fractures generated in late Hercynian times with multiple reactivations (Heward and Reading, 1980). Alonso et al. (1996), Kullmann and Schönenberg (1978), Nijman and Savage (1989) and Reijers (1985) describe a horizontal displacement along the SGF, which is linked to the basin genesis in Stephanian times (Sabero Coal basin). During the Alpine Orogeny the main thrust caused the reactivation of the SGF as a backthrust rotated by simple shear (Alonso et al., 1996). According to these authors the geological sections show a steep vertical dip which varies slightly (Alonso et al., 1996; Reijers, 1985). The timing of reactivation or reactivations remains unclear, but the geological map of Boñar shows a displacement of Tertiary formations caused by movement on the SGF (Alonso et al., 1990). However, no seismic activity has recently been reported for the SGF.

3.2.3 Overview of the research areas

The research areas were chosen after analysis of available geological and structural maps, our own structural field work and the interpretation of morphological features. The three chosen sites are located south of Boñar and in the village Boca de Huergano (Fig. 3.2a).

In the Veneros research area (Fig. 3.2b) three profiles “SG”, “S4” and “SAB” were investigated. The profiles extend across the SGF, north of the village Veneros, and were measured in soils above the Boñar Formation (upper Cretaceous) which consists of arenaceous limestones and marls (Evers, 1967), deposited during the Cenomanian transgression. The SGF marks the boundary between the Boñar Formation and molasse sediments in the south. The molasse sediments consist of alternating coarse- to fine-grained micaceous sandstones, greywackes, carbonaceous mudstones and coal beds (Comte, 1959; Evers, 1967). The soil cover is classified as an Alfisol, characterised by argillaceous accumulation horizons (http://sig.marm.es/siga/). The profiles in this area have a length of up to 45 m and could not be extended because of outcrops.

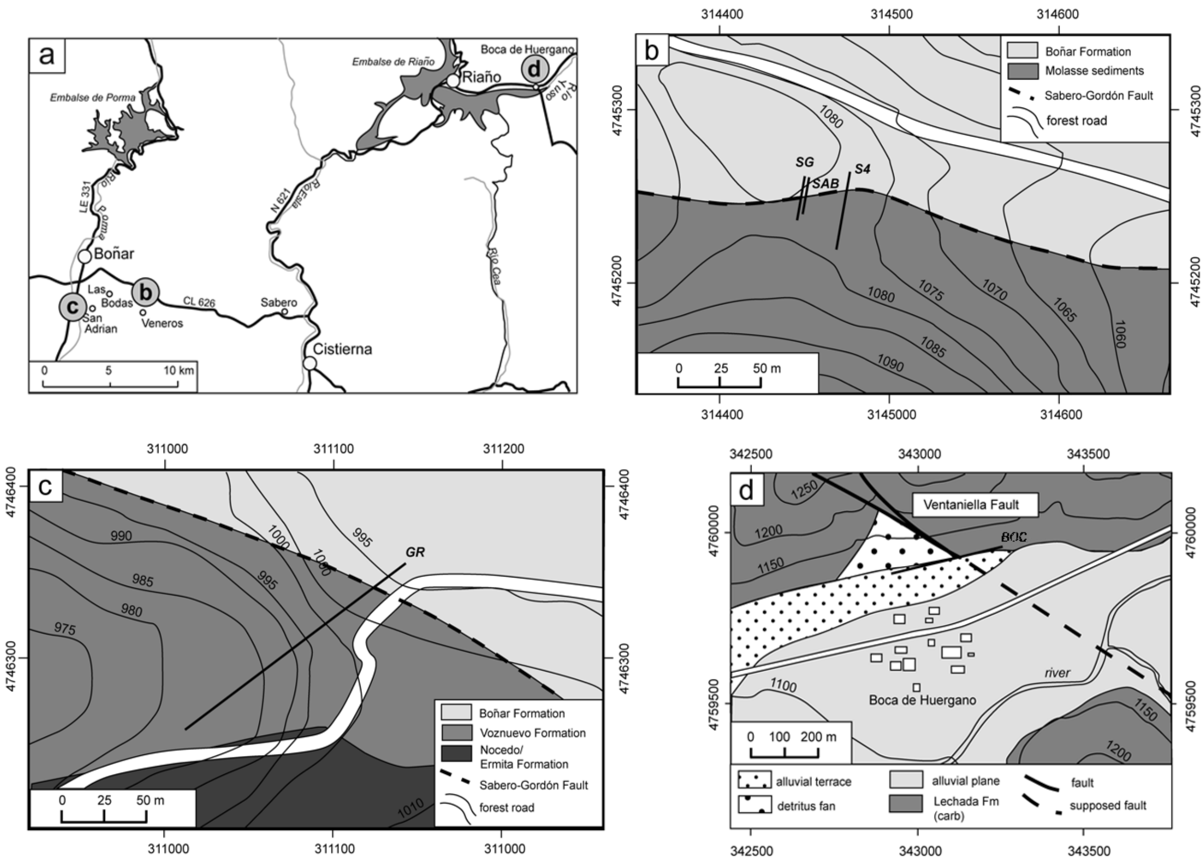

Fig. 3.2: (a) Geographical overview showing the locations (b,c,d) of the measured ^{222}Rn profiles; (b) traverses across the SGF north of Veneros; (c) traverse across the SGF west of San Adrian; (d) traverse across the VF in the village Boca de Huergano. Geological contours are taken from the 1:50 000 geological maps Boñar (b, c) (IGME, 1981) and Riaño (d) (Instituto Tecnológico GeoMinero de España, 1990).

The profile “GR” (Fig. 3.2c) is located to the west of the village San Adrian, near the river Porma. It crosses the Boñar Formation (upper Cretaceous) from north to south, the inferred trace of the SGF and the Voznuevo Formation with sediments from the lower part of the upper Cretaceous (Fig. 3.2c). The sediments predominantly consist of multicoloured sandstones with clay and gravel lenses and quartz pebbles (Evers, 1967). The soil cover can be characterised as an Entisol (http://sig.marm.es/siga/).

The research profile “BOC” (Fig. 3.2d) was chosen to run across the Ventaniella Fault north of the village Boca de Huergano, near Riaño. This profile has a length of 215 m and consists of 21 sampling points with distances varying from 5 to 20 m. The profile crosses greywackes and shales of Westphalian age, which build up the Lechada Formation (Van Veen, 1965), alluvial terraces formed by the River Yuso and gravity deposits (detritus fans) of mixed origin. The soil cover is assigned to the order Entisol, an ochreous sandy soil, with no remarkable horizons (http://sig.marm.es/siga/).

3.3 Material and Methods

^{222}Rn in soil gas was measured along lines perpendicular to the assumed subsurface fault trace at sampling points of equal spacing. In case of divergent ^{222}Rn values at adjacent sampling points, the distance between the points was reduced if repeat sampling visits were carried out. The length of the profiles was dependent on the accessibility of the area and the present soil cover. Table 3.1 summarises the dates of sampling, prevailing meteorological conditions, the profile lengths and the number of sampling points on the individual profiles. During the second measurement program (September and October 2010), a ^{222}Rn map was produced according to the method published by Kemski et al. (1996b).

Table 3.1: Overview of ^{222}Rn in soil gas profiles 2010.

Profile name	Date	Length m	*n**	T °C	± stdv	Atmos. press. hPa	± stdv	Air moist. %	± stdv
SG	Sep 10	25	8	25.3	1.6	947.8	3.2	39.3	2.6
SAB	Jun 10	20	5	25.3	1.4	947.5	0.8	42.7	3.5
S4	Oct 10	45	10	28.2	3.7	947.8	1.8	39.9	5.8
S4.2	Oct 10	10	5	21.0	0.0	946.0	0.0	43.6	0.8
GR	Oct 10	126	14	21.4	3.0	949.9	4.5	40.2	4.7
BOC	Jun 10	155	19	31.9	5.0	944.6	2.5	34.4	4.7

**n* = number of sampling points

3.3.1 Soil gas samples

The soil gas sampling and measurement of ^{222}Rn was conducted according to the protocol reported by Wiegand (2001). The principle is based on soil gas sampling and subsequent measurement of the samples in Lucas cells (Wiegand, 2001). In order to ensure the reproducibility of the results, each point was sampled twice. During the sampling, temperature, relative air moisture, atmospheric pressure, the time of sampling and sample volume were also recorded.

The soil gas extraction was carried out by grab sampling using iron pipes that were pushed into the ground to a depth of 100 cm and subsequently connected to a manual pump. The residual atmospheric air in the probe was evacuated by suction prior to sampling. A total volume of 120 ml of soil gas was drawn up into a syringe. The time required for filling the syringe was noted as an indication of the soil´s permeability. In order to minimize contamination of the soil gas samples by atmospheric air during the sampling procedure, 20 ml of the total volume of soil gas were released into the atmosphere and a quantity of 100 ml soil gas was injected into a Lucas cell with a volumetric capacity of 100 ml that had been evacuated prior to use.

After the equilibration time of a minimum of 3 h of ^{222}Rn and its short-lived alpha emitting daughter isotopes, the ^{222}Rn present in the soil gas sample was measured using the scintillation counter „Sisie" with a sensibility of 13.23 (impulses/min)/Bq/l and Lucas cells coated with silver activated ZnS(Ag). Calibration was achieved using an internal standard from the manufacturer. The alpha particles produced by the decay of Rn collide with the ZnS(Ag)-cover and the resulting light pulses can be counted by an alpha counter amplified with a photomultiplier tube (PMT). Each cell was measured for 120 seconds divided in six counting intervals of 15 s. The ^{222}Rn activity in 1 m^3 soil gas was calculated from the arithmetical mean of the 6 impulses measured per cell.

It is very likely that parts of the ^{222}Rn were lost during the sampling procedure. In addition to that, ^{222}Rn may be diluted by the atmospheric air. Therefore, we used the maximum value of the duplicate measurements for the data interpretation. In order to ensure that Rn activity at the surface is zero, control samples of atmospheric air at the sampling points were taken. The value of the ^{222}Rn concentration in the atmospheric samples was always negligible.

3.3.2 Soil samples

In the vicinity of the soil gas sampling points, soil samples were collected from a depth of 100 cm using an iron steel sampling tube. The lower 10 cm of the core were placed into a sealed hermetic plastic bag and placed in a cool box preventing evaporation. The water content was determined by drying the soil samples in an oven at T = 105 °C until a constant weight was reached. The wet bulk density was estimated by weighing 8 cm^3 of undisturbed soil core. The grain density was measured by kerosene-pycnometry. Approximately 7 g of the sample were placed into the pycnometer, which was subsequently filled with kerosene while continuously removing the air by a vacuum pump. The rock sample volume was calculated as the difference between the volume of kerosene in the pycnometer with and without the rock material. A detailed description of this method was given by

Koroleva et al. (2011). The dry bulk density was calculated using measured bulk wet density and natural moisture content. From the obtained values physical porosity was calculated.

3.4 Results and discussion

Table 3.2 shows the measured data and calculated results of both measurement programs. During summer 2010, the profiles “BOC” and “SAB” were sampled and the autumn measurement program comprises the traverses “SG”, “S4”, “S4.2”, “GR” and “GR2” (Table 3.2). The traverses “SAB” and “SG” were sampled at the same location. Traverse “GR2” and “S4.2” are constituted of repeatedly and additionally measured points of profile “GR” and “S4”, respectively.

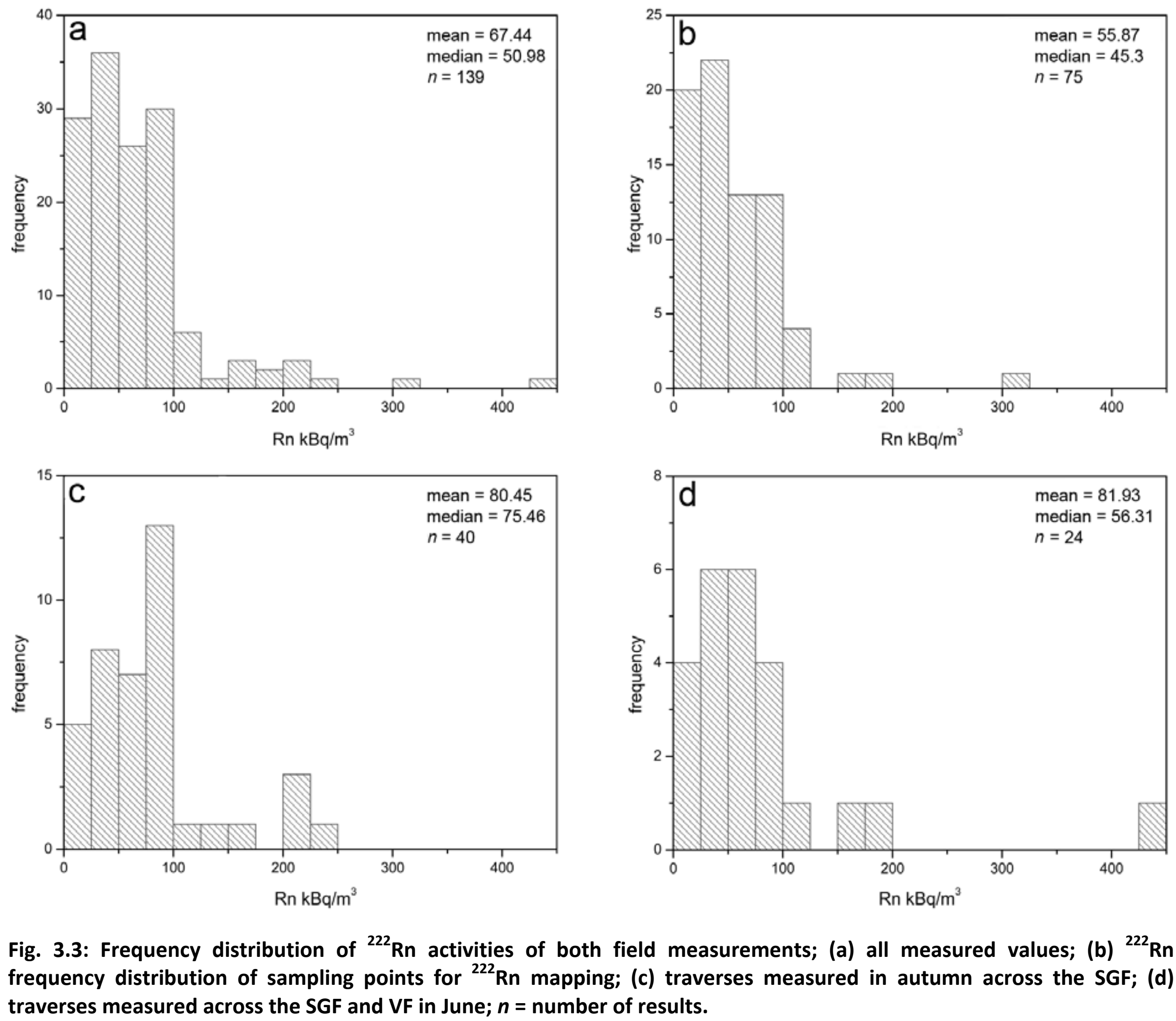

Fig. 3.3: Frequency distribution of ^{222}Rn activities of both field measurements; (a) all measured values; (b) ^{222}Rn frequency distribution of sampling points for ^{222}Rn mapping; (c) traverses measured in autumn across the SGF; (d) traverses measured across the SGF and VF in June; *n* = number of results.

The ^{222}Rn activities in soil gas range from 5 kBq/m^3 to 441 kBq/m^3. The arithmetic mean ^{222}Rn activity of all 139 sampled points acquired during both field measurements is 67 kBq/m^3 with a median value of 51 kBq/m^3 (Fig. 3.3a). Fig. 3.3b shows the frequency distribution of the ^{222}Rn activities obtained from the sampling of the geological formations for ^{222}Rn mapping, Fig. 3.3c shows the results of the traverses measured across the SGF during the autumn field measurements and Fig. 3.3d shows the ^{222}Rn activities of the measurements conducted in June across the VF and the SGF. The data distribution shows that high ^{222}Rn values occur more frequently in the traverses measured across faults compared to the ^{222}Rn values occurring in the geological formations. The ^{222}Rn activity across the investigated fault zones is highly variable and ranges from 10 kBq/m^3 up to 441 kBq/m^3. Areas not affected by faults show an arithmetic mean of 56 kBq/m^3 whereas the fault-related zones yield an arithmetic mean of 80 kBq/m^3 (autumn) and 82 kBq/m^3 (summer).

The water content of soil samples collected during both field measurements varied between 3.31 and 24.31 wt% with an average value of 9 wt% for the soil samples collected during the autumn field measurements, whereas the soil samples from June revealed an average value of 17 wt% (Table 3.2). The soil´s grain density varies from 2.58 to 2.81 g/cm^3 and the total porosity lies between 8.7 and 29.5 %. As expected, water content increases with increasing total porosity of soil samples. However, there is no correlation between water content and the activity of ^{222}Rn in soil gas.

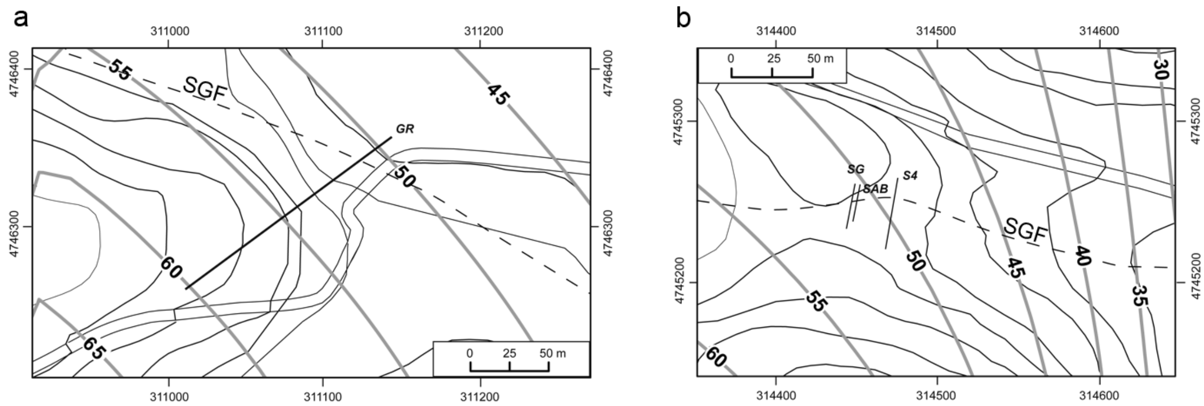

Fig. 3.4: ^{222}Rn maps of the research area across the SGF, grey lines with numbers show the ^{222}Rn distribution in kBq/m^3; (a) profile "GR" near San Adrian; (b) profiles near Veneros.

Fig. 3.4 shows two cutouts of the ^{222}Rn map created during the second field measurements in the SGF research area. The map sampling was carried out according to Kemski et al. (1996b). Each geological formation present in the research area was sampled at two different points. At each point, three sites, located in triangle and distanced from each other by 5 m were sampled twice. The countour maps with contour interval of 5 kBq/m^3 were prepared using the arithmetic mean of these six ^{222}Rn activities (Fig. 3.4a, b). The area belonging to the "GR" profile (Fig. 3.4a) is characterised by ^{222}Rn activities of 45–65 kBq/m^3. North of Veneros, the map (Fig. 3.4b) shows a similar ^{222}Rn in soil gas distribution inferred from the results of the formation measurements.

Table 3.2: Data collected during both measurement programs 2010.

Profile	Name	Distance	UTM-coordinates		^{222}Rn max[c]	Petrophysical soil parameters: Water content	Bulk density dry	Grain density	Total porosity
		m			kBq/m^3	wt%	g/cm^3	g/cm^3	%
Autumn measurement program September and October 2010									
SG	Sg1	0	314451	4745261	28	10.17	2.25	2.66	15.3
	Sg2	5	314450	4745256	22	7.46	1.87	2.65	29.5
	Sg3	7.5	314448	4745253	47				
	Sg4	10	314448	4745250	77	6.78	2.35	2.70	11.4
	Sg5	12.5	314448	4745248	88				
	Sg6	15	314444	4745241	87	6.91	2.34	2.64	11.5
	Sg7	20	314446	4745237	51	5.23	2.25	2.68	16.6
	Sg8	25	314448	4745232	35	6.41	2.47	2.71	8.7
S4	S4.1	0	314476	4745264	115	14.30	2.19	2.69	18.7
	S4.2	5	314478	4745252	202	11.05	2.25	2.69	16.2
	S4.3	10	314478	4745249	78	6.85	2.36	2.68	12.2
	S4.4	15	314478	4745246	88	9.21	2.32	2.77	16.4
	S4.5	20	314477	4745241	94	12.89	2.05	2.68	23.5
	S4.6	25	314479	4745236	79	8.10	2.38	2.81	15.4
	S4.7	30	314478	4745230	79	12.20	2.23	2.61	14.6
	S4.8	35	314476	4745225	32	11.58	2.24	2.66	15.9
	S4.9	40	314472	4745221	78	5.41	2.36	2.63	10.1
	S4.10	45	314471	4745215	34	8.17	2.36	2.59	9.0
S4.2	S42.1[a]	0	314478	4745259	133				
	S42.2[b]	2.5	314477	4745258	90				
	S42.3[a]	5	314477	4745257	212				
	S43.4[b]	7.5	314474	4745256	154				
	S43.5[a]	10	314477	4745251	76				
GR	GR1	0	311126	4746340	75				
	GR2	10	311119	4746335	57				
	GR3	20	311114	4746330	217	5.13	2.40	2.73	11.8
	GR4	30	311106	4746322	242	17.79	2.18	2.73	20.1
	GR5	40	311095	4746316	66	7.05	2.41	2.75	12.6
	GR6	50	311090	4746309	21				
	GR7	60	311078	4746306	13				
	GR8	70	311071	4746295	41				
	GR9	80	311062	4746293	22				
	GR10	88	311064	4746290	38				
	GR11	96	311054	4746282	10				
	GR12	106	311036	4746262	73				
	GR13	116	311033	4746276	71				
	GR14	126	311025	4746270	63				
GR2	GR2.1[a]	35	311101	4746317	90				
	GR2.2[b]	15	311114	4746331	92				
	GR2.3[b]	10	311130	4746351	45				
Summer measurement program June 2010									
BOC	1Boc	0	342991	4759906	40				
	3Boc	20	343013	4759905	75				
	4Boc	30	343024	4759904	100	24.31		2.73	
	5Boc	40	343031	4759904	99				
	6Boc	50	343043	4759907	30				
	7Boc	60	343052	4759914	23				
	8Boc	70	343062	4759914	73	21.30		2.67	
	9Boc	80	343073	4759917	52				
	10Boc	90	343081	4759919	51				
	11Boc	100	343091	4759920	36				
	12Boc	110	343101	4759921	21				
	15Boc	145	343132	4759930	106	21.03		2.64	
	16Boc	155	343143	4759933	90				
	18 Boc	165	343158	4759928	23				
	19 Boc	175	343166	4759933	22				
	20Boc	185	343178	4759934	38				
	21Boc	195	343187	4759936	61	17.38		2.74	
	22Boc	205	343197	4759938	37				
	23Boc	215	343205	4759945	34				
SAB	Sab1	0	314469	4745279	92	19.81		2.72	
	Sab2	10	314448	4745253	74				
	Sab3	20	314450	4745247	441	11.17		2.72	
	Sab4	30	314444	4745240	181				
	Sab5	40	314446	4745229	168	6.16		2.63	

[a] repeatedly sampled points; [b] additionally sampled points; [c] positive relative standard deviation is about 20–30% for 1–20 kBq/m^3; 10–20% for 20–40 kBq/m^3 and ≤10% for results > 40 kBq/m^3

The ^{222}Rn profiles obtained (Fig. 3.5) can be described as follows:

a)

The measured ^{222}Rn activity in soil gas along profile “GR” ranges from 10 to 242 kBq/m^3. The highest values form a clearly defined peak between 20 and 30 m along the chosen trace. The maximum ^{222}Rn activity is about 5 times higher than the background value resulting from ^{222}Rn values excluding the maximum concentrations which show an arithmetic mean of 49 kBq/m^3 (Fig. 3.5a). The results of the ^{222}Rn soil gas map are comparable background values between 50 and 60 kBq/m^3 (Fig. 3.4a). Three additional points were sampled to get a higher resolution in the zone of elevated ^{222}Rn concentrations. The sampling took place one day after the first sampling under the same meteorological conditions. To compare the data of both sampling days, the 10 m distance point was sampled on both visits. The results of the duplicate measurements vary only marginally (by 12 kBq/m^3) and the additional points, at a 15 and 35 m distance support the existence of a confined zone with high ^{222}Rn activity.

b)

The three profiles (Fig. 3.2b, 3.4b) near Veneros are aligned in an N–S direction and are separated from each other by approximately 10–20 m. Profile “S4” (Fig. 3.5b) is the easternmost trace and expands up to 45 m in length. The distances between sampling points are 5 m. Fig. 3.5b shows that a clearly defined zone of elevated ^{222}Rn activities at 5 m distance can be distinguished with a maximum value of 202 kBq/m^3. The residual values next to the peak show an arithmetic mean of 80 kBq/m^3, whereas the ^{222}Rn map gives a background of 50 kBq/m^3 (Fig. 3.4b). As in profile “GR”, repeat and additional measurements were taken along the first 10 meters of the profile one day after the first measurement, under the same meteorological conditions. The repeated values (0, 5 and 10 m) and additional values (2.5 and 7.5 m) confirm the trend previously observed (Fig. 3.5b).

c, d)

The profiles “SAB” and “SG” (Fig. 3.5c, 3.5d) are located 25 m west of traverse “S4” (Fig. 3.2b, 3.4b). Fig. 3.5c shows the traverse “SAB” sampled during the first field measurements in June 2010. The ^{222}Rn activity ranges from 74 up to 441 kBq/m^3, which is the highest activity measured during both field measurements. Compared to the arithmetical mean of the values excluding the peak (130 kBq/m^3), the maximum value of 441 kBq/m^3 is of the order of 3 times higher.

The same traverse was sampled 4 months later during the second field measurements (Fig. 3.5d). The “SG” profile reveals maximum ^{222}Rn activities at 10–15 m distance with 88 kBq/m^3 and minimum values of 22 kBq/m^3 at 5 m distance. The values beyond the zone of elevated ^{222}Rn activity reveal an arithmetic mean of 28 kBq/m^3, so the maximum values are approximately 3 times higher than the background values. The ^{222}Rn mapping of the geological formations in the research area yields background values between 45 and 55 kBq/m^3. These values differ from the above-mentioned background values, 80 kBq/m^3 (S4, Fig. 3.5b), 30 kBq/m^3 (SG, Fig. 3.5d) and 130 kBq/m^3 (SAB, Fig. 3.5c).

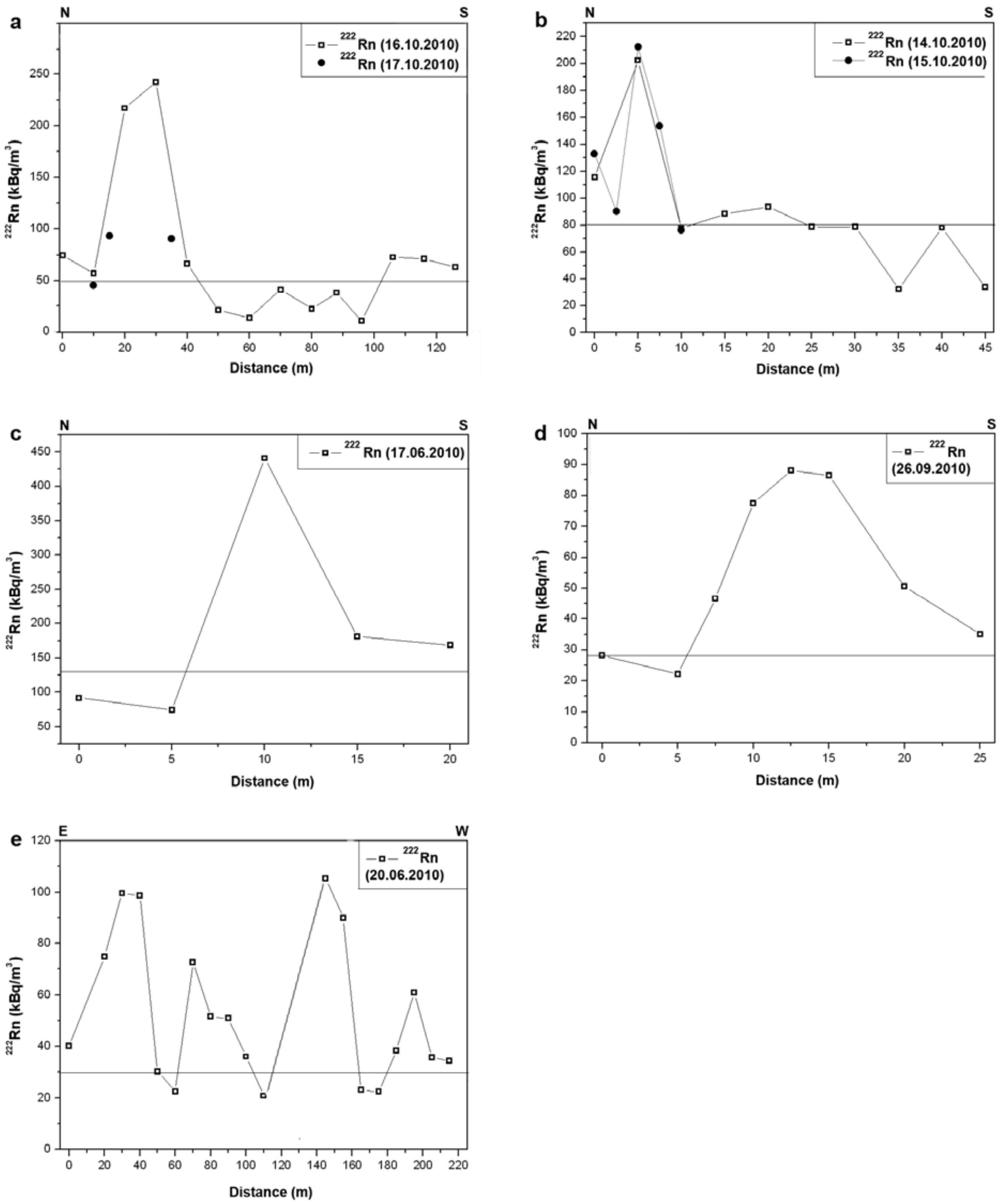

Fig. 3.5: ^{222}Rn profiles across the SGF and VF, the solid horizontal line represents average background value, achieved from the arithmetic mean for points measured outside the peaks; (a) profile "GR" (16.10.2010) across the SGF with three additionally sampled points ("GR.2", 17.10.2010); (b) profile "S4" (14.10.2010) and profile "S4.2" (15.10.2010) across the SGF; (c) profile "SAB" across the SGF in June 2010; (d) profile "SG" across the SGF; (e) profile "BOC" across the VF in June 2010.

e)

In contrast to the profiles presented above, four peaks can be identified along the traverse “BOC”, at 20–40 m, 70–100 m, 145–155 m and 195 m distances (Fig. 3.5e). The maximum ^{222}Rn concentrations range between 60 and 106 kBq/m^3. For this profile, we cannot present a ^{222}Rn map to get insight into the inert ^{222}Rn activity of the underlying geology. Hence, related to the measured ^{222}Rn activities beyond the zones of elevated ^{222}Rn concentrations a background value of 30 kBq/m^3 results. The ^{222}Rn activity at a distance of 145 m is about 3.5 times higher.

Comparison of the graphs evidently shows well defined peaks, which form the maximum ^{222}Rn values in the traverses across the SGF. In four measured profiles (Fig. 3.5a, b, c and d) the “single peak feature”, which is commonly reported in the literature clearly occurs. Across the VF, there are four zones of elevated ^{222}Rn activities in soil gas. Fig. 3.5c, d show results which were obtained at the same location during the summer (3.5c) and autumn (3.5d) field measurements. Both ^{222}Rn profiles show a well defined zone with elevated ^{222}Rn activity which increases fourfold in the space of 5 m (3.5c) and 7 m (3.5d). However, in the first case (3.5c) the maximum activity is 441 kBq/m^3, which is contrasted by a maximum value of 80 kBq/m^3 in the second case. Comparison of the two data sets gives further details: the maximum ^{222}Rn activity of profile “SAB” (3.5c) was registered at a 10 m distance and approaches the background at a distance of 15 m, while for the second case, the maximum appears at a distance of approx. 12 m, and the concentration value decreases slowly until it reaches the background at a distance of approximately 25 m. Visually, the graph shape appears broader in the second case compared to the first one.
Previously, studies at different sites (e.g. Kemski, 1993; Richon et al., 2011) show that after emanation to the available pore space, ^{222}Rn migration to the earth´s surface occurs mainly by two processes, diffusion and advection. Diffusion means ^{222}Rn migration is mainly through pores, and the source of ^{222}Rn is the geochemistry of the bedrock (Kemski, 1993; Richon et al., 2010). The diffusive migration of ^{222}Rn leads to migration distances of a few metres under standard conditions (Tanner, 1964). While diffusion depends on the geochemistry of the lithology and therefore represents the ^{222}Rn background of a sample point, advection is dependent on the geological structure, especially on potential migration paths and the availability of carrier gases. ^{222}Rn migration due to advection is the mechanism which accounts for long distance transport, resulting in spatially restricted ^{222}Rn activities in soil gas, occurring in particular above active faults. Brittle deformation in the subsoil accounts for an increase of ^{222}Rn released into soil gas as it leads to the generation of pathways (joints, cracks, etc.). The breakup of rock compounds further supports an increase of the inner surface, which in turn causes the cumulative release of ^{222}Rn (Kemski, 1993; King, 1986). The diffusive and advective migration process can be superimposed upon each other.

Based on the results obtained, the hypothesis may be put forward that the measured ^{222}Rn originates from deeper geological formations. Hence, in order to identify active faults by their ^{222}Rn in soil gas activity it is important to separate the measured ^{222}Rn signal into its components. In our case, where no data of radionuclide content in the subsoil is available, a probabilistic approach to rule out that the measured ^{222}Rn activity is higher than the diffusive one, seems appropriate. Therefore, we applied two different ways to identify possible intense ^{222}Rn signals caused by the underlying structure. The background values resulting from ^{222}Rn mapping (Fig. 3.4a, b) provide an approach to the zones which could not be sampled, but as is obvious from the profile sections, the ^{222}Rn activity can vary within a few metres due to structural circumstances as well as inhomogeneous soil permeability. For a given profile, background values resulting from the arithmetical mean of the values excluding peak values give a more reasonable indication of the local ^{222}Rn background signature. The fact that the same measurement points sampled during both field measurements show the same trend in the ^{222}Rn pattern but the resulting values of the summer study are about 5 times higher strongly suggests an advective ^{222}Rn migration process.

The difference within the patterns obtained from the ^{222}Rn values related to the seismically inactive SGF (“single peak feature”) and the seismically active VF with 4 peaks of maximum ^{222}Rn activities alternating with background values, is evident. From a comparison of the profiles “BOC” (Fig. 3.5e) and “GR” (Fig. 3.5a) it becomes apparent that the different patterns are not an effect of the profile resolution. The multiple ^{222}Rn maxima positions in the profile “BOC” may be explained by the fact that large faults do not usually occur as discrete surfaces, but instead, form a braided fracture zone (Hickman et al., 1995). Further support is given by Holub and Brady (1981), who investigated the ^{222}Rn emanation of rock under uniaxial stress conditions. Episodic variation of the stress intensity can lead to the occurrence of microcracks and to healing phenomena on older cracks. This would lead to an increase and a decrease of the ^{222}Rn emanation rate, respectively (Hickman et al., 1995; Holub and Brady, 1981). The generation of microcracks leads to a further increase in possible pathways for gas migration. Opening and closing of microcracks, due to seismic activity or tectonic stress, provides a rationale for the differences in the maximum position of the ^{222}Rn values in the profiles “SAB” and “SG”(Fig. 3.5c, d), which were measured at the same location in summer and autumn, respectively. Although from a seismic point of view the SGF is regarded as inactive, the different ^{222}Rn values suggest active fault slip which is too slow to radiate seismic waves (Roeloffs, 1999). The high ^{222}Rn activity of 440 kBq/m^3 agrees with the suggestion of an aseismic movement, owing to the fact that ^{222}Rn in soil gas measured across faults in seismic inactive areas usually reveal very low ^{222}Rn activities. These faults are consequently regarded as sealed faults, preventing gas migration (Lombardi and Voltattorni, 2010). In the investigated research area, the average direction of the maximal principal stress direction is about 140° (Cloetingh et al., 2005), which could facilitate creeping in the Sabero-Gordón weakness zone. An alternative explanation for the high ^{222}Rn activity measured across the SGF in June is given by Kristiansson and Malmqvist (1982), who argue with the formation of microbubbles occurring in fault zones. Their study reveals that by the escape of different terrestrial gases through waterfilled fractures, rising microbubbles pick up ^{222}Rn atoms from the geological environment on their way up, which leads to an accumulation of ^{222}Rn in soil gas, without requiring a specific ^{222}Rn source or very fast migration velocities necessitated by ^{222}Rn from deep uranium bearing rocks (Etiope and Lombardi, 1995). For the present data, the shift of the ^{222}Rn maxima position and the difference of the ^{222}Rn maxima values between the June and autumn field works can plausibly be explained by the healing of older pathways and the generation of new ones, leading to different zones of high permeability. The intensity of a ^{222}Rn signal in soil gas beneath the earth´s surface and the ^{222}Rn exhalation into the atmosphere is further heavily influenced by the soil´s physical properties and meteorological conditions such as air moisture content, temperature, atmospheric pressure and precipitation (Ioannides et al., 2003; Kemski, 1993; Kraner, 1964). The studies of King and Minissale (1994) and Washington and Rose (1992) describe the seasonal variability in ^{222}Rn activity in soils due to the water content in soil pores, which is controlled by meteorological parameters. Washington and Rose (1992) quantified the seasonal ^{222}Rn variability in soil gas in Pennsylvania and reported low winter ^{222}Rn values with 10–50% of the ^{222}Rn activity measured during summer. The results of these annual surveys do not reveal consistent trends, as according to geographic location and soil properties of the sample site the winter values can also be higher than the summer values (King and Minissale, 1994). Temperature, atmospheric pressure and air moisture varied only slightly during our field measurements (Table 3.1), whereas the precipitation rate fluctuated. During June 2010, the total precipitation was 57.9 mm, distributed across eleven days of rainfall. Our survey started after the precipitation period, as noticed during the sampling procedure from low groundwater levels and the water content of the soil samples. The monthly precipitation was 38.7 mm (6 days) and 59.3 mm (11 days) for September and October, respectively (ftp://ftpdatos.aemet.es/series_climatologicas/valores_mensuales/annual/). The second survey began in September after a dry period and continued until the end of October with several periods of rainfall. After the first precipitation event we measured a previously sampled point to reveal if we were able to quantify the impact of the meteorological change in the soil gas ^{222}Rn record. The results showed no significant change of ^{222}Rn values. Correlating all measured ^{222}Rn activities with the moisture content of soil samples (Table 3.2) did not evidence any coherency as reported e.g. in Papastefanou (2010). Our measurements took place in summer and autumn 2010. Comparing the traverses “SG” and “SAB”, the summer values are clearly higher than the autumn values, differing by a factor which is not reflected in the water content of soil samples collected at the sampling points. Nevertheless, in summer and autumn, a zone of elevated ^{222}Rn in soil gas is evident at the same location. As the radionuclide content in the subsoil, which causes the diffusive ^{222}Rn signal in soil gas, is supposed to be stable under unaltered moisture content of the soil, the difference in the height of the ^{222}Rn activities measured during both field measurements accounts for an advective transport of ^{222}Rn in soil gas.

3.5 Conclusions

During two measurement programs we investigated ^{222}Rn activity in soil gas across two faults in the Cantabrian Mountains, the seismically active VF and the seismically inactive SGF. Both faults can be traced in the soil gas by elevated ^{222}Rn activities. Zones of ^{222}Rn maxima can be distinguished from background values obtained from ^{222}Rn mapping of the geological formations and from the arithmetic mean of ^{222}Rn values at sites being located outside the zones of the maxima. The ^{222}Rn mapping gives broad information about the ^{222}Rn distribution in soil gas in the investigated area. However, the ^{222}Rn profiles require a higher resolution.

Across the SGF, the ^{222}Rn maximum signals differ by a factor of 5 between summer and autumn. From the data presented in this work we do not observe any correlation between ^{222}Rn in soil gas and petrophysical soil parameters or meteorological influences, which could be responsible for the observed change. Both, the difference and the shift of the position of ^{222}Rn maxima give the reason to suppose that the elevated concentrations of ^{222}Rn in soil gas across the SGF are a result of ^{222}Rn migration from a deeper source towards the surface by advection. A possible mechanism is the active formation of pathways for gas migration by aseismic fault slip of the SGF under the present tectonic stress regime. Comparing the results of the measured traverses over both investigated fault segments, it is evident that the magnitude of ^{222}Rn activities in soil gas in these cases does not reveal if a fault is aseismic or seismic.

4 Palaeostress patterns in the southern Cantabrian Mountains, NW Spain

Manuscript in preparation

Abstract

The Cantabrian Mountains in NW Spain experienced a complex geodynamic history which started with the Variscan Orogeny. Due to the following changes of the plate tectonic configuration induced by the breakup of Pangaea and the progressive opening of the Atlantic Ocean, different stress fields affected Iberia. The northern Iberian margin experienced a passive margin stage during the opening of the Bay of Biscay, constituted a plate boundary from late Cretaceous to Eocene with the development of a subduction zone and finally was strongly influenced by the Pyrenean compression. The present rocks in the Cantabrian Mountains are predominantly of Palaeozoic ages and were subjected to and deformed by the stresses acting on them throughout the time. This complicates the analysis of fault-striae data in terms of recent palaeostress reconstruction, as the resulting stress patterns are difficult to arrange chronologically. Nevertheless, a quantitative palaeostress reconstruction was carried out in the present work and the results show that the dominant post-Variscan stress directions reported for the Iberian Peninsula are equally preserved in the southern Cantabrian Mountains. The most recent maximum horizontal compression direction is oriented N–S to NW–SE.

4.1 Introduction

Intraplate-deformation is principally based on stresses induced by active plate tectonic forces on plate boundaries. The former Iberian microplate is nowadays attached to the Eurasian Plate. Due to its position in western Europe, the tectonic stress field acting on the Iberian Peninsula is governed by the convergence between the African and European plates and additionally by ridge-push forces of the Atlantic mid-ocean ridge. The research area is located in the southern Cantabrian Mountains that extend parallel to the northern margin of the Iberian Peninsula. With respect to Mesozoic to recent deformations, little has been published about palaeostress analysis based on fault-striae data in the Cantabrian Zone. Possibly, this is due to the predominant outcrop of Palaeozoic rocks and the complex geological history of the Cantabrian Mountains. The regional main faults cutting through the area of investigation display the intricate geological evolution. The main faults were generated during the Variscan Orogeny as well as Mesozoic extensional tectonics and were reactivated during Cenozoic times. Evidence of active deformation in the Variscan basement is given by the recorded seismic events. In the last decade, moderate seismic activity has been documented in the Cantabrian Mountains, mainly associated with the Ventaniella Fault (VF) as reported by López-Fernández et al. (2004, 2008). The current stress state of the Iberian Peninsula is generally characterised by NW–SE horizontal compression as indicated by the present-day stress map (Jabaloy et al., 2002; Müller et al., 1992; Zoback, 1992) and the analysis of palaeostress data and focal earthquake mechanisms (Herraiz et al., 1998). De Vicente et al. (2008) and DeMets et al. (1990) describe a NW–SE convergence of 3–6 mm/a of the Eurasian and African plates. According to Herraiz et al. (2000), the north-eastern part of the Iberian Peninsula actually undergoes mainly N–S to NE–SW compression, and the south-eastern part an E–W compression.

In 2010 ^{222}Rn activity in soil gas was measured across the seismic active VF and the Sabero-Gordón Fault (SGF) (Künze et al., 2012). The results indicate elevated ^{222}Rn in soil gas activity of the SGF compared to the VF and active genesis of pathways for gas migration driven by aseismic fault slip was proposed, causing these elevated concentrations. In the present study a quantitative palaeostress analysis is presented in order to obtain information on the recent crustal stress orientations in the southern Cantabrian Mountains and northern Duero Basin. The objectives of this analysis are to detect the orientation of palaeostress patterns and if possible, to elucidate the chronological order of these patterns.

4.2 Geological setting

The Cantabrian Mountains in NW Spain evolved during the Variscan and Alpine Orogenies and an extensional regime in Mesozoic times. The Cantabrian Zone (Lotze, 1945) is situated in the core of the Ibero-Armorican Arc and represents the Palaeozoic foreland thrust and fold belt of the Iberian Variszides (Fig. 4.1).

The Alpine cycle was initiated with the onset of Permo-Triassic rifting and basin development (Alonso et al., 1996; Lepvrier and Martínez-García, 1990). In the Cantabrian Zone, evidence of Alpine deformation is given by structural relationships between the Variscan basement and the surrounding Permo-Mesozoic cover (Pulgar et al., 1999). The stresses, which were induced by the Alpine Orogeny, caused the uplift of the Cantabrian Mountains above the synorogenic Duero basin in the south and the Bay of Biscay in the north (Alonso et al., 1996). Pre-existing structures were reactivated and the Mesozoic basins inverted. Fig. 4.1 shows the location of the research area at the southern rim of the Cantabrian Mountains. In the following a short outline is given of the Mesozoic to recent tectonic events influencing Iberia and especially the northern Iberian margin.

The Mesozoic is characterised by extensional tectonics, mainly influenced by the opening of the North Atlantic Ocean. At the beginning of the Mesozoic, Iberia was an independent microplate moving along the Azores-Gibraltar plate boundary in the south and the North Pyrenean Fault in the north (Vergés et al., 2002). The northern Iberian margin experienced a continental rift phase followed by a passive margin stage during the rifting and opening of the Bay of Biscay by seafloor spreading (Boillot and Malod, 1988).

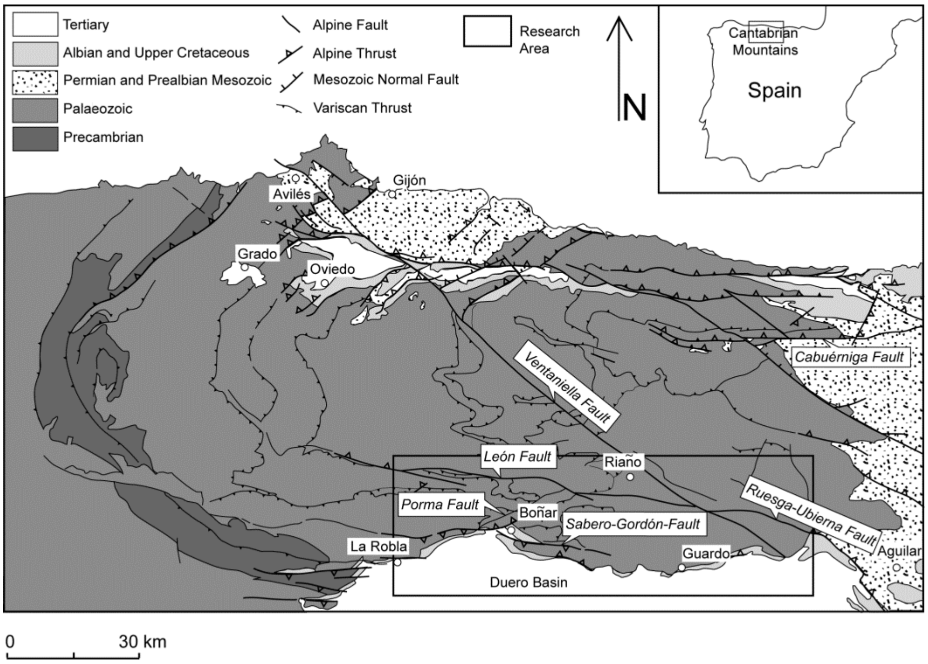

Fig. 4.1: Simplified geological map of the Cantabrian Zone showing the location of the research area (modified after Alonso et al. (1996); Künze et al. (2012).

The continental rift phase started with a NE–SW extension turning into a NW–SE extension prior to the rifting in the Bay of Biscay. NW–SE striking faults as the Ventaniella and Ubierna Faults are assigned as normal faults that developed during NE–SW extension (Boillot, 1986). Other authors interpret these structures as strike-slip faults connecting pull-apart basins in a segmented rift zone (Malod and Mauffret, 1990; Olivet et al., 1984). This rift zone developed during the later SE motion of Iberia with respect to Eurasia. The end of the continental rifting stage at the northern Iberian margin is marked by the formation of oceanic crust in the Bay of Biscay in late Aptian times (Malod and Mauffret, 1990). The opening of the Bay of Biscay is linked to the former gradual opening of the central and northern Atlantic, which had caused an anticlockwise rotation of Iberia with respect to the Eurasian plate of approximately 30° (Sanz de Galdeano, 1996). Between 120–80 Ma (Choukrone, 1992; Roest and Srivastava, 1991; Rosenbaum et al., 2002) oceanic lithosphere was produced in the Bay of Biscay, inducing a change from the former left lateral strike-slip motion to a left lateral-transpressive regime (Rosenbaum et al., 2002). The formation of oceanic crust in the Bay of Biscay proceeded until the Campanian (Sanz de Galdeano, 1996). Between 84–42 Ma Iberia was attached to Africa and the plate boundary between Eurasia and Africa (with Iberia) coincided with the North Pyrenean Fault (De Vicente et al., 2008; Roest and Srivastava, 1991). In the western segments, the initial divergent displacement changed progressively to a strike-slip type one (De Vicente et al., 2008). An active southward subduction of oceanic crust in the Bay of Biscay initiated during the latest Cretaceous to early Eocene and led to the uplift of the Cantabrian Mountains (Boillot and Capdevila, 1977; Boillot and Malod, 1988). According to Sanz de Galdeano (1996) the convergent movements between the African and Eurasian plate during the late Cretaceous initiated the generation of the first nappes in the Eastern Pyrenees. The Cantabrian subduction ceased at 54 Ma (Eocene) (Andeweg, 2002) and the compressive deformation migrated southwards (Huerta et al., 1996). According to De Vicente et al. (2008), a continental collision at the Pyrenean part of the margin was initiated by this time. As a result a fundamental change in the regional tectonic regime took place as the triple point between North America, Eurasia and Africa turned from Ridge-Ridge-Ridge to Ridge-Ridge-Fault (De Vicente et al., 2008).

At the beginning of the Cenozoic Iberia was affected by N–S compressive movements induced by the African-Eurasian convergence. According to Roure et al. (1989) and Sanz de Galdeano (1996) the Eocene compression led to the northward subduction of the Iberian plate beneath the European plate (Fig. 4.2c). Other authors such as Boillot and Capdevila (1977) report a partial southward subduction of the Pyrenean realm beneath the Iberian plate and interpret the Cantabrian subduction as the western prolongation (Fig. 4.2a).

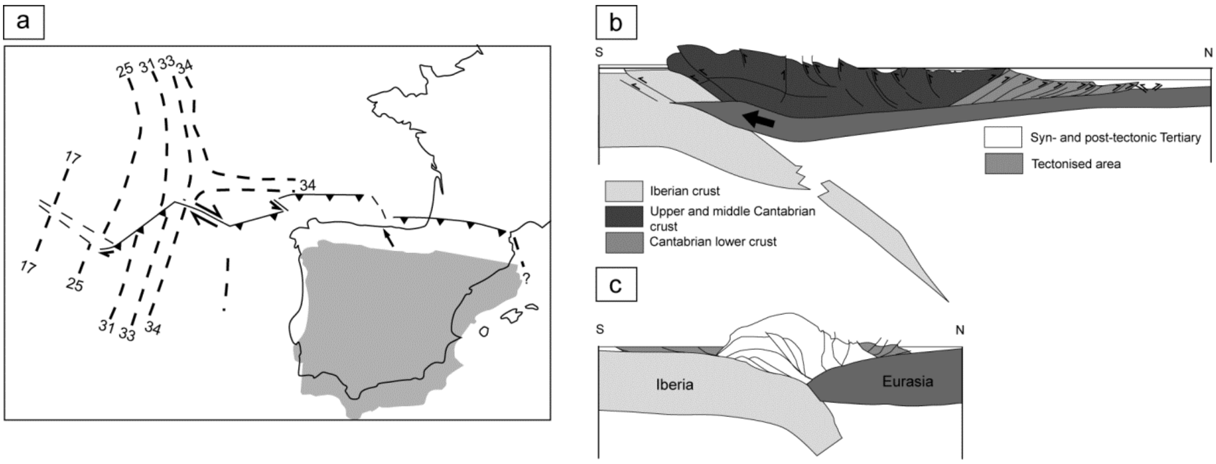

Fig. 4.2: (a) Model of Eocene plate tectonic setting of the northern Iberian margin. The location of Iberia at isochron 33 is shown in grey, the arrow indicates the Palaeocene to Eocene movement of Iberia, after Boillot and Malod (1988); (b) deep structure model of the Cantabrian Mountains modified after Gallastegui (2000); (c) deep structure of the Pyrenees (Muñoz et al., 1996).

More recent investigations based on seismic profiles divide the Pyrenees in a north verging- and south verging zone and report underthrusting of the Iberian crust below the European one (De Vicente and Vegas, 2009) (Fig. 4.3). Deep structure models of the Cantabrian Mountains and the Pyrenees reveal similar situations and the overthrust of the Cantabrian range above the Duero basin may be considered as the prolongation of the South Pyrenean frontal thrust (De Vicente and Vegas, 2009) (Fig. 4.2b, c). N–S and NW–SE compressions in the Pyrenees continued in Oligocene times, whereas the deformation processes mitigated in the western prolongation. Additionally to the convergence of Africa and Europe, an E–W extension affected central Europe and continued during the Neogene (Sanz de Galdeano, 1996). The Betic Internal Zones collided with southeastern Iberia during the Neogene (Jabaloy et al., 2002). A compilation of the most recent tectonic influences on Iberia is shown in Fig. 4.3.

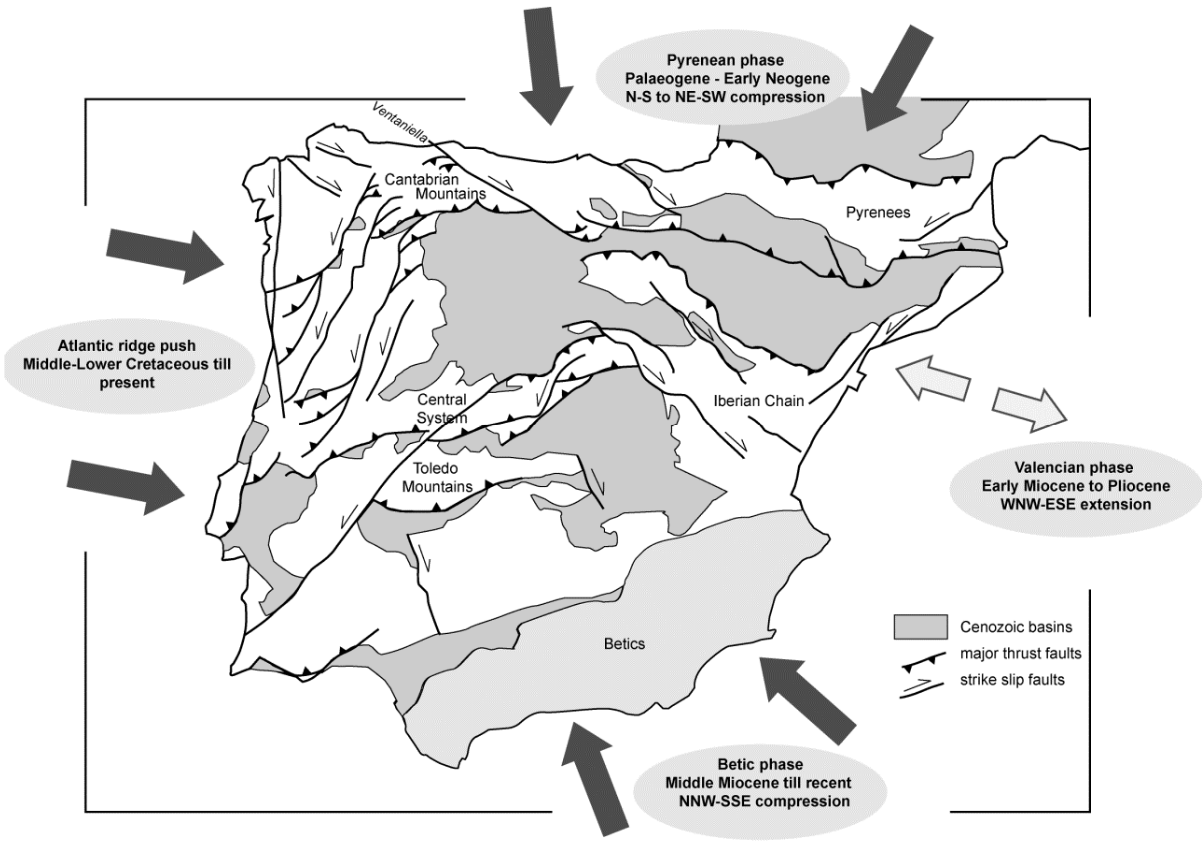

Fig. 4.3: Plate tectonic setting and chronology of influences on Iberia, modified after Cloetingh et al. (2002) and De Vicente and Vegas (2009).

In summary, the processes related to the opening and subsequent closing of the Bay of Biscay and the overall later convergence between the African plate and the Eurasian plate led to a counter-clockwise rotation of Iberia with respect to Eurasia, which caused a NE–SW compression (e.g. Andeweg, 2002; Van der Voo, 1969; Vergés et al., 2002). At the southern margin of Iberia (Azores-Gibraltar Fracture Zone) the Africa-Eurasia boundary is active since the early Miocene (Roest and Srivastava, 1991). The direction of convergence between Africa and Europe turned from NNE to NNW to the present convergence direction of NW (De Vicente et al., 2008). The deformation induced by collision at the northern margin of Iberia was transferred to the interior of the Iberian plate. The overall directions of the maximum horizontal stress (Shmax) range from N–S, NE–SW, E–W to NW–SE (De Vicente et al., 2005). Evidence of active deformation in the research area is given by the seismic events recorded there (Fig. 4.4).

The major faults in the Cantabrian Zone were described by Julivert et al. (1981) as well as Lepvrier and Martínez-García (1990) (Fig. 4.1, Fig. 4.4). These faults can be grouped according to their strike direction into E–W striking faults (León Fault and SGF) and NW–SE striking faults (VF), which are described below. The outcrops analysed in the present study are located around the León Fault, the Sabero-Gordón Fault, Ventaniella Fault and Porma Fault. The NE–SW striking faults (e.g. Porma Fault) are not specifically discussed in this work. A short literature review with respect to the generation and activity of the major faults important for the present work is given in subsequent sections.

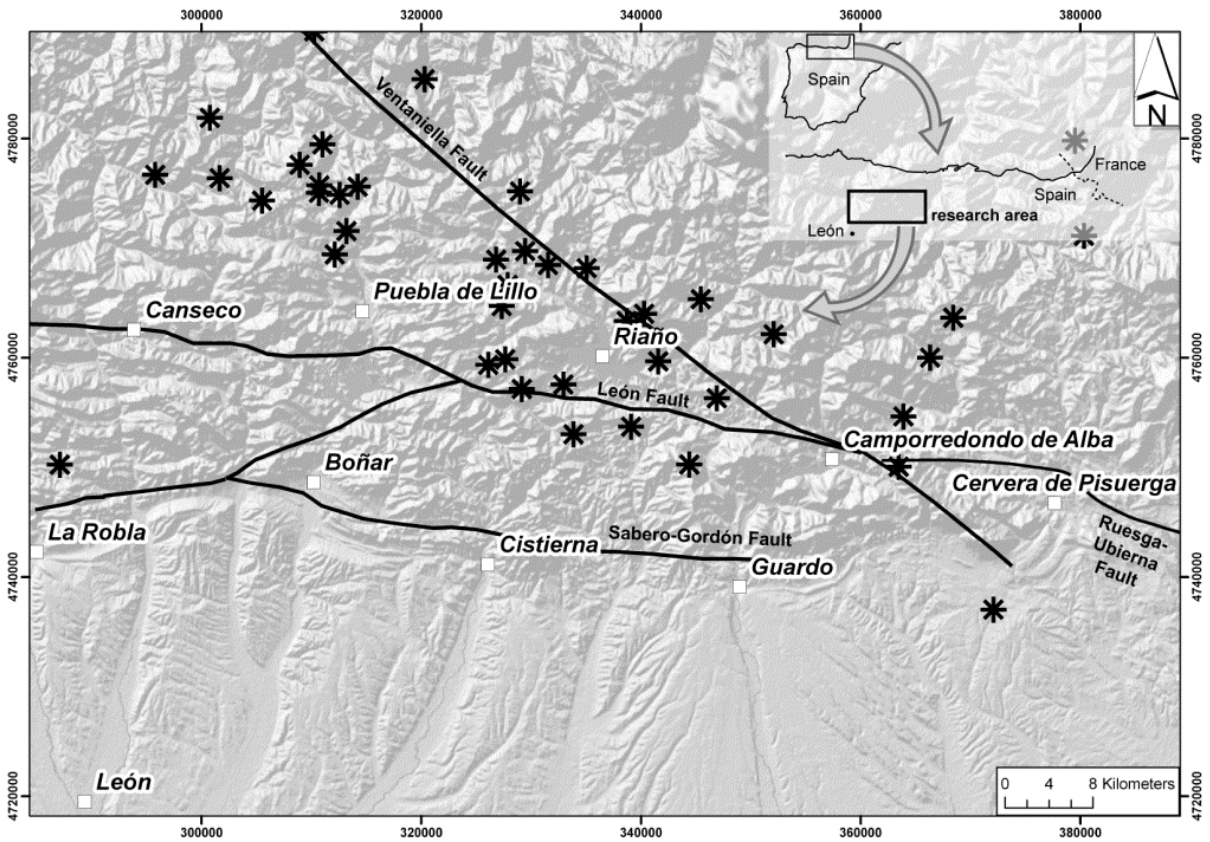

Fig. 4.4: Seismic activity (asterisks) recorded in the research area since 1960 (location of seismic events according to IGN, 2011).

4.2.1 Ventaniella Fault

The Ventaniella Fault (VF) stretches out by about 140 km in an NW–SE direction and separates the Cantabrian Mountains to the west from the Basque Mountains to the east (De Vicente et al., 2011) (Fig.3). With reference to the official geological maps of the region the VF cuts all previous structures including the Tertiary sedimentary succession (Arthaud and Matte, 1975; Julivert, 1971). The fault was first described by Julivert (1960) as a dextral decrochement fault (strike-slip fault) of late Hercynian (Permian) age, which has been reactivated several times (Julivert, 1971; Lepvrier and Martínez-García, 1990). Alonso et al. (2007) describe the VF as an Alpine fault whereas Aller et al. (2002) attribute the generation of the fault to the Mesozoic opening of the Bay of Biscay. Boillot (1986) ascribes the VF as initial normal fault that was generated during the continental rift phase prior to the rift in the Bay of Biscay. Malod and Mauffret (1990) and Olivet et al. (1984) interpret the VF and Ubierna Faults as strike-slip faults connecting pull apart basins during the following SE-motion of Iberia relative to Europe. The description of De Vicente et al. (2011) summarises the VF as ancient rift border fault, which was active during the Permian and Triassic extension and was subsequently reactivated during the Cenozoic compressive regime as right-lateral-strike-slip fault with a SW-verging reverse component (Marín et al., 1995). Additionally, Tavani et al. (2011) report active right lateral transpression in the Ventaniella-Ubierna Fault system. Along the fault seismic activity is continually reported (Alonso et al., 2007; López-Fernández et al., 2004, 2008) particularly northeast of Avilés and near Riaño (Fig. 4.4).

4.2.2 Sabero-Gordón Fault

The Sabero-Gordón Fault (SGF) extends in E-W direction, parallel to the Cantabrian Mountain margin (Fig. 4.1). The fault´s character and structural influence are still matters of discussion. The SGF was first mentioned by Evers (1967) as a facies boundary between thicker Devonian sediments in the north compared to the Devonian deposits in the south. Some authors characterise the SGF, including other major structural lines such as the Ventaniella-(Cardaño) and León Fault, as fractures generated in late Hercynian times with multiple reactivations (Heward and Reading, 1980). Alonso et al. (1996), Kullmann and Schönenberg (1978), Nijman and Savage (1989) and Reijers (1985) describe a horizontal displacement along the SGF, which is linked to the basin genesis in Stephanian times (Sabero Coal basin). During the Alpine Orogeny the main thrust of the Cantabrian Mountains on the Duero Basin caused the reactivation of the SGF as a backthrust rotated by simple shear (Alonso et al., 1996). According to these authors the geological sections show a steep vertical dip which varies slightly (Alonso et al., 1996; Reijers, 1985). The timing of reactivation or reactivations remains unclear, but the geological map of Boñar shows a displacement of Tertiary formations caused by movement on the SGF (Alonso et al., 1990). However, no seismic activity has recently been reported for the SGF.

4.2.3 León Fault

The León Fault strikes E–W about 100 km in the Cantabrian Zone (Fig. 4.1). The generation of the fault and reactivation phases are discussed controversially by Dutch and Spanish geologists (Alonso et al., 2009). De Sitter (1962), Evers 1967), Rupke (1965) and Sjerp (1967) described the fault as rupture zone, which influenced Devonian and Carboniferous sedimentation. Spanish authors characterise the fault as late Variscan strike-slip fault which was generated in Westphalian to Stephanian times with active phases in post-Stephanian times (see references in Alonso et al. (2009)). Kullmann and Schönenberg, (1978) and Heward and Reading (1980) interpret a dextral strike-slip fault which influenced the sedimentation during the Carboniferous (Alonso et al., 2009). Alonso et al. (2009) interpret the León Fault as out-of-sequence breaching thrust. According to these authors, movements along the breaching thrust occurred at the Moscovian-Stephanian boundary with minor reactivations of post-Stephanian age. The late Variscan phase of N–S shortening caused the subvertical dip of the fault.

4.3 Outline of the methods applied

The analysis of brittle tectonic structures is a common method to get information about regional stress regimes. The orientation and sense of slip of faults are indicators for the stress regime, which induced the generation and movements of the faults. There are two different approaches to the development of geological structures, which presume

1) stress as the independent variable acting on geological structures (Pollard and Saltzer, 1993), or

2) stress as the dependent material response to strain (Tikoff and Wojtal, 1999).

Accordingly, kinematic and dynamic analyses of field data have been a matter of debate in the scientific community. A detailed discussion of both approaches is given in Peacock and Marrett (2000) and Tikoff and Wojtal (1999). In practice both approaches are usually combined considering the strain which is accommodated by a structure and stress as the cause for the generation of the structure (Tikoff and Wojtal, 1999).

The kinematic analysis of faults and associated striae allows for a determination of the principal strain axes and for the deduction of the principal stress axes. In solids, stresses are characterised by anisotropic orientation and the state of stress is defined by three principal stress axes ($\sigma_1 > \sigma_2 > \sigma_3$) that define the stress ellipsoid (Angelier, 1994). Once the orientation of these principal axes is determined, the shape of the ellipsoid which is described by the stress ratio (R) = $(\sigma_2-\sigma_3)/(\sigma_1-\sigma_3)$ (Bott, 1959) can be calculated. The stress ratio (R) provides information about the magnitudes of the principal stress axes (Sperner et al., 1993) and varies between 0 and 1, where a value close to 1 indicates that $\sigma_2 = \sigma_1$, and (R) about 0 indicates $\sigma_2 = \sigma_3$. The ratio of the principal stress axes in relation to their orientations indicates the stress regime.

To deduce stress regimes from the strain of a body, assumptions have to be made dependent on the applied method. A general assumption is that the regional stress field is homogeneous in space and time (Pollard and Saltzer, 1993). The methods applied for palaeostress reconstructions are either based on the *Wallace and Bott criterion* (Bott, 1959; Wallace, 1951) or the *Mohr-Coulomb Criterion* (Van Gent et al., 2010).

The methodical principle founding on the *Wallace and Bott criterion* is that the fault slip direction can be predicted by knowing the orientation of a plane and the stress tensor. The inversion of this principle enables the deducibility of the stress tensor from fault-striae data (Van Gent et al., 2010). The basic assumption of the *Wallace and Bott criterion* is that fault slip occurs parallel to the maximum resolved shear stress on the plane. As a result, these methods yield the orientation of the principal stress axes.

The *Mohr-Coulomb criterion* assumes that the contraction and extension axes lie inside the plane defined by the slip direction and the normal of the fault plane. The ratio of shear stress and normal stress must be high for the generation of a fault. The results of the methods based on the *Mohr-Coulomb criterion* are the orientation of the kinematic axes (*p, b, t*) which in case of coaxial deformation correspond to the principal stress axes (Van Gent et al., 2010).

In summary, the analysis of brittle deformations provides information on the orientation of the stress axes and the shape of the stress ellipsoid. Gravity and earth`s free surface constrain one of the principal axis to be vertical and oblique oriented stress tensors mainly result from the rotation of former non-oblique faults. The kinematic analysis of faults is complicated by the existence of both neoformed faults and reactivated faults or weakness planes. Fault planes may show different slip generations, which are overlaying each other and may indicate local stress conditions instead of regional stress fields.

4.3.1 Data acquisition

In the research area 235 faults were identified at 38 sites and their orientations recorded as fault-striae data during the field program. The size of the fault planes ranged from cm- to m-scale. All data presented in this work and employed for analysis originate from fault planes and associated lineations on these fault planes.

The fault´s sense of slip can be determined by several criteria, first of all by the displacement of stratigraphic units. The slip senses of the faults treated in this work were identified *in situ* by the evaluation of slip indicators on the fault plane. In dependence of the lithology, mainly calcitic or quartzitic slickenfibres, as well as slickenside striations allowed for identification of the slip sense.

The incurrence of slickenfibres indicates aseismic creeping of the fault, as the slow growth of fibres is thought to have kept step with fault slip (Reuther, 2012) (Fig. 4.5).

Only unambiguous data are included in the analysis. The quality ranking for the type of data proposed by Sperner and Zweigel (2010) is disregarded in the present work. In the case of irregular fault plane surfaces, multiple data pairs were recorded to ensure the quality of the measured orientations.

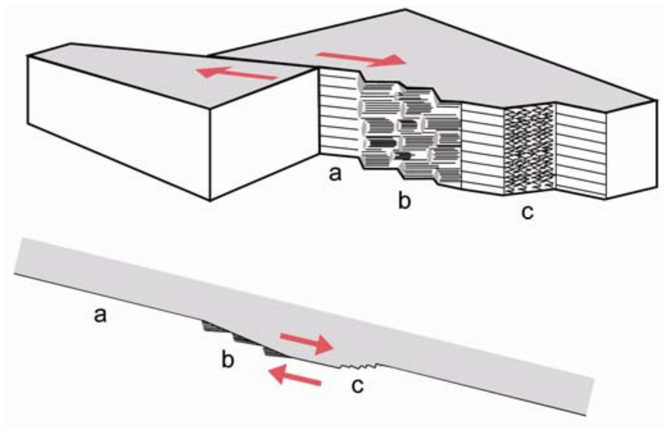

Fig. 4.5: Slip indicators on a strike-slip fault plane; a= striations (lineations); b= slickenfibres; c= horizontal slickolites (Reuther, 2012).

The locations of the sites were recorded by GPS and the faults were documented photographically and graphically. The dip direction and dip of the fault planes as well as the azimuth and plunge of the lineations were measured with a CLAR compass.

4.3.2 Processing

The data visualising, sorting and processing was performed with the program TectonicsFP (Ortner et al., 2002). After the input of raw data (orientations of fault planes and lineations as well as the fault´s character) the program offers a correction tool, which rotates the measured lineation on the associated fault plane to inhibit misfits. The corrected data form the base for further analysis. In the next step the heterogeneous data must be separated into homogeneous data sets. The sorting of inhomogeneous data is simplified by their visualisation into lower hemisphere plots, the Angelier diagram, Hoeppener diagram or the construction of *p-, b-* and *t*-axes after Turner (1953).

1) The Angelier diagram presents the fault planes as great circles and the lineations as poles, marked by arrows indicating the slip direction.

2) The Hoeppener diagram displays the poles to the fault planes with arrows indicating the slip direction of the fault (Hoeppener, 1955).

3) A further possibility to display the data is the analysis of pressure and tension axes (PT-method) according to Turner (1953). The PT- or PBT-method is based on the calculation of a theoretical contraction (*p*) and extension axis (*t*) for each fault-striae pair (Fig. 4.6). The maximum concentration

of *p*-axes corresponds to σ_1 and the *t*-axes correspond to the orientation of σ_3 (Sperner et al., 1993). Originally, the method was used in seismology but it is applicable in the brittle tectonic field, owing to the fact that the axes correspond to the infinitesimal strain axes of a fault. The method neglects natural anisotropy and assumes that faults in a data set were generated under homogeneous deformation; thus σ_2 lies in the fault plane and the angle of internal friction ϑ between the *p*-axis and the fault plane is constant (Ortner et al., 2002). A great circle is constructed through the pole to the fault plane and the lineation. This great circle is defined as movement plane and the *p*- and *t*-axis are located on this plane. For fractures generated according to the *Mohr Coulomb criterion*, typical values for the angle ϑ span about 30°. TectonicsFP offers the possibility to determine ϑ by a least-square-fit procedure or by manual input. The orientation of the *p*-axis at the determined angle is dependent on the fault´s character. The position of the *t*-axis is rotated by 90° from the *p*-axis on the movement plane and the angle between the *t*-axis and the pole of the fault plane is determined by the input angle. The *b*-axis or intermediate axis is oriented on the fault plane at an angle of 90° to the lineation.

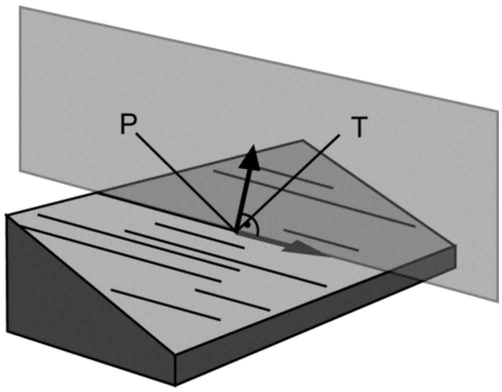

Fig. 4.6: Construction of pressure (*p*) and tension (*t*) axes for a given fault plane with striae (Meschede, 1994).

The *p-, b-* and *t*-axes are plotted in a lower hemisphere stereoplot and the maxima are counted statistically. Due to the simplified illustration of the data, the PT-plots are suitable for data separation and give a first indication of the orientation of the principal axes. The kinematic fault axes that were generated under a distinct stress regime are easily identified and hence can be assigned to the corresponding data set. The important step of sorting data can be carried out regarding different aspects. As homogeneous deformation is required for palaeostress analysis, faults in a homogeneous data set should fulfil this. Spatial grouping of data located in the same tectonic unit is possible. According to Sperner and Zweigel (2010) the separate analysis of each outcrop is reasonable and was applied in the present study.

4.3.3 Data analysis

The analysis procedure applied in the present work is summarised in Fig. 4.7. For each site, the *p*-and *t*-axes of the exposed faults were determined. According to the orientation of the kinematic axes, the data were grouped into homogeneous subsets (Fig. 4.7, step 1). These subsets were analysed with the different methods offered in TectonicsFP (*vide infra*).

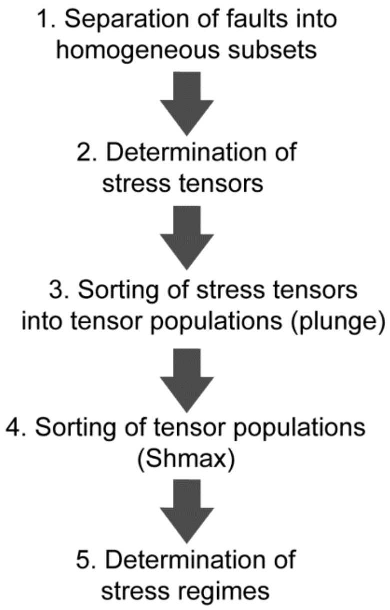

Fig. 4.7: Workflow of the analysis procedure. See reference in the text for steps 1 to 5.

Next, the resulting dynamic stress axes and kinematic axes, fluctuation diagrams, Mohr-circles and beachballs were plotted (Fig. 4.7, step 2) and the adequate method for stress axes calculation was chosen. Using this protocol, 54 stress tensors were determined. Tensor populations were grouped according to the steepness of the axes (Table 4.1) and the orientation of Shmax (Fig. 4.7, steps 3, 4). The fault-striae data generating the tensor populations were combined and the stress tensors of the populations were determined (Fig. 4.7, step 5). The stress axes calculation methods applied in this work are outlined in the following subsections.

Table 4.1: Tensor axes and grouping into tensor populations by means of the plunge of the axis.

Axis	Plunge	Population	Number of Tensors	Number of faults
p-axis	>45°	normal faults	11	36
b-axis	>45°	strike-slip faults	32	151
t-axis	>45°	reverse faults	11	48

4.3.4 Numerical dynamic analysis, NDA (Spang, 1972)

The NDA method was originally developed for the analysis of calcite twins. As twinning of calcite conforms to a slip along a fault, the NDA is applicable in fault-striae analysis (Sperner and Zweigel, 2010). The NDA method is based on the *Mohr-Coulomb criterion* and TectonicFP offers the possibility of a manual input of the angle ϑ which is about 30° for neoformed and 45° for reactivated faults (Van

Gent et al., 2010). The NDA determines the orientation of the *p-, b-* and *t*-axis for each dataset assuming a shear stress magnitude of 1 along the fault plane (Sperner and Zweigel, 2010). In the case of coaxial deformation, the kinematic axes and the calculated ratio (R) correspond to the principal stress axes and the stress ratio, respectively (Van Gent et al., 2010). The resulting tensors are summarised in the bulk tensor, which gives the orientations and relative values of the axes.

4.3.5 Inversion method

The orientation of the principal stress axis is based on the minimization of the lowest error squares (Angelier, 1994), which are the result of the angle of deviation of the lineation on a fault plane from the direction of the calculated maximum shear stress acting on this plane (Meschede, 1994). The reduced stress tensor is calculated from all data. The inversion method needs four independent faults with different orientations and different slip directions (Sperner and Zweigel, 2010) and fails either if one fault orientation is dominant or if conjugate faults are present (Van Gent et al., 2010). It may happen that the principle stress axis is oriented parallel to the fault plane, which does not provide the amount of shear stress necessary for slip initiation (Sperner and Zweigel, 2010).

4.3.6 Right dihedra method (Angelier and Mechler 1977)

Applying this method, a theoretical plane is constructed for each fault-striae pair perpendicular to the movement plane and the lineation, often referred to as “conjugate plane”. This conjugate plane and the fault plane divide the Schmidt projection into four quadrants, the “right dihedra” (Angelier and Mechler, 1977). Corresponding to the included axis, the quadrants are compressive or extensive. The Right Dihedra plots for each data pair are superimposed and from the area of the maximal probability of the position the σ_1 and σ_3 axes are determined. McKenzie (1969) showed that there can be significant differences between the *p*- and *t*-axes and the position of the principal stresses, for example when planes were reactivated. The maximum principal stress axis may be located everywhere in the compressive quadrant defined by the fault plane and the conjugate plane. The method of Angelier and Mechler (1977) assumes that the orientation defined by greatest number of *p*-quadrants corresponds with the σ_1 orientation.

4.4 Data presentation

A range of possibilities for presenting stress data on maps does exist and is widely accepted within the international research community. The most common ones are the “dihedra”- or “beachball” plots in combination with the construction of stress trajectories. The stress trajectories show the interpolation Shmax of the tensors, which is σ_1 in the case of reverse and strike-slip tensors and σ_2 in the case of normal tensors. In this work, the calculated tensor axes are presented in beachball plots. A beachball plot shows the compressive and distensive dihedra of the stress tensor

(Ortner et al., 2002) (Fig. 4.8). The advantage of this notation is that the orientation and plunge of all axes is easily recognised. In the following chapter, the positions of the principal axes are additionally indicated within the beachball plots.

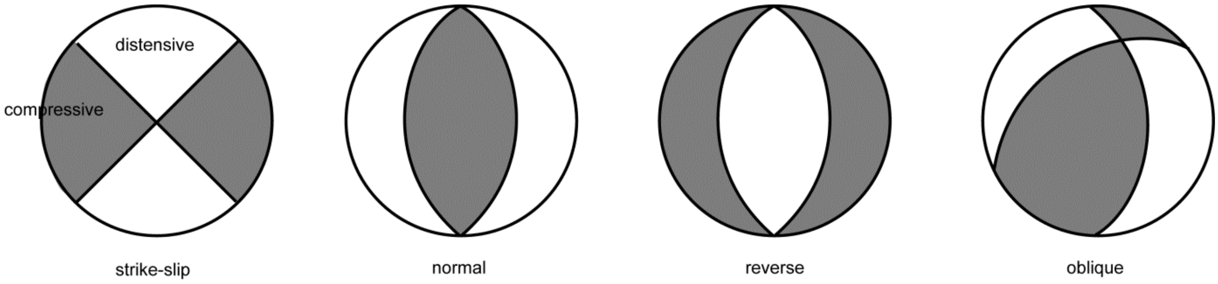

Fig. 4.8: Description of beachball plots; for the presentation of seismic data the compressive dihedra are white and the distensive dihedra black.

4.5 Results

The distribution of strike directions and dip angles of the 235 faults analysed in the present work is shown in Fig. 4.9a, b. The reduced stress tensors per outcrop were calculated with the NDA method and the Right Dihedra method. For each method fluctuation diagrams indicate the quality of the results, showing the angle between measured and theoretical slip direction. To find out the most adequate method for the data set, emphasis was put on an angle deviation < 30°. The resulting tensors are presented in Table 4.2. The results of this first approach are summarised in Fig. 4.10 and give an impression of the prevailing kinematic directions. Both strike-slip tensors and reverse tensors indicate predominantly N–S to NW–SE orientation of Shmax whereas the normal tensors show N–S distension (Fig. 4.10).

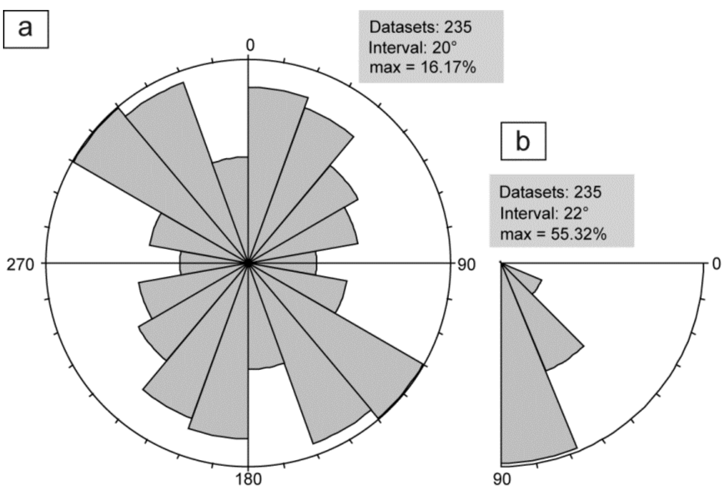

Fig. 4.9: (a) Rose diagram of the strike direction of fault planes analysed in this study; (b) Rose diagram of the dip of fault planes.

The 54 tensors of the outcrop analysis reveal a series of convergent solutions. Subsequent to the analysis of these preliminary results the tensor populations were grouped into homogeneous sets according to the Shmax direction (Fig. 4.7, step 4). Four Shmax directions oriented N–S, NW–SE, E–W and NE–SW resulted. The mean tensor for each palaeostress field was calculated in a second step by analysing the whole fault population related to the appropriate stress field together (Fig. 4.7, step 5). The resulting palaeostress patterns are described in the following subsections.

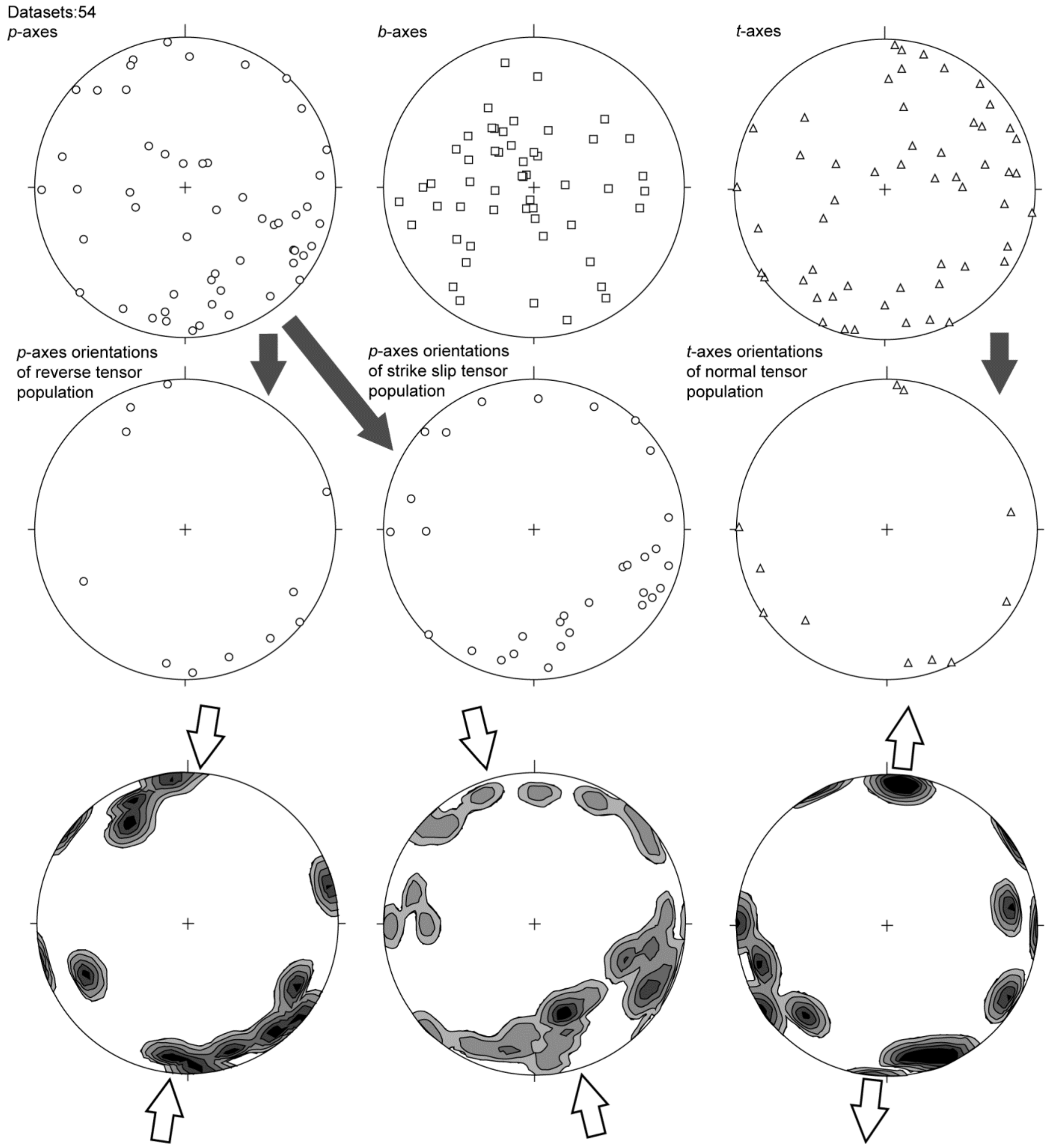

Fig. 4.10: Orientation of *p*-, *b*- and *t*- axes of the reduced tensors and the separation procedure into tensor populations (Fig.4.7, step 3, 4). Lowermost plots show the frequency distribution of the axes, white arrows highlight the dominant directions.

Table 4.2: Presentation of tensors calculated of homogeneous faults; nda = NDA method, dih= Right Dihedra method, *n*= number of faults, R = stress ratio, Shmax = maximum horizontal stress direction.

Name	UTM-coordinates		Age of lithological formation	Method	Theta angle (°)	*n*	*p*-axis (°)		*b*-axis (°)		*t*-axis (°)		R	Shmax (°)
Esl08	325954	4770387	Stephanian	nda	30	6	189	17	7	73	99	1	0.4929	9
Cusu06	304163	4754809	Namurian A	dih		2	174	8	329	82	83	13		174
Cur24	304103	4754260	Namurian B/C	nda	30	5	194	11	91	49	292	39	0.4932	14
Cur06	304056	4758733	Namurian B/C	nda	30	9	164	36	296	42	53	27	0.5033	164
Cur09	304000	4757871	Namurian A	dih		3	338	9	199	78	69	7		158
Ha	292752	4753099	Namurian A	nda	30	5	284	17	85	73	192	5	0.4978	284
Alm06b	291730	4757548	Ordovician	nda	30	5	85	11	332	64	180	24	0.4977	85
Alm07*	292497	4754470	m.Devonian	dih		2	355	77	213	11	121	8		33
Tosa06	305952	4760378	Namurian B/C	dih		2	43	72	253	16	161	9		73
Tosa01	305960	4760415	Namurian B/C	dih		3	353	3	84	28	258	62		173
Cusu07	304025	4754553	Namurian B/C	dih		2	104	25	331	55	206	22		104
Cur17	303472	4756179	Namurian A	dih		3	318	14	178	73	51	11		138
Vale04	387231	4735937	Palaeo-/Neogene	nda	30	5	269	5	169	63	2	27	0.5011	89
Cur20	303970	4755114	Namurian A	nda	30	5	143	39	326	51	234	1	0.4975	143
Cur22	303787	4755482	Quaternary	dih		2	115	8	315	82	205	3		115
PN04	313678	4759953	Stephanian	dih		2	125	13	14	58	222	29		125
UT23	311856	4758620	Namurian B/C	nda	30	5	37	74	264	11	171	11	0.4848	84
Cs29*	314949	4760433	Kambrian	dih		2	178	63	2	27	271	2		2
Pn01	313789	4759893	Kambrian	dih		3	142	9	46	35	245	53		142
Vss15	387063	4735839	Palaeo-/Neogene	nda	30	7	167	21	51	48	171	34	0.4887	167
Cs13	314578	4760551	Namurian B/C	nda	30	7	161	28	293	51	57	24	0.4980	161
Rn10	332198	4765788	Stephanian	nda	30	4	186	29	308	44	76	32	0.5016	6
Cur10	303984	4757908	Namurian A	dih		2	113	36	255	48	8	20		113
M1.3*	313057	4745328	Stephanian	nda	30	7	112	44	330	39	222	20	0.5033	150
Fs1_1	313983	4744973	Stephanian	nda	30	4	269	29	143	38	143	38	0.4925	89
Fs1_2*	313983	4744973	Stephanian	nda	30	4	329	69	146	21	236	1	0.4919	146
Fs2b	313889	4744957	Stephanian	nda	30	4	120	10	0	71	212	16	0.5358	120
Fs2a j	313889	4744957	Stephanian	nda	30	4	177	5	270	27	77	62	0.4896	177
Fs2a ä	313889	4744957	Stephanian	nda	30	4	329	25	222	33	88	47	0.5028	149
M1.6_1	313273	475210	Stephanian	nda	30	4	312	3	197	83	42	6	0.5037	132
M1.6_2	313273	475210	Stephanian	dih		2	111	34	275	55	16	7		111
M1.4	313075	4745269	Stephanian	nda	30	4	161	39	325	50	64	8	0.4998	161
M1.5_1	313364	4745179	Stephanian	nda	30	4	26	10	182	79	295	4	0.5071	26
M1.5_2	313364	4745179	Stephanian	nda	30	4	161	39	325	50	64	8	0.4998	161
fs3*	314811	4745147	Stephanian	dih		3	243	25	147	13	32	62		63
fs6	310868	4746112	Visean	nda	30	4	207	10	338	75	115	11	0.5010	27
Cs22_2	314302	4760313	Stephanian	dih		3	75	3	166	10	330	79		75
Cs22_1*	314302	4760313	Stephanian	nda	30	5	126	69	347	16	253	13	0.5173	167
Cs22_3*	314302	4760313	Stephanian	dih		2	248	61	63	29	154	2		63
Torio1_1	292492	4754499	m.Devonian	nda	35	5	161	11	259	35	57	53	0.4892	161
Torio1_2_1	292492	4754499	m.Devonian	nda	40	9	129	2	219	16	33	74	0.5147	129
Torio1_2_2	292492	4754499	m.Devonian	nda	40	5	120	18	227	42	13	43	0.5024	120
Cur04_1	304039	4758700	Quaternary	dih		2	265	60	101	29	7	7		101
Cur04_2	304039	4758700	Quaternary	nda	30	8	2	14	241	65	97	21	0.5080	2
Cur21_2	303775	4755496	Namurian A	dih		2	105	8	313	81	196	4		105
Cur21_1	303775	4755496	Namurian A	nda	30	10	43	1	135	61	312	29	0.5021	43
Cur07_1*	304171	4758329	Namurian A	dih		2	319	60	180	24	82	18		180
Cur07_2	304171	4758329	Namurian A	nda	30	4	225	0	315	63	134	27	0.4912	45
Ld02_1	377896	4742535	u.Cretaceous	dih		2	100	58	272	32	4	4		92
Ld02_2	377896	4742535	u.Cretaceous	nda	30	11	120	17	265	69	26	11	0.4956	120
Cusu8_1-1	304188	4754497	Namurian B/C	dih		2	99	19	343	52	201	32		99
Cusu8_1	304188	4754497	Namurian B/C	nda	40	9	56	7	313	61	150	28	0.4979	56
Cusu8_2	304188	4754497	Namurian B/C	nda	30	5	336	12	236	38	80	50	0.5166	156
Cusu8_3	304188	4754497	Namurian B/C	nda	30	4	188	11	92	27	298	60	0.5017	8

*= faults incompatible with palaeostress fields

4.5.1 *Stress regimes*

E–W maximum horizontal stress

The location of the faults and fault types assigned to the E–W stress pattern are shown in Fig. 4.11. Analysis of all faults of the E–W Shmax pattern yields a stress ratio (R) of 0.7275, which indicates a transtensional stress regime according to Meschede (1994). The stress field can be identified at 13 sites and 18% of the whole fault population is explained by the E–W-transtensional regime. The faults are distributed in the western and eastern part of the research area. The E–W stress pattern is related to strike-slip and normal faults, which is supported by the stress ratio (R) (Fig. 4.11a, b). Dextral faults strike in NE–SW direction and sinistral faults are NW–SE oriented (Fig. 4.12, Vale04). Normal faults occurring in the research area strike widely E–W.

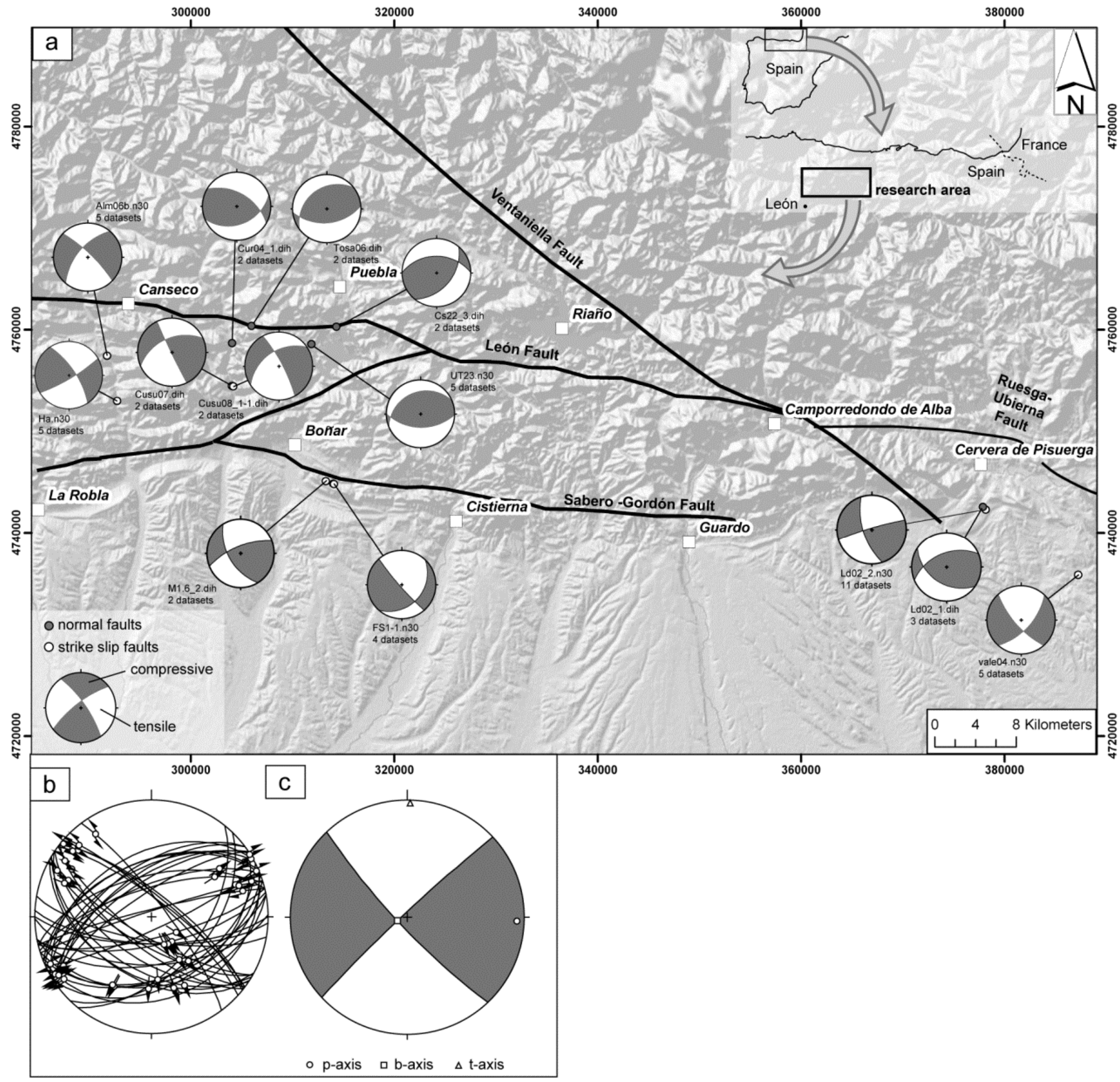

Fig. 4.11: (a) Beachball representation of stress axes orientation, white dots = strike-slip faults, grey dots = normal faults; the abbreviation "n30" stands for calculations with NDA method with ϑ = 30°, "dih" stands for application of Right Dihedra method; (b) Angelier plot of the faults assigned to the E–W stress regime; (c) stress axes orientation (analysis of all data).

Faults belonging to this regime affect rocks of Ordovician to Palaeo-Neogene ages. By applying the NDA method, the mean tensor for this stress field was calculated, with an orientation of the principal stress axis of σ_1= 088/12, σ_2=265/76 and σ_3= 002/02, i.e. σ_1 and σ_3 are nearly horizontal (Fig. 4.11c). Examples of the faults belonging to the E–W stress field are represented in Fig. 4.12.

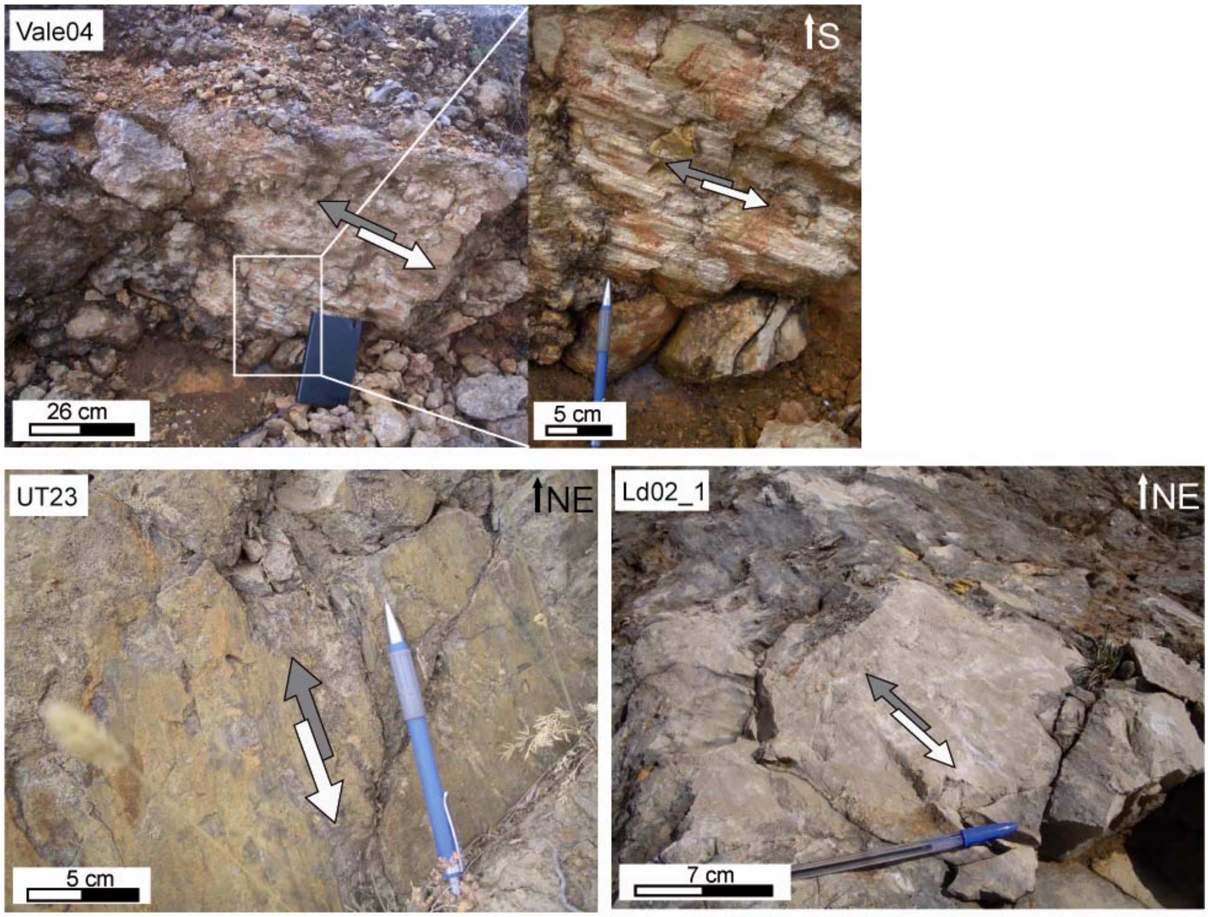

Fig. 4.12: Vale04: sinistral strike-slip fault as indicated by slickenside striations and steps in Palaeogene conglomerate rocks; UT23: normal fault in sandstones of the Westphalian Lena Formation; Ld02_1: oblique normal fault in upper Cretaceous limestones.

N–S maximum horizontal stress

The N–S stress regime comprises 65 faults at 13 different sites and constitutes one of the dominant stress patterns in the research area. The faults are dominantly strike-slip faults except for 4 sites where reverse faulting has been identified (Fig. 4.13a, b). The stress axes orientations and locations of the faults are shown in Fig. 4.13. The analysis of all faults results in a stress ratio (R) = 0.2196, which is characteristic for transpressional stress regimes (Meschede, 1994). Particularly sinistral strike-slip faults striking NE–SW (Fig. 4.14, Esl08) and dextral strike-slip faults striking NW–SE are present. The application of the NDA method gives a mean tensor with the following orientation: σ_1= 174/18, σ_2= 311/66 and σ_3= 079/15 (Fig. 4.13c). Further examples of faults assigned to the N–S stress pattern are shown in Fig. 4.14. The rocks affected by faults assigned to this pattern range from Devonian to Quaternary ages.

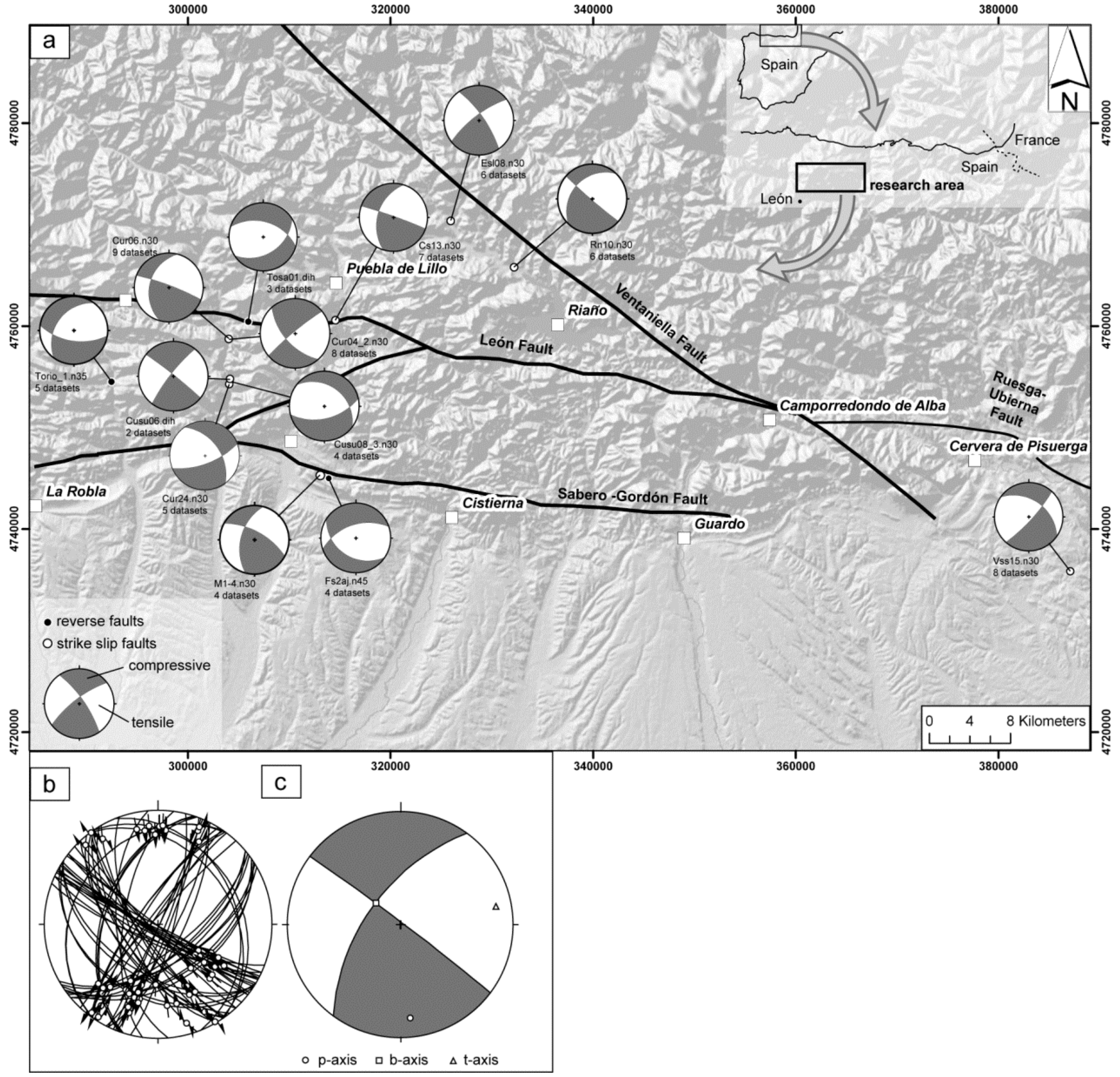

Fig. 4.13: (a) Beachball representation of stress axes orientation, white dots = strike-slip faults, black dots = reverse faults; the abbreviation "n30" stands for calculations with NDA method with ϑ = 30°, "dih" stands for application of Right Dihedra method; (b) Angelier plot of the faults assigned to the N–S stress regime; (c) stress axes orientation (analysis of all data).

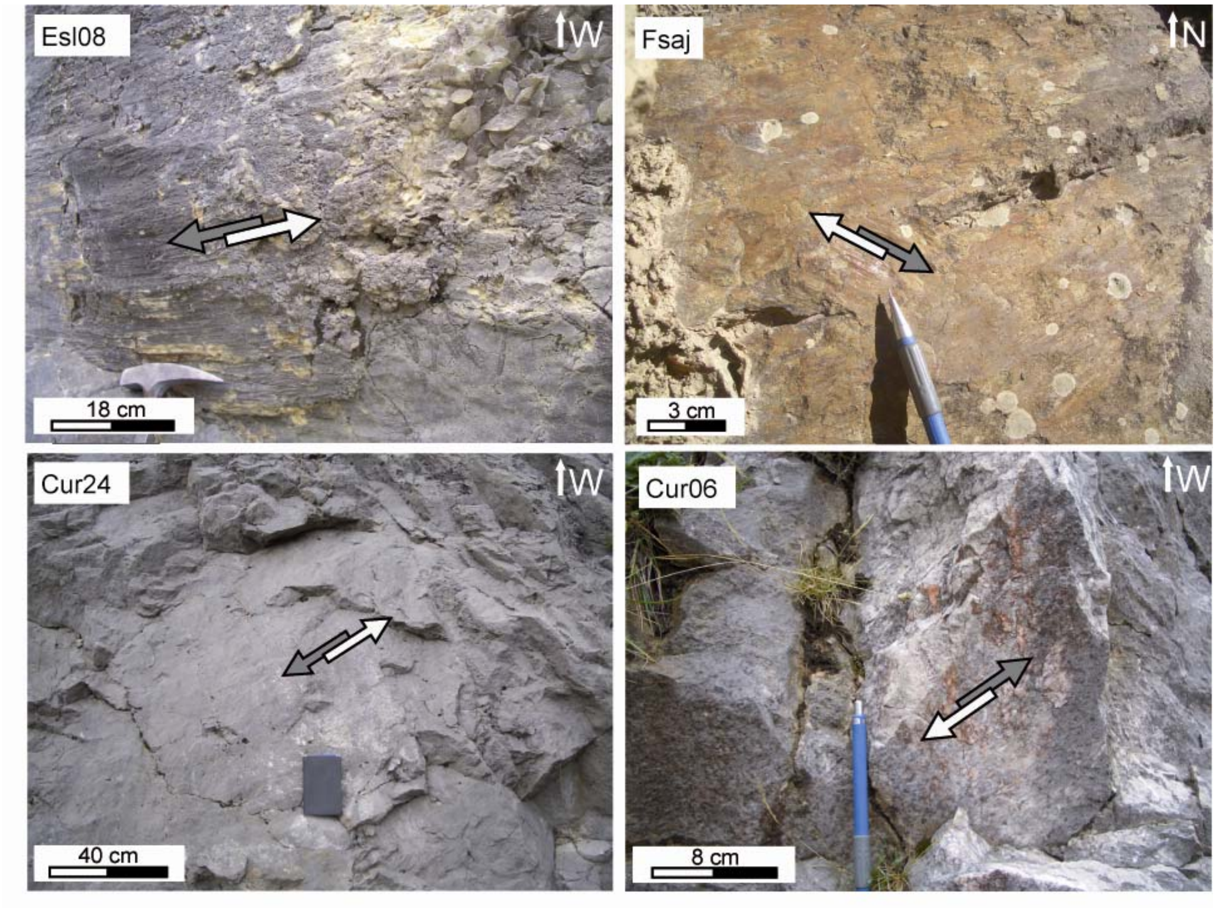

Fig. 4.14: Esl08: sinistral strike-slip fault, as indicated by slickenfibres in olistolith limestone of Stephanian age; Fsaj: younger generation of slickenside striations indicates oblique reverse faulting in molasse sediments of Stephanian age; Cur24: sinistral oblique strike-slip faulting (Namurian/Westphalian limestones); Cur06: dextral oblique strike-slip faulting in Namurian/Westphalian limestones (Valdeteja Formation).

NW–SE maximum horizontal stress

The palaeostress field with NW–SE oriented Shmax is the second dominant field in the research area. 27% of the whole faults analysed can be assigned to this stress field, occurring at 37% of the measurement sites (Fig. 4.16a). It is composed of two tensor populations, which are related to strike-slip faulting and reverse faulting (Fig. 4.16a, b). The faults deform rocks ranging from Cambrian to Quaternary ages. The stress ratio (R) of 0.3373 points to a transpressional regime (Meschede, 1994). The mean tensor for this stress pattern is shown in Fig. 16c and is composed of the axes σ_1= 135/01, σ_2=230/70 and σ_3= 045/18. Fig. 4.16, “Cur22” shows a typical sinistral, N–S striking strike-slip fault, assigned to the NW–SE stress pattern. The dextral strike-slip faults strike in E–W direction (Fig. 4.15b; Fig. 4.16, Fsaä).

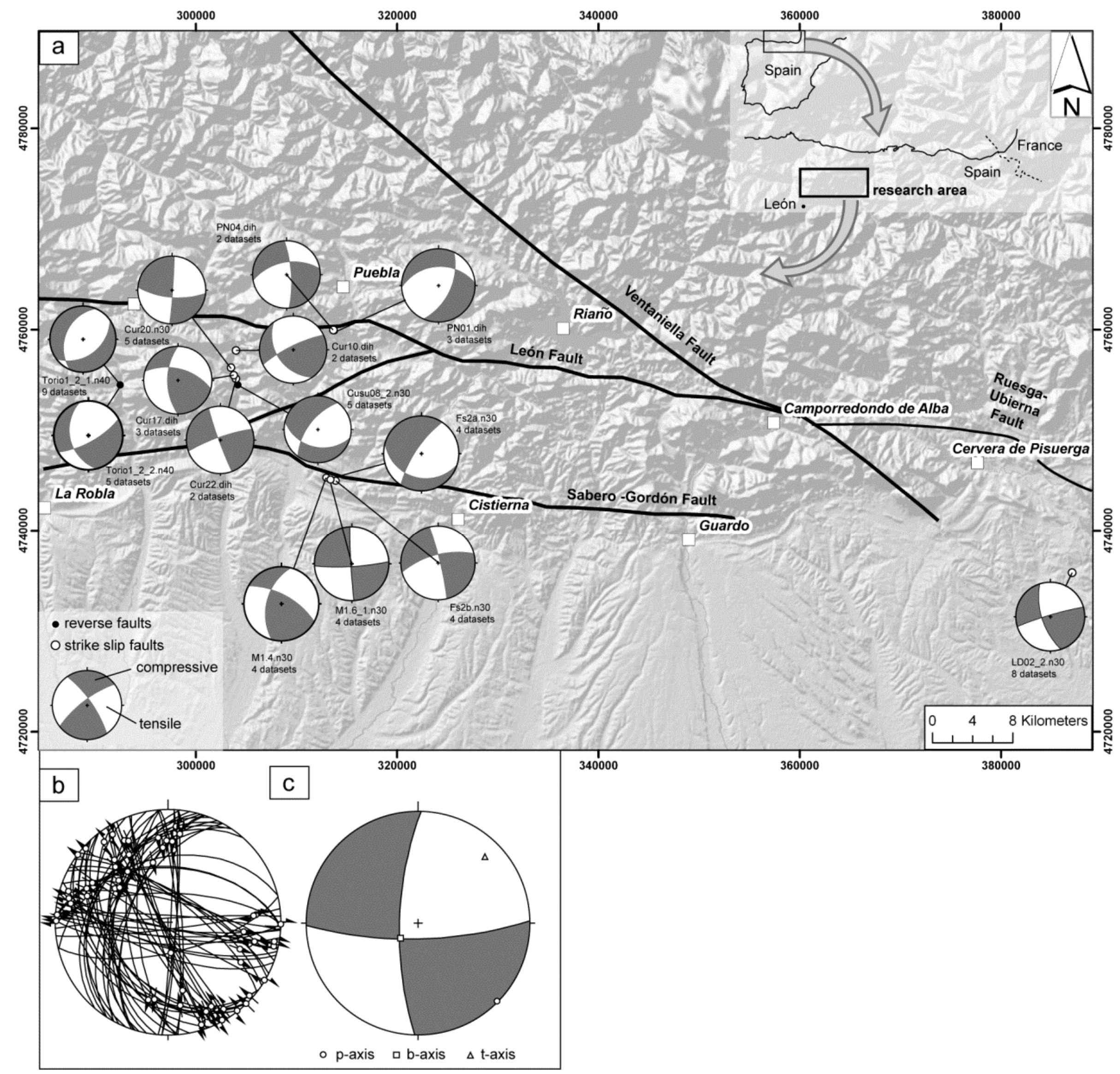

Fig. 4.15: (a) Beachball representation of stress axes orientation, white dots = strike-slip faults, black dots= reverse faults; the abbreviation “n30” stands for calculations with NDA method with ϑ = 30°, “dih” stands for application of Right Dihedra method; (b) Angelier plot of the faults assigned to the NW–SE stress regime; (c) stress axes orientation (analysis of all data).

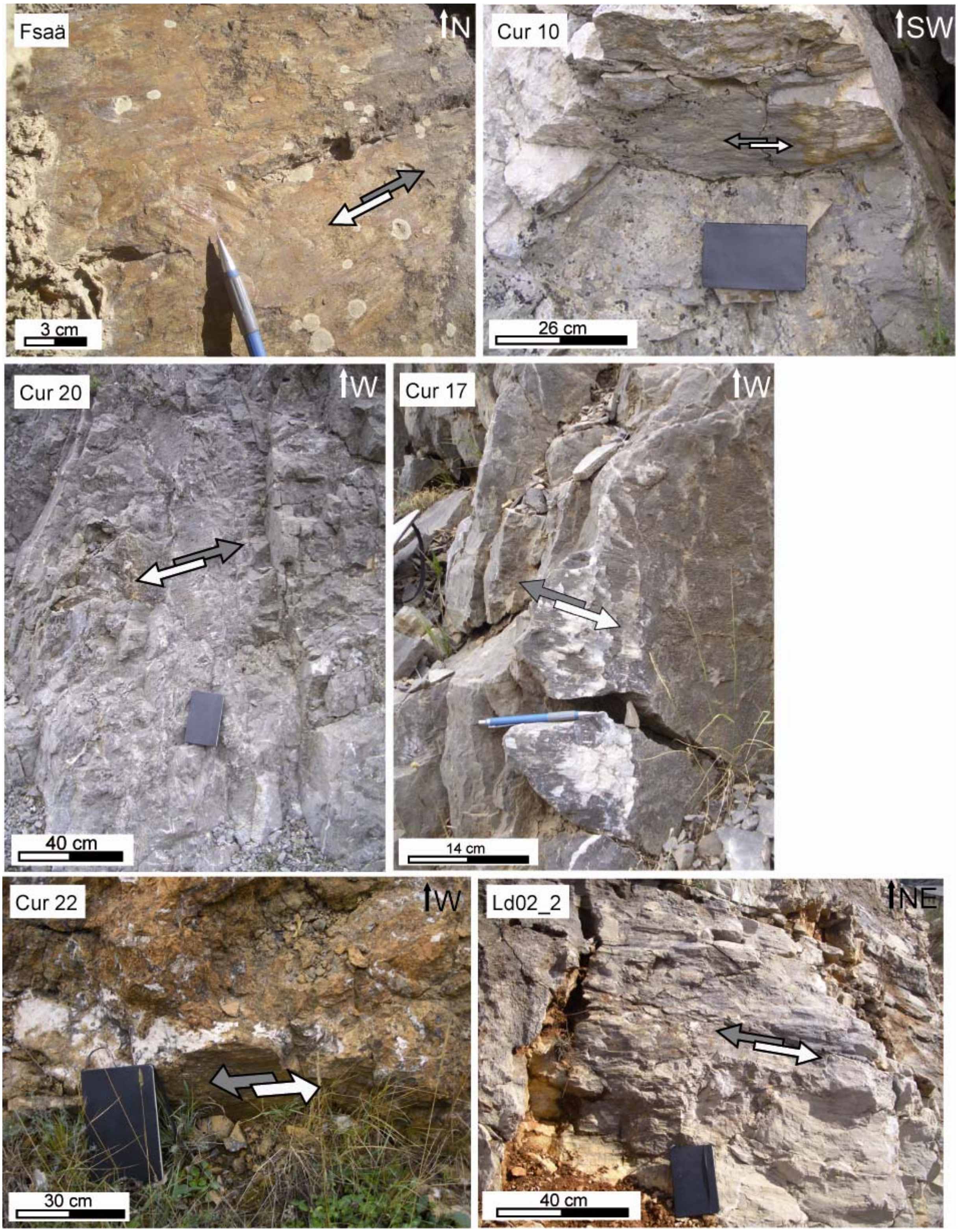

Fig. 4.16: Fsaä: dextral strike-slip fault in molasse sediments of Stephanian age; Cur10: sinistral strike-slip faulting in Namurian/Westphalian limestones (Valdeteja Formation); Cur20: dextral strike-slip fault in Namurian/Westphalian limestones (Valdeteja Formation); Cur17: sinistral strike-slip fault in Namurian/Westphalian limestones (Valdeteja Formation); Cur22: sinistral strike-slip faulting in consolidated Quaternary debris; Ld02_2: sinistral strike-slip fault in upper Cretaceous limestones.

NE–SW maximum horizontal stress

The stress pattern with NE–SW oriented Shmax represents 13% of the faults analysed in the present work. These faults appear at 5 sites in the research area and concentrate in the Curueño valley and along the SGF (Fig. 4.17a). The rocks affected by these faults are of Carboniferous ages. The NE–SW oriented Shmax led to the formation of N–S to NE–SW strike-slip faults (Fig. 4.17a, b). The mean tensor calculated for the stress pattern is σ_1= 037/02, σ_2=286/85 and σ_3= 127/05 (Fig. 4.17c). The stress ratio (R) = 0.3782 indicates a strike-slip regime with a minor reverse component. Fig. 4.18 represents three dextral strike-slip faults assigned to the NE–SW stress pattern that are striking in N–S direction.

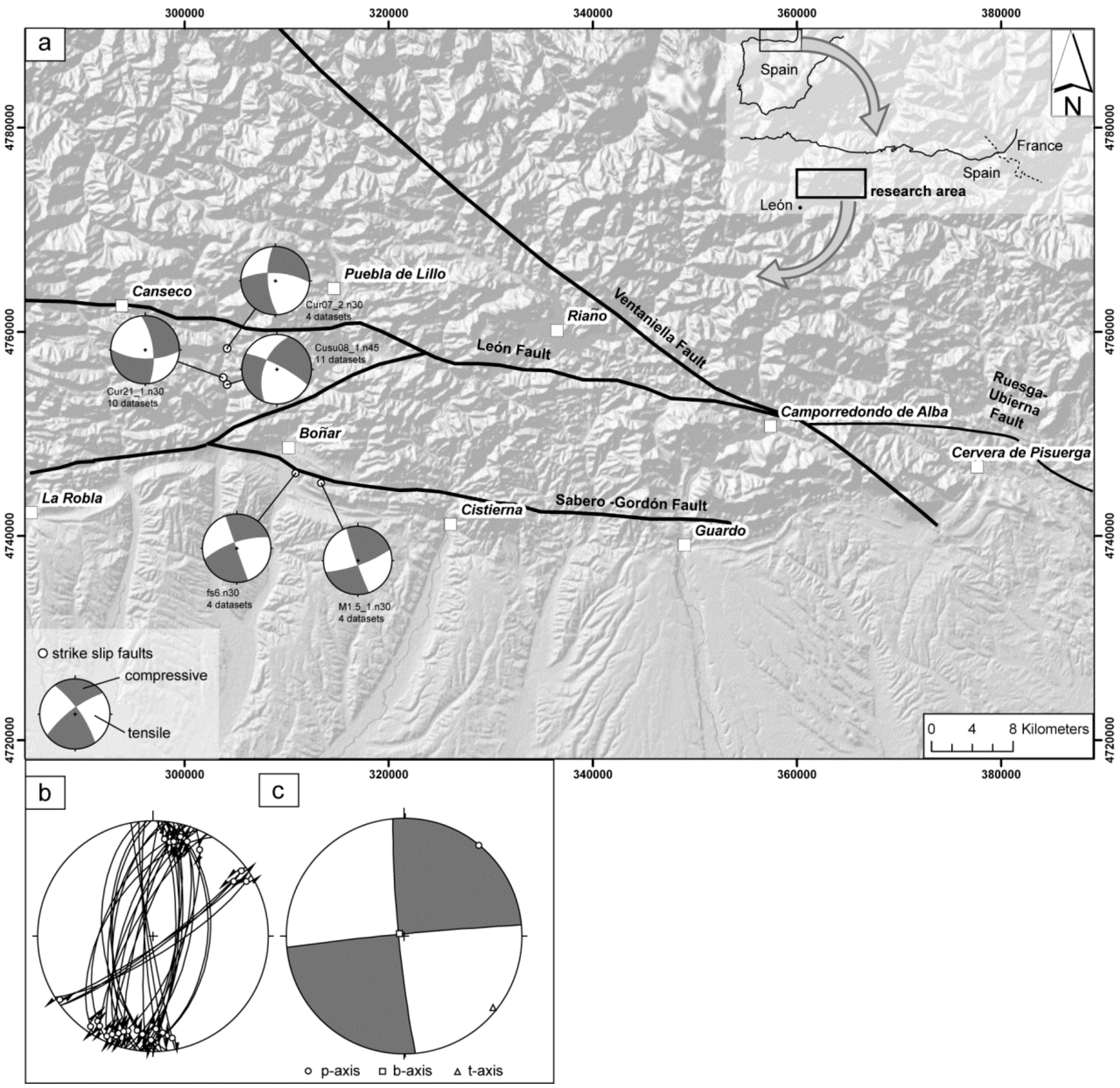

Fig. 4.17: (a) Beachball representation of stress axes orientation, the abbreviation “n30” stands for calculations with NDA method with ϑ = 30°, “dih” stands for application of Right Dihedra method; (b) Angelier plot of the faults assigned to the NE–SW stress regime; (c) stress axes orientation (analysis of all data).

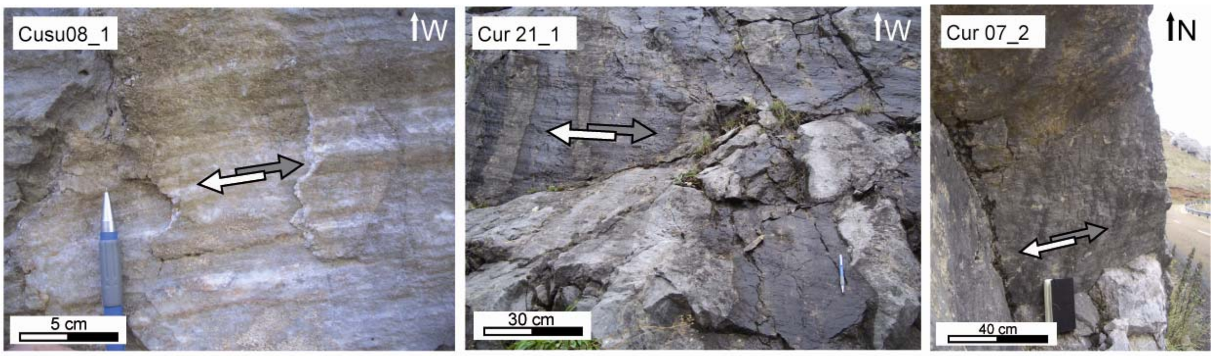

Fig. 4.18: Cusu08_1: dextral strike-slip fault, as indicated by slickenside striations and steps in Namurian/Westphalian limestones (Valdeteja Formation); Cur21_1: dextral strike-slip fault (Valdeteja Formation); Cur07_2: dextral strike-slip fault, fault´s character indicated by slickenfibres (Valdeteja Formation).

Incompatible faults:

28 faults are not compatible with the resulting stress fields. The tensors of these faults are marked in Table 4.2 and can be summarised to a normal fault population with Shmax = NW–SE and a reverse population with Shmax = E–W.

4.6 Discussion

As stated above, the results of fault-striae analysis are four palaeostress patterns with Shmax oriented E–W, NE–SW, NW–SE and N–S shown in Fig. 4.11, 13, 15, 17; Table 4.3.

Table 4.3: Statistical distribution of the faults assigned to a palaeostress pattern.

	Faults	%	Sites	%
E–W	43	18.30	13	34.21
N–S	65	27.66	13	34.21
NE–SW	31	13.19	5	13.16
NW–SE	64	27.23	14	36.84
Residual faults	32	13.62	7	18.42

These orientations correspond to the stress directions published by De Vicente et al. (2005) as main stress orientations for the Iberian Peninsula. Additionally, the quantitative distribution of the Shmax patterns in the research area is shown in Table 4.3. Crosscutting relationships such as superposition of striae on a single fault plane are scarce in the research area; thus, the chronological order of the palaeostress patterns is limited to relative estimations. To assign a relative age to a palaeostress field, indirect indicators such as the age of the affected rocks must be included. Fig. 4.19 shows a summary of the principal compression directions reported by several authors related to the research area. N–S to NNW–SSE to NNE–SSW compression is evident since Palaeogene/Neogene times. The data collected in this work fits well with the so far known directions, but the exact assignment to a geological period is not possible. Nevertheless, a relative assignment is being made and the results are shown in Fig. 4.19 (outer right column).

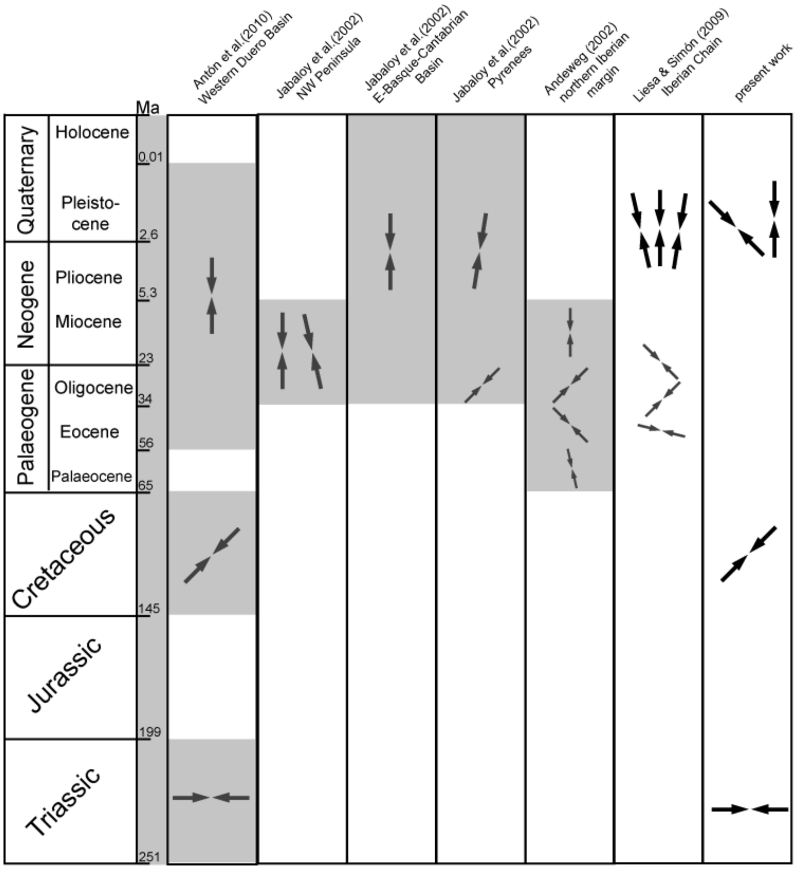

Fig. 4.19: Mesozoic to recent palaeostress directions, compiled according to Andeweg (2002); Antón et al. (2010); Jabaloy et al. (2002) and Liesa and Simón (2009).

In order to find out the recent stress states in the research area, the faults affecting the youngest rocks are of special interest. The faults present in the youngest lithologies are shown in Table 4.4. 74% of these can be assigned to the NW–SE and N–S stress field whereas the transtensive E–W palaeostress field generated 26% of these recent faults.

Table 4.4: Faults affecting youngest rocks deposited in the research area.

Site	Faults	Age	Palaeostress-field
Cur22	2	Quaternary	NW–SE
Cur04_1	2	Quaternary	E–W
Cur04_2	8	Quaternary	N–S
Vss15	7	Palaeo-Neogene	N–S
Vale04	5	Palaeo-Neogene	E–W
LD02_1	3	late Cretaceous	E–W
LD02_2	11	late Cretaceous	NW–SE

An E–W transtensional stress field is reported by Antón et al. (2010), who investigated an area between the Vilariça strike-slip belt and the western margin of the Duero basin. Absolute dating revealed that the E–W palaeostress pattern can be assigned to Triassic times. In the present work, this E–W oriented palaeostress pattern affected late Cretaceous to Quaternary rocks. The supposed Quaternary "Cur04_1"- and "LD02_1"-faults occur together with faults assigned to the N–S and NW–SE stress field (Table 4.4). Due to the lack of evidence for an E–W transtensional stress regime in Cenozoic times, these faults must be discussed separately. Fig. 4.20 shows that under a mean stress state local stress deviations may occur at the transition from one structure to another.

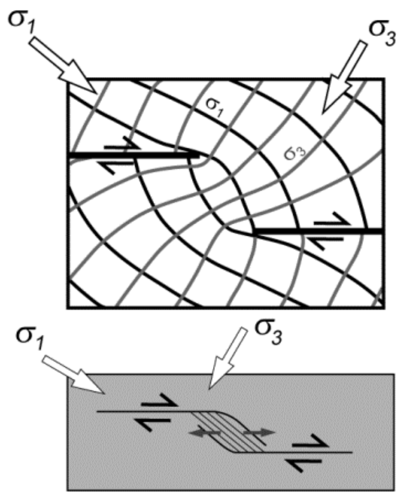

Fig. 4.20: Stress state and local stress deviation due to the interplay of two geological structures (modified after Chinnery, 1966).

The faults that generate the "Cur04_1" tensor are normal faults striking 70° whereas the main part of faults identified at site "Cur04" are dextral strike-slip faults that strike about 140°. The dextral strike-slip faults indicate an orientation of the principal stress axis of NNE–SSW and belong to the N–S palaeostress pattern. It is probable that the normal faults detected at the "Cur04" site are secondary structures related to the movement on the dominating dextral strike-slip faults. Such conditions would be met in the transition zone between two equal oriented dextral strike-slip faults. Accordingly these faults may have been generated as secondary structures to principal faults, thus indicating a misleading stress orientation. A simple sketch shows that local stress deviations can account for the "Cur04_1" faults (Fig. 4.21).

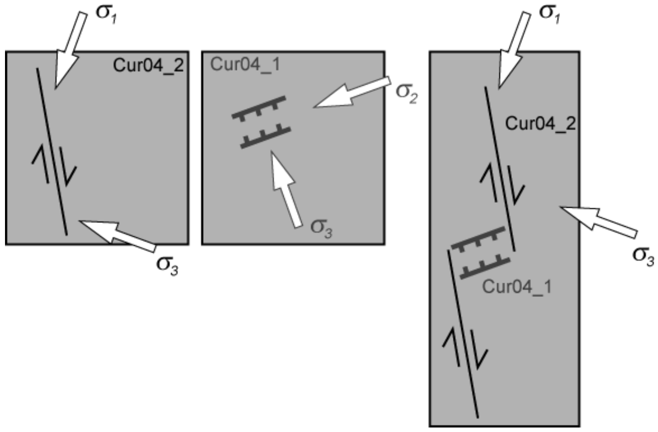

Fig. 4.21: Explanation of the generation of "Cur04_1"-faults under a NNE–SSW stress regime.

In the case of the “Cur04” site, this assumption is supported by the quantitative distribution of the faults (Table 4.4). The same holds true for the “Ld02_1”- and “Ld02_2”-faults (Fig. 4.22). The dominant faults occurring at the “Ld02” site are strike-slip faults that are assigned to the NW–SE palaeostress pattern. A permutation of the principal stress axes due to the interplay of faults thus may be accountable for these faults and demonstrates the ambiguousness that bears the interpretation of fault-striae data and the importance of controlling the calculated principal axes.

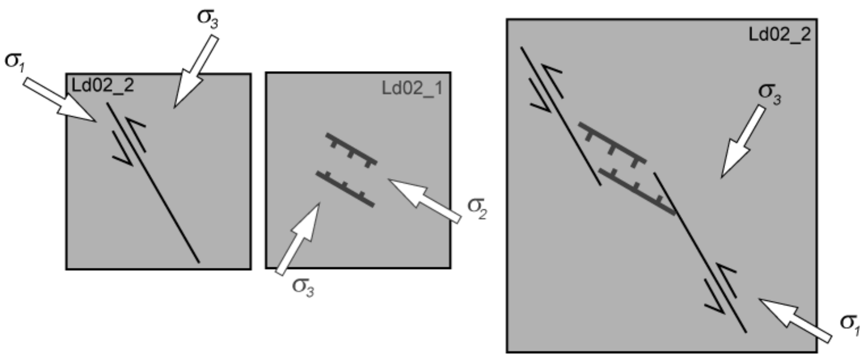

Fig. 4.22: Explanation of the generation of “LD02_1” faults under a NW–SE stress regime.

The faults at the “Vale04” site are NW–SE striking sinistral strike-slip faults. Adjacent to the “Vale04” site N–S striking oblique reverse faults are present (“Vss15”site, Fig. 4.13a), deforming the same rocks but indicating a different orientation of the principal stress axis (N–S to NNW–SSE horizontal σ_1). The generation of the “Vale04” faults under such σ_1-orientation would be possible as tear fault, displacing two reverse faults. Moreover, both sites are located beneath the Ventaniella Fault and the existence of structures as transpressive strike-slip duplexes should be taken into consideration. Strike-slip duplexes may arise from tensional or compressional bends under progressing shear and provide the conditions for complex fault interplay (Fig. 4.23a, b).

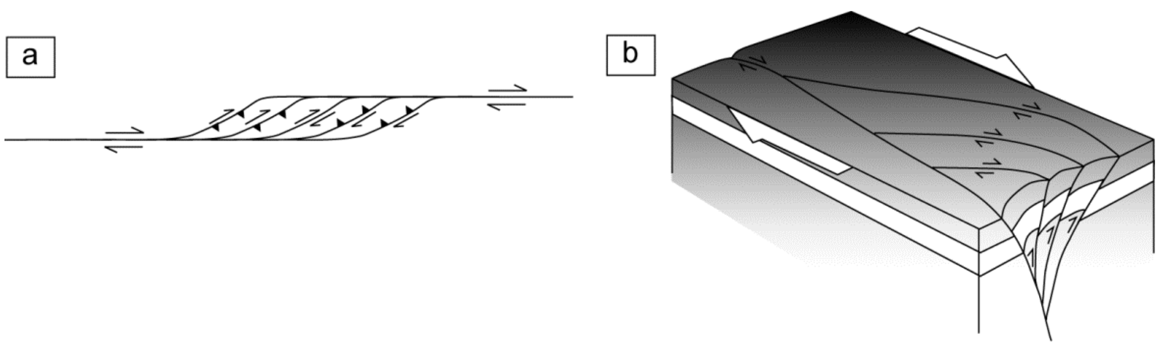

Fig. 4.23: (a) Aerial view of transpressional strike-slip duplex between two dextral strike slip faults (Reuther, 2012); (b) 3D view showing part of a transpressional strike-slip duplex, modified after Woodcock and Fischer (1986).

The most recent lithologies affected by the NE–SW palaeostress pattern were deposited in Stephanian times and no younger rocks have been observed to be deformed by faults of this regime. As the pre-Mesozoic deformations are unlikely to be preserved, the NE–SW pattern may be assigned to Cretaceous times as reported by Antón et al. (2010) (Fig. 4.19). The NE–SW stress field is a strike-slip regime with nearly horizontal σ_1 and σ_3 values. The remaining palaeostress patterns are the N–S and NW–SE patterns. Both have influenced the majority of faults analysed in the present work and are quantitative equally present in the research area (Table 4.3). Including the "Cur04_1"- and "Ld02_1" faults (which could subsequently be assigned to the N–S and NW–SE stress pattern) does not significantly change the quantitative distribution between these dominant stress patterns. Cloetingh et al. (2002) report N to NE compression due to the Pyrenean compression but a NE–SW recent stress pattern was not detected in the research area. Superposition of striae on a fault plane (Fig. 4.14, Fsaj; Fig. 4.16, Fsaä) indicates the N–S stress field as the younger one, but must be handled with care, as multiple slickenside striations on a fault plane could in principle also be attributed to the interaction of faults. The N–S stress pattern as the youngest one disagrees with the overall actual stress field reported for Iberia with NW–SE orientation described in Chapter 4.1. Recent measurements of electromagnetic radiation emitted from rocks under current stress in the research area indicate present-day Shmax trending between 130–140° (Berger, 2011; Jäger, 2011).

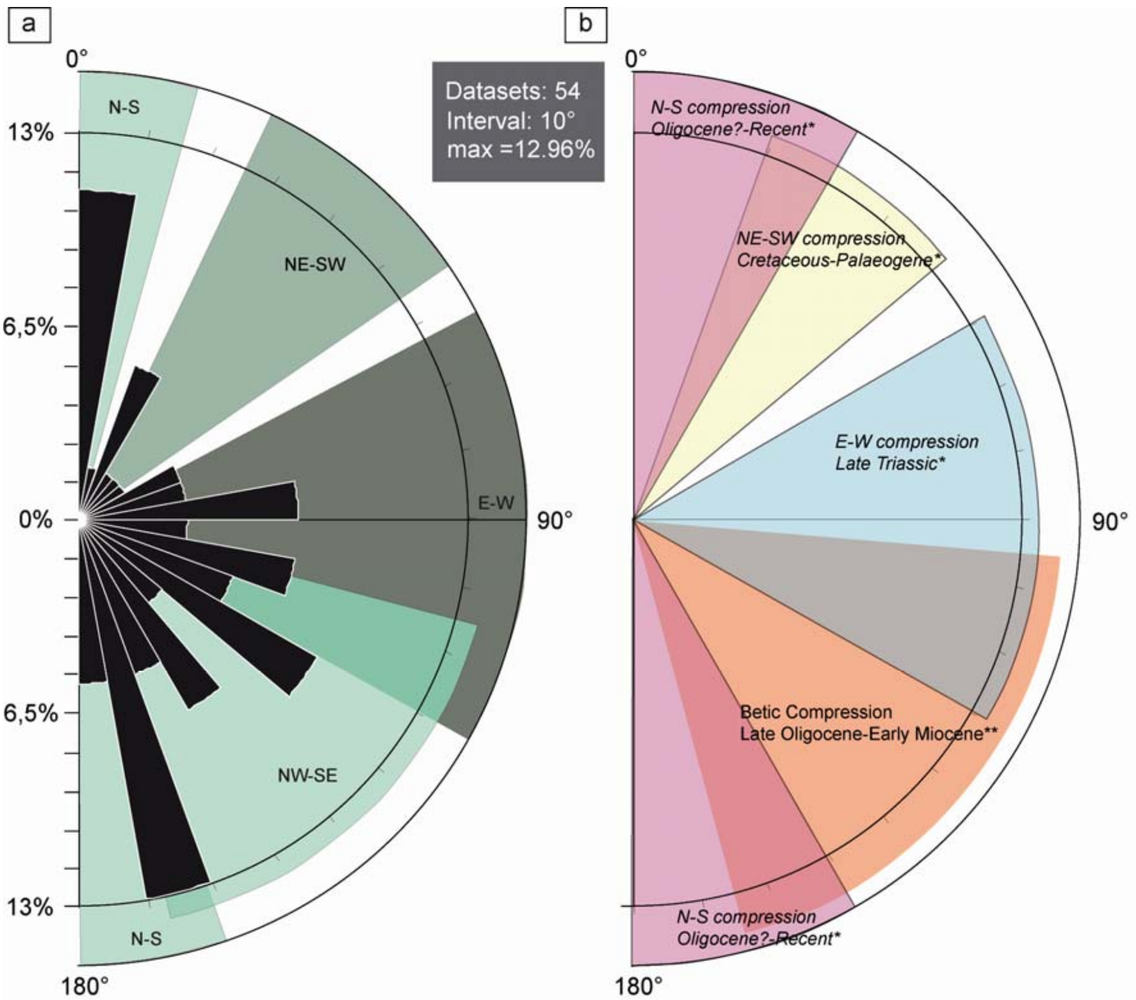

Fig. 4.24: (a) Results of the stress inversion, local Shmax compression trends are displayed as rose diagram for the research area; (b) Interpretation of the results of Antón et al. (2010)(*)and Liesa and Simón (2009)(**).

Nevertheless, the palaeostress analysis of Antón et al. (2010) resulted in an N–S oriented palaeostress pattern as the most recent one, prevailing from Oligocene to Miocene times. The most recent palaeostress pattern (NW–SE) could not be detected in the research are of Antón et al. (2010). The authors explain this with the indication of De Vicente and Vegas (2009) who stated that NW–SE compression induced by the Betics has not yet superimposed western Iberia.

Based on the data analysed in the present study, a determination of the chronology of the N–S and NW–SE palaeostress pattern is not possible because the faults belonging to these patterns occur at the same sites and affect the same rocks. Nevertheless, the data analysed indicate that these stress patterns are the most recent ones affecting the research area. Fig. 4.24a shows a rose diagram of the local maximum compression directions (Shmax) of the analysed data and the corresponding events according to Antón et al. (2010) (west of the research area) and Liesa and Simón (2009) (Fig. 4.24b) (south east of the research area). The overlap of the Shmax solutions of the N–S and NW–SE is displayed and the similar stress ratio (Chapter 4.4.1) implies a possible relation between these patterns. The comparison with the results of the present work indicates a good agreement with the events inducing the stresses responsible for the faults to the west of the research area and part of the results of the Iberian Chain.

At the northern margin of the Iberian Peninsula, the influence of the N–S Pyrenean compression played an important role. The concurrent dominant NW–SE compression corresponds to the present-day stress state reported for the Iberian Peninsula, but the effects on the southern Cantabrian Mountains were not investigated so far. As reported by some authors, the transmission of this compression to the western part of Iberia is uncertain (e.g. Antón et al., 2010; De Vicente and Vegas, 2009). The faults detected in the vicinity of the SGF are represented in all stress patterns determined in this work. Depending on the orientation of the maximum horizontal stress axis, activity phases of the SGF as reverse fault (N–S compression) or dextral strike-slip fault (NW–SE compression) are possible. Both Shmax directions would enable active movement on the SGF, which is supported by the elevated ^{222}Rn in soil gas concentrations reported by Künze et al. (2012).

4.7 Conclusions

A quantitative approach is applied in order to display the dominant stress directions recorded by faults in rocks of Cambrian to Quaternary age. Based on the faults affecting the youngest rocks present in the research area, a relative estimation of the chronology of the resulting palaeostress patterns was undertaken. The forthcoming maximum horizontal compression directions indicate four palaeostress patterns, oriented N–S, NE–SW, E–W and NW–SE. As crosscutting relationships in the research area are scarce, the timeframe of the stress patterns was derived with respect to the age of the rocks affected and the stress inducing events reported in literature. The E–W Shmax pattern is related to strike-slip and normal faults. In the literature this stress field is dated to the late Triassic. The following stress pattern is the NE–SW transpressive stress field, responsible for strike-slip and reverse faults in Carboniferous rocks. The youngest stress patterns are the N–S and the NW–SE oriented ones, which are the dominant stress patterns resulting from the inversion of fault-striae data analysed in this work. Between these patterns, a clear chronological separation cannot be attempted on basis of the available data. Due to several overprintings of deformations during the stress history of the Cantabrian Mountains, palaeostress analysis of faults that predominantly occur in Palaeozoic rocks is complicated. Absolute dating methods of mineral fibres that developed on fault planes would provide further insight into the chronological order of the dominant stress directions recorded in the research area.

5 Soil gas ^{222}Rn concentration in northern Germany and its relationship with geological subsurface structures

Submitted to Journal of Environmental Radioactivity

Abstract

^{222}Rn in soil gas activity was measured across the margins of two active salt diapirs in Schleswig-Holstein, northern Germany, in order to reveal the impact of halokinetic processes on the soil gas signal. Soil gas- and soil sampling were carried out in springtime and summer 2011. The occurrence of elevated ^{222}Rn in soil gas concentrations in Schleswig-Holstein has been ascribed to radionuclide rich moraine boulder material deposits, but the contribution of subsurface structures has not been investigated so far. Reference samples were taken from a region known for its granitic moraine boulder deposits, resulting in ^{222}Rn in soil gas activity of 40 kBq/m^3. The values resulting from profile sampling across salt dome margins are of the order of twice the moraine boulder material reference values and exceed 100 kBq/m^3. The zones of elevated concentrations are consistent throughout time though variations in magnitudes. One soil gas profile recorded in this work expands parallel to a seismic profile and reveals multiple zones of elevated ^{222}Rn activities above a rising salt intrusion. The physical and chemical properties of salt have an impact on the processes influencing gas migration and surface near radionuclide accumulations. The rise of salt supports the breakup of rock components thus leading to enhanced emanation. This work provides a first approach regarding the halokinetic contribution to the ^{222}Rn in soil gas occurrence and a possible theoretical model which summarises the relevant processes was developed.

5.1 Introduction

The investigation of the ^{222}Rn activity in soil gas in Germany progressed with the development of a national Rn map which was published 1998 by the University of Bonn (Kemski et al., 1999). The ^{222}Rn in soil gas measurements and their evaluation were carried out by the Geological Institute of the University of Bonn considering the geological formations and structural circumstances and are published in Kemski et al. (1996b, 2001, 2002, 2004, 2009) and Lehmann et al. (2001). Both factors influence the geogenic ^{222}Rn potential which has a fundamental impact on the indoor ^{222}Rn activity. Today, mapping of ^{222}Rn in soil gas and indoor ^{222}Rn is common practice internationally as the inhalation of ^{222}Rn and its progenies provoke lung cancer (Appleton and Miles, 2010; Dubois et al., 2010; Ielsch et al., 2010). In 1990, the European Commission recommended an indoor reference level of 400 Bq/m^3 (annual Rn gas concentration) for existing buildings, which is the equivalent to an effective dose of 20 mSv per year. For new constructions, an average annual gas concentration of 200 Bq/m^3 is the aim (Ripa di Meana, 1990).

Yet an annual exposure to 150 Bq/m^3 results in a significant additional lung cancer risk. The World Health Organisation (WHO) advocates a reference level of 100 Bq/m^3 (WHO, 2009). A similar approach is advised by the International Commission on Radiological Protection (ICRP, 2009) recommending for an annual dose of 10 mSv from Rn, as well as the Strahlenschutzkommission (SSK, 2004) with a reference level of 150 Bq/m^3 annual indoor ^{222}Rn exposure.

In this paper we deal with the application of ^{222}Rn in soil gas measurements in the tectonic field, which has not been investigated in detail in northern Germany so far. Apart from quantifying the health risk ^{222}Rn in soil gas measurements are subjects of interest for tectonic researchers, as active faults reveal elevated ^{222}Rn in soil gas signals. The measurement of ^{222}Rn in soil gas is frequently applied in further fields of geosciences as economic geology (Singh et al., 1986) and prediction of seismic (e.g. King, 1986) and volcanologic hazards (e.g. Baubron, 1991) as the short half life of 3.82 days enables ^{222}Rn as a natural tracer. The elevated ^{222}Rn activity in soil gas above fault zones and areas of high permeability has been reported all over the world. ^{222}Rn in soil gas measurements are a well accepted method for the mapping of active fault zones nowadays. Even the detection of latent fault movements with the ^{222}Rn method yielded conclusive results (González-Díez et al., 2009).

Our research areas are located in Schleswig-Holstein, northern Germany. Northern Germany is characterised by unconsolidated Quaternary deposits and is generally known as seismically rather inactive area. The flat morphology draws the attention to the subsurface, characterised by Permian salt structures which rose up thousands of meters in the ground. These halokinetic processes are proceeding until today. Yet, the appliance of ^{222}Rn in soil gas measurements in northern Germany is limited to the measurements which attributed to the national Rn map (Kemski et al., 1996b, 1999). In this paper we report the ^{222}Rn activity values in soil gas across two active salt structures. According to previous investigations of Kemski et al. (1996b, 1999), Schleswig-Holstein is characterised by ^{222}Rn in soil gas concentrations about 10–50 kBq/m^3 in the western part and higher activities in the eastern part with local concentrations > 100 kBq/m^3. The authors attribute the east-west gradient in the ^{222}Rn in soil gas activity to the distribution of glacial sediments. In the eastern part of Schleswig-Holstein, the granite rich glacial deposits of the Weichsel glacier are dominant.

Neither the impact of geological subsurface structures on the local ^{222}Rn in soil gas signal in northern Germany nor the general behaviour of ^{222}Rn above salt structures has been investigated so far. Salt structures near the surface form geothermal zones (Jensen, 1983; Nagihara et al., 1992) and have an impact on groundwater salinity (Magri et al., 2009). The rise of salt domes provokes faults in the overlying geological strata. All these aspects influence the gas characteristics and migration possibilities in the soil. Our measurement program was carried out during springtime and summer 2011. The aims of this work are (1) to determine ^{222}Rn activity in soil gas above salt structures in Schleswig-Holstein and (2) to develop a possible theoretical model which can explain elevated ^{222}Rn concentrations in the soil gas of the investigated areas.

5.2 Geological background

The investigated area in Schleswig-Holstein forms part of the North German Basin (NGB), which is located in the central part of the Central European Basin System (CEBS). The CEBS extends from the North Sea to Poland and from Norway to middle Germany (Maystrenko et al., 2008). Structurally, the CEBS is confined by two NW-SE striking deep seated fault zones, the Sorgenfrei-Tornquist Zone (STZ) and the Elbe Fault Zone (EFZ) to the south (Scheck-Wenderoth and Lamarche, 2005), as shown in Fig. 5.1. The formation of the CEBS was initiated at the end of the Variscan Orogeny during the late Carboniferous and early Permian. The incipient basin evolution was supported by early Permian volcanism, further broadening due to the E–W extensional stress field (Ziegler, 1982) and the beginning of regional thermal subsidence (Bachmann et al., 2008; Breitkreuz et al., 2008). Three basins developed, the Northern- and Southern Permian Basin (NPB, SPB), which were separated by the Ringköbing Fyn High, and the Polish Trough (Maystrenko et al., 2008). The CEBS coincides with the position of the former SPB. During the lower Permian (Rotliegend), mainly reddish continental siliciclastics were deposited under arid climate conditions. The earliest salt deposits were lacustrine evaporites in the central part of the SPB (Bachmann et al., 2008). The transgressional events in the upper Permian (Zechstein) flooded both basins. Eustatic sea level changes as well as isostatic subsidence of exposed swells caused the alternating connection of the Permian basins with the northern boreal ocean and subordinate with the Tethys to the south; thus both effects are responsible for the cyclic deposition of the Zechstein evaporites. According to Ziegler (1982) the thickness of the Zechstein salt layers in the SPB reached up to some 1500 m. The basin evolution proceeded under thermal subsidence during the Zechstein transgression (Scheck-Wenderoth et al., 2008). The E–W extensional stress regime continued during the early Triassic leading to the widening of the basin areas (Scheck-Wenderoth et al., 2008). During the Buntsandstein, mainly siliciclastic sediments were deposited, which changed with the marine Muschelkalk deposits. At the beginning of the Muschelkalk, syndepositional normal faults caused the formation of graben structures and troughs, striking in N–S direction, e.g. the Glückstadt Graben (GG), Central Graben and Horn Graben (Fig. 5.1).

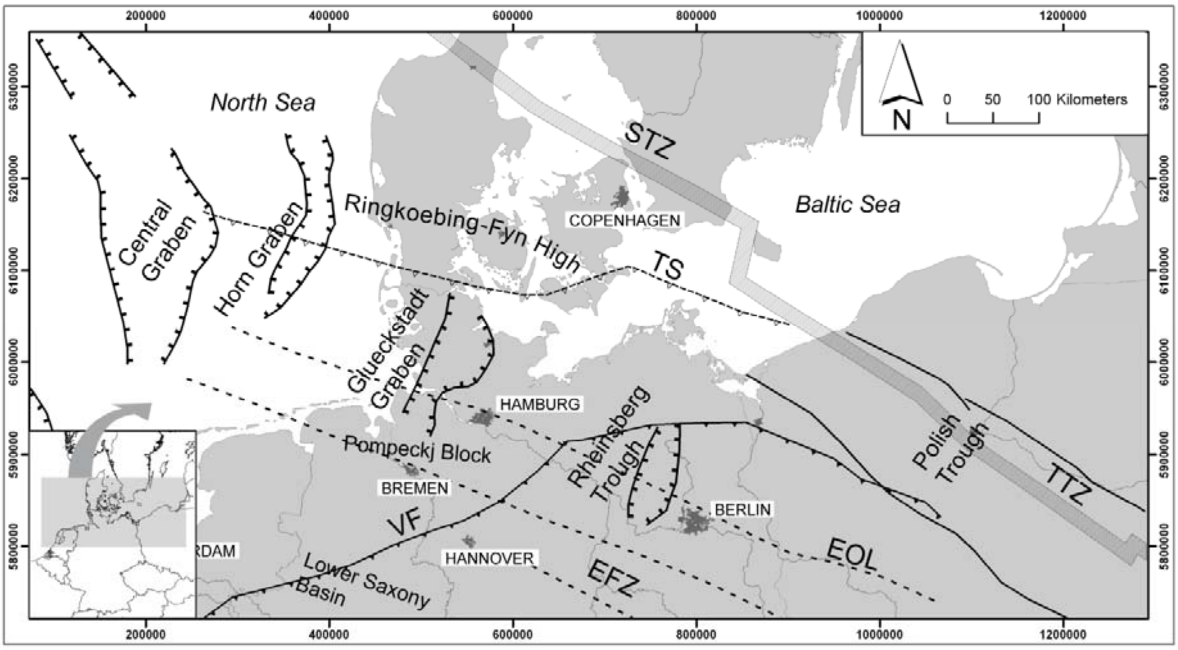

Fig. 5.1: Structural outline of the CEBS modified after Maystrenko et al. (2005a, 2010). STZ= Sorgenfrei-Tornquist Zone, TS= Thor Suture, TTZ= Teisseyre-Tornquist Zone, EOL= Elbe-Odra Line, EFZ= Elbe Fault System, VF= Variscan Front.

Due to the development of these structures, the former WNW–ESE striking Permian basins were differentiated in a series of sub-basins (Scheck-Wenderoth et al., 2008). During the Keuper, renewed siliciclastic sediments with intercalated evaporites dominated. The early Triassic E–W extension reached its maximum in the Keuper, leading to a stage of rapid subsidence which is recorded in the GG (Maystrenko et al., 2008). The late Triassic is further characterised by the development of river systems as documented by fluvial deposits. During the Jurassic, the Westholstein Trough, Hamburg Trough and Eastholstein Trough (Fig. 5.2) developed in the marginal zones of the GG (Scheck-Wenderoth et al., 2008). The deposits during this time are mainly marine carbonates. The marine conditions persisted during the Jurassic and Cretaceous era. In the late Cretaceous a fundamental change in the regional tectonic regime affected the CEBS: NE–SW compression was induced by the Alpine Orogeny. Permo-triassic normal faults were reactivated as reverse faults and induced the basin inversion of the CEBS. The compressional regime proceeded during the early and middle Tertiary until the Pleistocene, when the North German Basin turned into a continental phase. Mainly limnic and fluvial deposits prevail, deformed by glacial activity and overlain by the deposits of the Quaternary glaciers. The Weichsel glaciation is the youngest one; it occurred from 20,000 until 12,000 years ago and brought granite rich material from Scandinavia and the Baltic Sea. Regarding the salt structures in the CEBS, two groups can be characterised, a first group with structures striking in NW–SE direction, following the TTZ, STZ and the EFS. These structures developed over basement faults that were initiated prior to salt deposition. The second group of salt structures is N–S oriented and traces the graben structures in the central part of the CEBS (Scheck-Wenderoth et al., 2008).

5.2.1 *Evolution of the Glückstadt Graben (GG) and salt movements therein*

The investigated salt structures are located in the GG-realm. The development of the GG was investigated by Baykulov et al. (2009), Maystrenko et al. (2005a, 2005b, 2010), Scheck-Wenderoth et al. (2008), Yegorova et al. (2008) and Yoon et al. (2008). The GG strikes in NE direction about 180 km and is confined by the Rinkoebing-Fyn High in the North and the Lower Saxony Basin in the South (Fig. 5.1). Structurally, the GG can be divided in a central Triassic graben and marginal troughs generated later, which build up the transition to the adjacent blocks (Fig. 5.2a). The research area is located at the eastern border of the Eastholstein Trough, which adjoins the Eastholstein-Mecklenburg Block (Fig. 5.2a). The GG accommodates up to 12,000 m thick Permian to Cenozoic sediments (Scheck-Wenderoth et al., 2008) and the evolution of the GG is strongly characterised by the interaction of regional tectonics and salt tectonics.

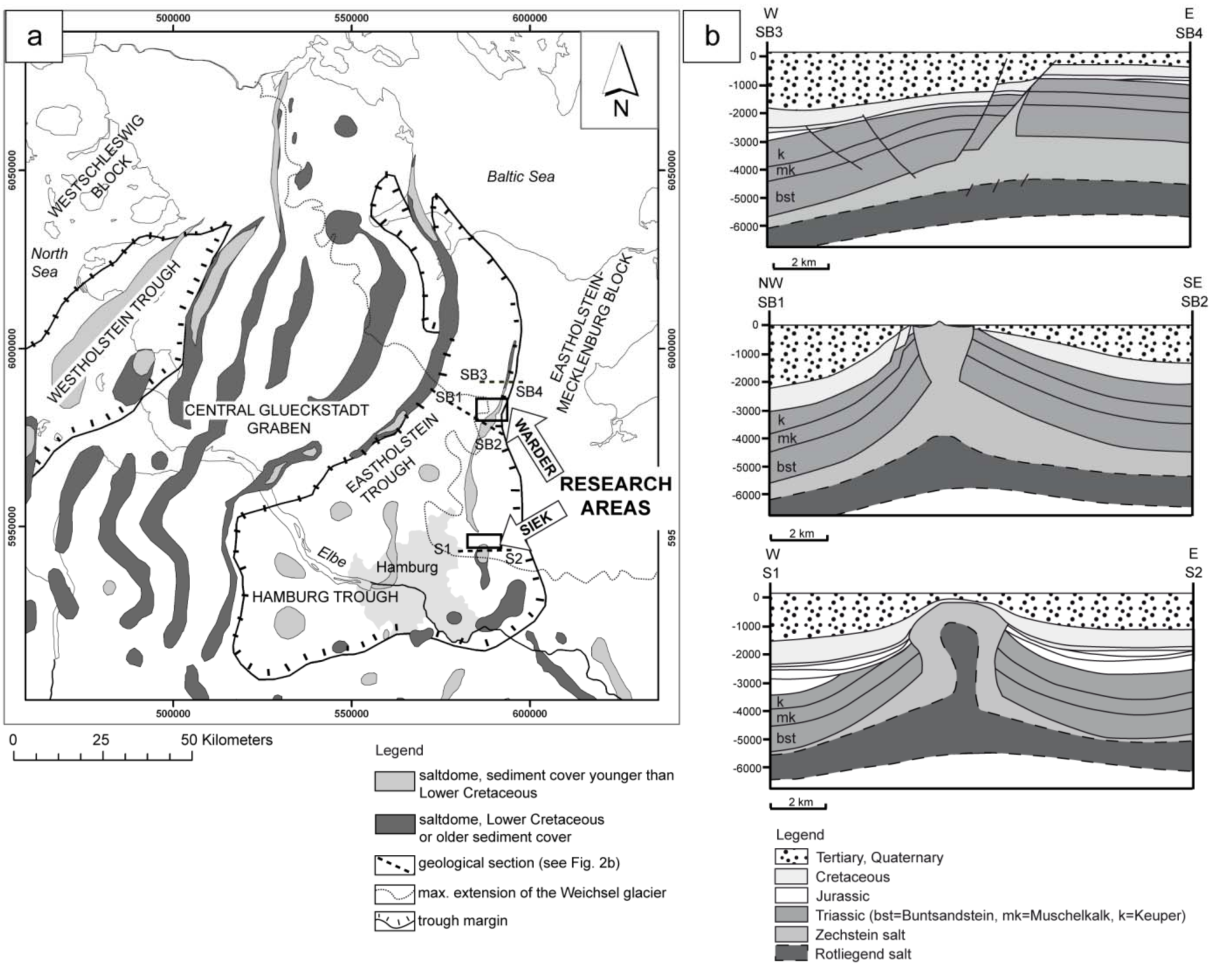

Fig. 5.2: (a) Structural map of the Glückstadt Graben realm with the location of the research areas Siek and Warder, the location of geological sections and the maximum extension of the Weichselian boulder deposits, modified after Maystrenko et al. (2005a); positions of salt domes after Baldschuhn et al. (2001); (b) geological sections after Baldschuhn et al. (2001).

The earliest salt movements in the GG can be attributed to the Triassic, when the central Triassic graben was generated under an extensional regime. The strongest salt movements coincide with the maximum E–W extension during the middle to late Triassic and were possibly triggered by normal faulting of the salt base (Maystrenko et al., 2005b; Scheck-Wenderoth et al., 2008). The former narrow trough in the central graben part broadened. The regional extension regime during the Triassic may have caused reactive diapirism (Jackson et al., 1994) which led to the formation of rim synclines in the central part of the GG. During the Jurassic a new pulse of salt activity started due to regional extension, possibly linked to normal faulting as documented in the Lower Saxony Basin and the Pompeckj Block (Maystrenko et al., 2005b). At the margin of the central GG realm the Westholstein-, Hamburg and Eastholstein- Troughs developed and strong salt movements took place at the margins of the former Triassic graben. The Jurassic salt activity leads to a second generation of rim synclines beneath the Triassic structures (Scheck-Wenderoth et al., 2008).

The early Cretaceous is recorded as tectonically quite phase, indicated by the rather uniform sediment cover which implies ceased salt movement (Maystrenko et al., 2005a). The late Cretaceous–early Tertiary basin inversion of the CEBS is not recorded in the GG but the salt walls in the marginal troughs grew up reacting to the compressive regime (Scheck-Wenderoth et al., 2008). A renewed tectonic activity in the Cenozoic is marked by rapid subsidence in the troughs during the Paleogene and Neogene. This youngest phase is characterised by the growth of N–S striking salt structures due to salt pillow depletion under an E–W extensional regime (Maystrenko et al., 2005b). The today distribution of sediments in the Glückstadt Graben reveals that sedimentation centre shifted from the central part in Triassic times toward the margins and shows that salt depletion of the Permian salt played a role in the structural evolution of the realm (Maystrenko et al., 2005b; Sannemann, 1968; Scheck-Wenderoth et al., 2008). In Bad Segeberg and Lüneburg the evaporite caprock pierced the glacial deposits and reaches the surface.

5.2.2 Research areas

The areas under investigation across the salt structures Siek-Witzhave and Sülberg-Segeberg were chosen after the examination of the data published in “Geotektonischer Atlas von Nordwestdeutschland und dem deutschen Nordsee-Sektor” (Baldschuhn et al. 2001) and available seismic sections (Wiederhold et al., 2003). The sites had to comply with the following requirements:

- Salt structure beneath the surface or
- Salt tectonic related faults, reaching the surface.

In this paper we present the results of two research zones that fulfil the requirements, the Siek salt dome east of Hamburg and the Segeberg-Sülberg salt structure that expands in N–S direction until Plön.

5.2.3 Siek-Witzhave salt structure

The Siek-Witzhave salt structure can be divided into two domes, the northern Siek dome and the southern Witzhave dome. Our research area is located across the younger Siek dome, so, in the following, we focus on the evolution of the Siek salt dome. Basic data of the Siek salt diapir are described by Baldschuhn et al. (2001) and Schmitz (1984). The maximum extension of the top is about 15 km^2 and the height from the pillow to the top up to 3500 m. The roof of the diapir is covered with sediments of the upper Cretaceous, Tertiary and Quaternary, but the central roof part is strongly eroded, so the thickness of the sediment cover is only about 10 m at this point. The salt pillow stage is supposed to have begun in the lower Triassic and the diapir stage in the Dogger. The rise of the salt dome still proceeds and the prospects are that the rising will continue given the possible supply from the pillow.

In the Siek area, 2 lines were sampled twice. The research area is located between the villages Siek and Lütjensee and the sampling was carried out in April and May 2011. The northern traverse BB extends in SW–NE direction about 440 m (Fig. 5.3a). During the two sampling days, on 44 sites we collected soil gas samples and soil samples. The southern traverse FW (Fig. 5.3a) extends about 465 m nearly in E-W direction. The bedrock consists of ground moraine materials of the Weichsel glacier and the soil cover is classified as podzol or lessivé, composed of boulder clay and sand. During the sampling in May 2011 114 soil gas samples were collected at 57 points, along with soil samples. Both profiles are assumed to cross the margin of the Siek salt dome.

5.2.4 The Segeberg-Sülberg salt structure

The Segeberg- and Sülberg salt structures attribute to the evolution of the GG during the Triassic and the following differentiation of the NGB in the Westholstein Block, the GG, and the Eastholstein Block. The basic data are described by Schmitz (1984). The salt structure strikes about 50 km in N–S direction and consists of Zechstein Salt and presumably Rotliegend salt in the lower parts. The diapir stage in the Segeberg area supposedly begun during the Tertiary, whereas the genesis of the southern Sülberg part is assumed to have initiated in the lower Triassic possibly linked to a basement fault. The pillow stage in the Sülberg area was reached in the upper Triassic to lower Cretaceous and continued until the lower Tertiary; the piercement of the diapir took place in the Miocene and proceeds until today. A link to the Siek structure to the south is most probable.

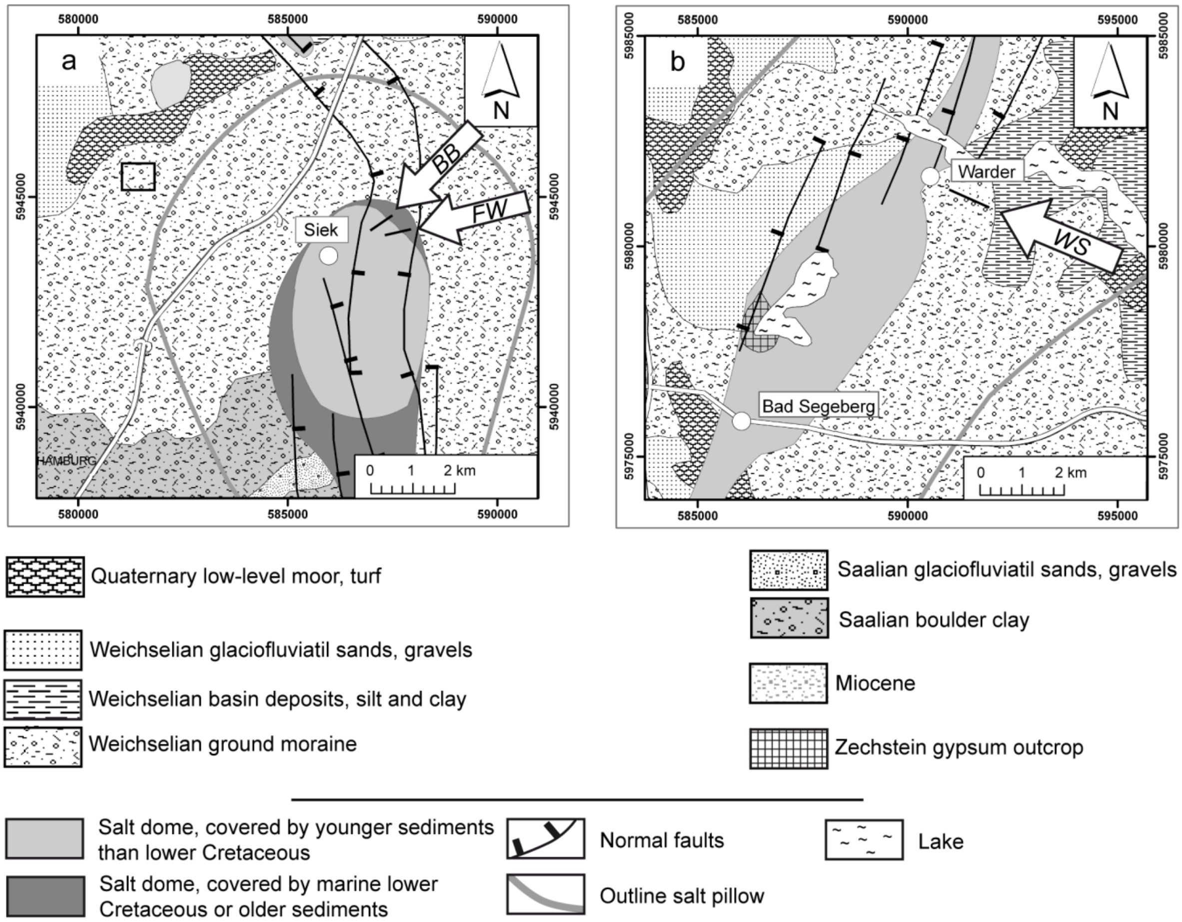

Fig. 5.3: Detailed map of the research areas; (a) Siek research area with the position of the BB- and FW-traverses (dashed lines); (b) Warder research area with the position of the WS - traverses. Position of salt domes and faults after Baldschuhn et al. (2001), geological formations adopted from BGR (2007).

The lake of Bad Segeberg is a subrecent subrosion feature which evolved during the Quaternary. The salt pillow building took place from late Triassic until the early Tertiary and the piercement occurred during the Miocene or later (Schmitz, 1984). To the north the salt dome continues in salt filled fracture. In the cave of the “Bad Segeberger Kalkberg” actual uplift rates are about 1.2 mm/a (Meier, 2003) whereas other authors reported 0.5 mm/a (Jaritz, 1980; Sirocko et al., 2002). Since the last glaciation the uplift amounted to 12 m (Meier, 2003). The stratigraphic succession is displaced along a westward-dipping normal fault which was generated in the Tertiary (Schmitz, 1984) (Fig. 5.2b, section SB3-SB4).

In the Warder research area the traverse WS (Fig. 5.3b) was sampled on two days in April and May 2011. The sampled traverse extends about 880 m in NW–SE direction and is located beneath the village Warder, south of the lake of Warder. It runs parallel to a section of the seismic profile published by Wiederhold et al. (2003). The bedrock consists of ground moraine materials of the Weichsel glacier and the soil is classified as pseudogley which is formed by boulder clay and overlying boulder sand. Soil gas samples were collected at 55 sites and soil samples were investigated stemming from 28 sites.

5.3 Methods

5.3.1 Soil gas samples

The ^{222}Rn in soil gas sampling was carried out applying three different sampling strategies according to the research aim: profile sampling, map sampling and vertical sampling.

The ^{222}Rn in soil gas profiles were aligned perpendicular to the assumed margins of salt domes. The sampling depth was 100 cm throughout all the ^{222}Rn profile surveys. To ensure equal conditions and comparable results it is important to carry out the sampling of a profile on a single day. For this reason, and due to the length of the profiles, each site was visited twice, which gave the possibility to sample more detailed sections and to choose the adequate points for soil sampling. Further, this protocol reveals the advantage to compare two intrinsic measurement series of the same site and to monitor permanent trends of the ^{222}Rn in soil gas distribution. To get regional information we applied the ^{222}Rn map sampling proposed by Kemski et al. (1996b). The sampling points are arranged in a triangle, distanced by 5 m from each other.

A further strategy was applied to get information about the vertical ^{222}Rn in soil gas distribution. Soil gas samples were taken at a single point in 25 cm distances from -0.25 cm down to -150 cm. Each point was sampled twice and the prevailing meteorological conditions were recorded.

The sampling iron pipes were pushed to the depth of 100 cm and connected to a manual pump to evacuate the residual atmospheric air in the pipe. Empirical testing revealed that 10 times of pumping previous to the first soil gas suction removes the contaminant atmospheric air accumulated in the pipe during the grab sampling. The pipes were sealed after the first sampling. Prior to the second sampling, 5 pumps were performed. The vertical samplings were carried out pushing the pipes to the different depths subsequently. Using a syringe a volume of 120 ml of soil gas was drawn up and a quantity of 100 ml was filled into a Lucas cell (with equal total volume capacity) that had been evacuated prior to use. After the acquired equilibration time between ^{222}Rn and its short lived alpha emitting progenies, ^{222}Rn in soil gas was measured with the scintillation counter “Sisie”. For a detailed description see Künze et al. (2012). Each soil gas sample was measured six times for 15 s. The ^{222}Rn activity in a 1 m^3 soil volume was calculated from the arithmetical mean resulting of the measurement series of each soil gas sample. Samples of atmospheric air near the soil surface were collected to control the exhalation of ^{222}Rn from the soil; the ^{222}Rn concentration in these samples was always negligible. To minimize the error induced by the entered atmospheric air we deal with the maximum of ^{222}Rn in soil gas values measured throughout this paper. The measurement inaccuracy is about 20-30% for 1–20 kBq/m^3; 10–20% for 20–40 kBq/m^3 and ≤10% for results > 40 kBq/m^3.

5.3.2 Soil samples

At selected sampling points soil samples were collected using a steel sampling tube. The soil core from 90–100 cm depth was placed in a plastic bag, closed and put in a cool box to avoid evaporation. With a slide, a known volume of undisturbed soil core was separated from the core to determine the wet bulk density. Water content of soil samples was determined in duplicate after drying the samples in an oven at 105°C. Using the obtained values the dry bulk density was calculated (Koroleva et al., 2011).

5.4 Results

In the research area in Schleswig-Holstein 410 soil gas samples were collected during the field work from April to July 2011. The main part of sampling (312 samples) has been carried out to reveal if the ^{222}Rn in soil gas concentration varies across the margins of salt structures. According to the results the sites for vertical sampling were selected, and 92 samples were taken from different depths.

Table 5.1: Basic data overview of the surveys carried out and the prevailing meteorological conditions during the sampling.

Survey name	Date	*n**	*T* °C	±stdv	Atmos.press. hPa	±stdv	Air moist. %	±stdv
profiles								
BB_1	Apr 11	17	27.1	2.9	1046.9	1.8	29.3	2.5
BB_2	Apr 11	27	12.4	1.9	1056.5	0.8	42.8	1.6
FW_1	May 11	28	27.1	2.6	1059.5	1.6	28.9	3.1
FW_2	May 11	29	22.6	3.7	1046.6	5.8	52.6	11.0
WS_1	Apr 11	25	28.1	2.9	1063.2	2.1	27.7	2.3
WS_2	May 11	30	13.6	3.3	1072.8	2.6	35.6	2.8
Depth measurements								
BT_1	June 11	6	26.4	0.5	1030.0	0.0	48.7	0.7
BT_2	June 11	6	26.3	0.2	1029.4	0.5	51.8	2.8
FT_1	June 11	6	26.9	0.3	1026.0	1.4	49.5	1.5
FT_2	June 11	6	25.1	0.8	1025.4	0.0	53.8	0.9
WT_1	June 11	6	27.3	0.4	1028.5	0.3	44.8	1.5
WT_2	June 11	6	27.2	0.3	1028.4	0.6	45.1	0.9
Moraine measurements								
MM	July 11	3	23.8	1.5	1009.8	0.0	51.7	4.2
MT_1	July 11	6	21.8	0.2	1009.8	0.0	53.1	1.3

**n*= number of measurements

Table 5.1 shows the surveys, the number of measured points and the meteorological conditions prevailing during the field work. The temperature varied between 12.4 and 28.1°C and the atmospheric pressure ranged between 1009.8 and 1072.8 hPa, showing a negative linear correlation with air moisture content, which runs from 27.7 to 53.8 %.

The frequency distribution of the calculated results of the ^{222}Rn in soil gas measurements are plotted in Fig. 5.4. Fig. 5.4a shows the frequency distribution of the 156 ^{222}Rn in soil gas values of the profile data. The ^{222}Rn activity in soil gas ranges from 5 to 105 kBq/m^3 with an arithmetic mean of 33 kBq/m^3 and a median of 27 kBq/m^3. The maximum and minimum values of each profile were investigated by vertical sampling. The ^{222}Rn in soil gas frequency distribution of the vertical ^{222}Rn profiles reveals an arithmetic mean of 31 kBq/m^3 and a median value of 27 kBq/m^3 (Fig. 5.4b). The water content of the soil samples varies between 5.40 and 29.75 wt% with an arithmetic mean of 14.27 (Fig. 5.4c).

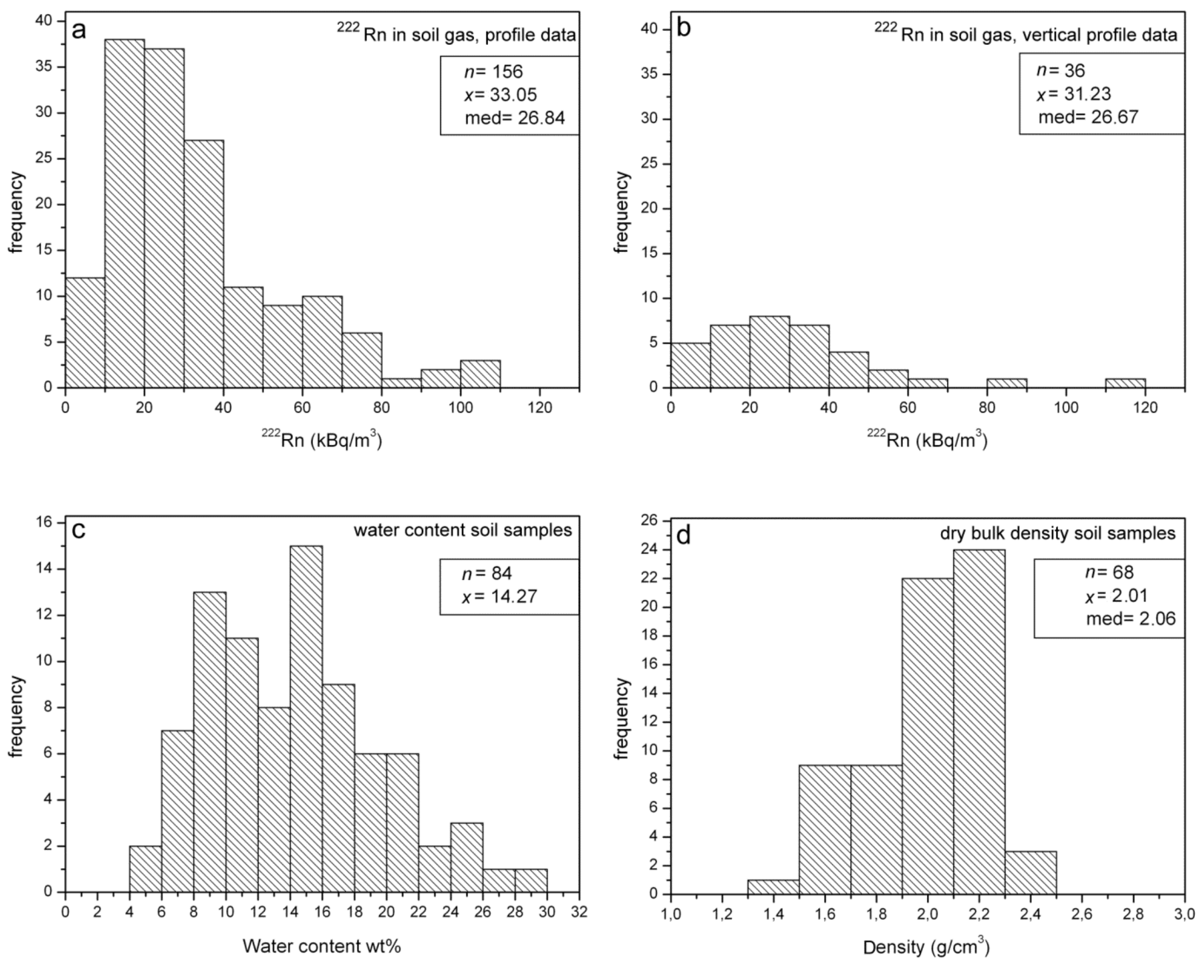

Fig. 5.4: Frequency distribution of the data presented in this paper; *n*= number of measurements, *x*= arithmetic mean, med= median value.

The soil samples of the two traverses in the Siek research area yield an average water content of 9.76 % and 19.82 % for samples collected in April 2011 and May 2011 respectively (Table 5.2). The soil samples of the Warder research area reveal an average value of 13.61% (Fig. 5.4c; Table 5.2).

The dry bulk density of 68 soil samples ranges from 1.37 to 2.33 g/cm^3 (Fig. 5.4d) and reveal an arithmetic mean of 2.01 g/cm^3 (Table 5.2). The density values calculated for the FW_2 samples are elevated and it has to be assumed some inaccuracy, as the expected maximum bulk dry density in unconsolidated sediments is about 1.8–2.2 g/cm^3 (Table 5.2). Throughout the sampled sections the estimated grain size distribution ranges between argillaceous and arenaceous.

Table 5.2: Ranges and averages of ^{222}Rn concentrations in soil gas of the profile surveys and map survey, ranges and arithmetic means of water content and dry bulk density of the soil samples.

		^{222}Rn in soil gas				Water content			Bulk density dry		
Name	**Length**	***n****	**range**	**mean**	**med**	***n***	**range**	**mean**	***n***	**range**	**mean**
	m		kBq/m^3	kBq/m^3	kBq/m^3		wt%	wt%		g/cm^3	g/cm^3
Siek profiles											
BB_1	400	17	15 – 86	36	26						
BB_2	255	27	5 – 105	40	33	27	13.67 – 29.75	19.82	27	1.50 – 2.31	2.06
FW_1	465	28	8 – 73	26	21						
FW_2	450	29	5 – 64	25	22	29	5.68 – 16.63	9.53	13	1.54 – 2.33	2.07
Warder profiles											
WS_1	600	25	10 – 103	37	34						
WS_2	620	30	12 – 99	36	33	28	5.40 – 21.20	13.61	28	1.37 – 2.28	1.93

**n*= number of measurements

5.4.1 *Considerations of background for ^{222}Rn in soil gas*

The aim of this work is to investigate if salt structures induce elevated ^{222}Rn activities in the soil gas located above them, in other words, if it is possible to trace the margin of salt structures in the underground by the rather surface near ^{222}Rn concentration in soil gas. In order to define the term "elevated ^{222}Rn activity" we need a definition of the natural background ^{222}Rn concentration in soil gas that is a result of the geochemistry of the underlying bedrock. Several methods are reported in the literature to estimate this background information as average values beneath maxima values (King et al., 1996) from statistical methods (Baubron et al., 2002) or from the diffusive ^{222}Rn signal (Kemski, 1993). Due to the lack of ^{226}Ra in soil data of the research area, an approach is desirable which would give a reasonable value including the local potential for high ^{222}Rn activity in soil gas. For this purpose we selected an area known for its granitic moraine boulder material deposits: Wartenberge (Fig. 5.3). The presence of granitic glacial boulder material implies high radionuclide contents compared to the autochthonous sediments deposited in Schleswig-Holstein, e.g. sands, gravels and clays, and as a result the maximum possible ^{222}Rn activity in soil gas. According to the map sampling strategy of Kemski et al. (1996b) in the area of Wartenberge three sites were sampled twice. The median value of the moraine measurements (MM_series) is 34 kBq/m^3.

Table 5.3 summarises the ^{222}Rn in soil gas concentrations of the prevailing sediments in northern Germany, as published in Kemski et al. (1999, 2002). The highest ^{222}Rn activity in soil gas was found in

Weichselian basin sediments with a median value of 47 kBq/m^3. The median value of our map sampling is in good agreement with the results for Weichselian ground boulder material (Table 5.3).

Table 5.3: Typical ^{222}Rn in soil gas values (median values in kBq/m^3) of lithologies occurring in the research areas.

	Glacial sands	Glacial loam	Quaternary	Weichselian	Tertiary	Weichselian ground boulder	Weichselian basin sediments	Weichselian fluvial sediments
Kemski et al. (1999)	11(53)*	14(70)	12(204)	20(36)	28(25)			
Kemski et al. (2002)	11(165)	31(245)	14(367)	23(178)	37(87)	36(109)	47(4)	13(78)
	Weichselian granitic boulder (Wartenberge)							
MM_series (this work)	**mean 31 (6)** **med 34** **max 40**							

*()= number of measurements

To ensure the quality of our definition of elevated ^{222}Rn values in soil gas (peaks) in this work, we deal with the maximum value of ^{222}Rn concentration in soil gas measured in the MM_series as regional background value bg_{mmax}. This maximum value was used as the critical value to differentiate the elevated ^{222}Rn values in the profile measurements from background values, or in other words, to define peaks and peakzones. To get insight into the local background (bg_{loc}) of the profile measurements the arithmetic mean of the values beneath the elevated zones was calculated for each profile.

5.4.2 Soil gas profile description

a) Siek

Across the Siek salt dome the BB- and FW-^{222}Rn in soil gas surveys were carried out at two sites in April and May 2011; each survey consists of two sampling traverses (Table 5.2; Fig. 5.3a). The traverses BB_1 and BB_2 consist of 17 and 27 sampling points, respectively. The traverses FW_1 and FW_2 consist of 28 and 29 sampling points. The ^{222}Rn in soil gas concentration ranges from 5 to 105 kBq/m^3; the latter represents the highest value measured throughout all profile surveys. The arithmetical mean is 31 kBq/m^3 and the median value about 24 kBq/m^3 (Fig. 5.5).

BB_Series

The ^{222}Rn activity in soil gas along the traverse BB_1 varies from 15 to 86 kBq/m^3 with an average of 36 kBq/m^3. With regard to the background applied in this work the bg_{loc} is 26 kBq/m^3. The maximum value within the profile BB_1 is about three times higher than bg_{loc} and twice the bg_{mmax} (Fig. 5.6a). The first 250 m of the sampled traverse show a rather uniform ^{222}Rn in soil gas activity and the section between 250 m to the end of the sampled traverse reveals elevated

^{222}Rn in soil gas activity, forming a kind of a “twin peak” feature (King et al., 1996).

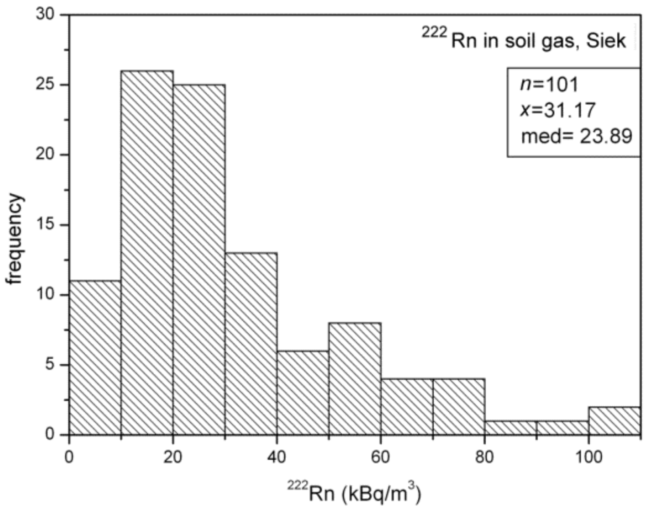

Fig. 5.5: Frequency distribution of the ^{222}Rn concentrations in soil gas of the Siek research area.

The profile BB_2 starts at the 175 m distance of profile BB_1. The closer setting of sampling points (up to 5 m) in BB_2 allows for a higher resolution of the defined peakzone BB_1. From the 250 m sample point of BB_1 onwards the ^{222}Rn in soil gas concentration increases up to 105 kBq/m^3 (Fig. 5.6b). Excluding the values higher than bg_{mmax}, the local background of BB_2 is 21 kBq/m^3. It follows that the maximum value of BB_2 is about 5 times higher than the local background. Regarding the general background bg_{mmax}, the elevated values form peaks more than twice the background.

Fig. 5.6c shows an overlay of the traverses BB_1 and BB_2. The zones of elevated ^{222}Rn activity in soil gas overlap. The single graphs (Fig. 5.6a, b) show a different shape due to the different sampling distances between the points, but also show that the intensity of the ^{222}Rn in soil gas signal differs, although the trend is consistent. The average of the ^{222}Rn in soil gas concentration in the BB_series is 38 kBq/m^3. The traverse BB_2 reveals a greater range of ^{222}Rn in soil gas activity with a minimum of 5 kBq/m^3 and a maximum of 105 kBq/m^3 compared to BB_1. Further, the higher sampling resolution clearly reveals three maximum values at about 300–320 m, 325–370 m and 380–410 m. Between the peak zones of BB_1 and BB_2 there is a slight shift in the position on the x-axis which may be caused by GPS deviation.

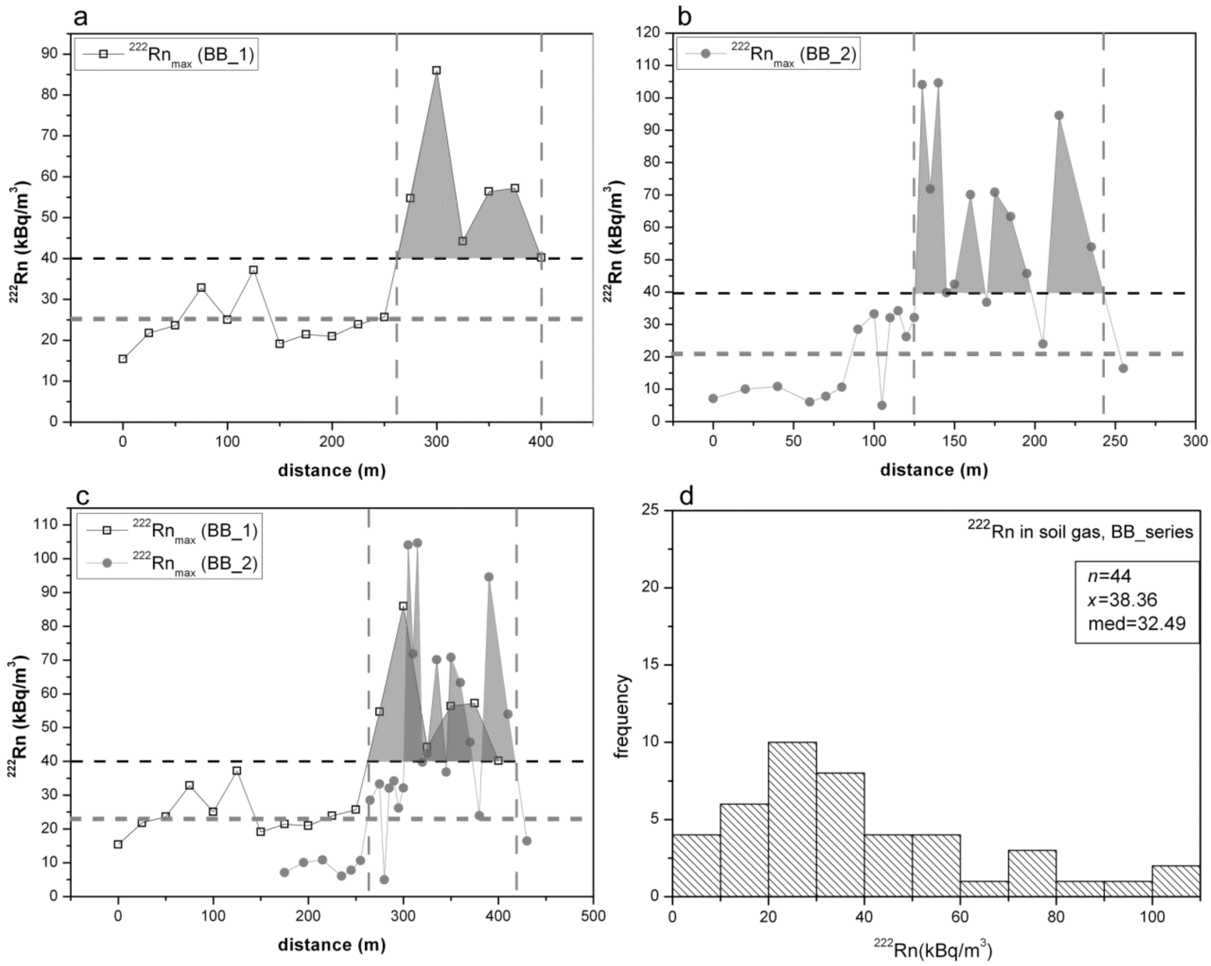

Fig. 5.6: Graphical interpretation of the measured profiles; (a) soil gas profile BB_1 sampled in April 2011; (b) soil gas profile BB_2 sampled two days after the BB_1 traverse; (c) fit of both traverses; (d) frequency distribution of the ^{222}Rn in soil gas values of the series. Black dashed line = bg_{mmax}, grey dashed line = bg_{loc}.

FW_Series

In the traverse FW_1 the ^{222}Rn in soil gas activity ranges from 8 to 73 kBq/m^3 (Fig. 5.7a, b). The average value is about 26 kBq/m^3 (Table 5.2). Three clearly defined elevated regions can be differentiated with reference to the bg_{mmax}. The bg_{loc} is about 19 kBq/m^3. Regarding bg_{loc}, the maximum value of ^{222}Rn activity in FW_1 is nearly four times higher. The maxima are also clearly separated from the bg_{mmax}. The ^{222}Rn in soil gas values do not form such a clear cut zone of elevated ^{222}Rn in soil gas concentration compared to the BB_series, however two zones of elevated values can be identified at a distance of 100 and 275–375 m.

The traverse FW_2 starts at the 50 m distance of FW_1. The ^{222}Rn in soil gas concentration lies in the same range as FW_1 with an arithmetic mean of 25 kBq/m^3. Several elevated values can be observed in the first 100 m of the traverse and also between 275 and 425 m. The bg_{loc} is 18 kBq/m^3 and the maximum value measured in this traverse is about three times higher.

Regarding the matching features of both profiles, a number of differences are revealed at a first glance (Fig. 5.7a). The position of the maximum values varies slightly and so does the ^{222}Rn concentration. Nonetheless, zones of elevated ^{222}Rn in soil gas concentration and zones of low ^{222}Rn in soil gas activity match with each other. In summary a zone of elevated ^{222}Rn in soil gas concentration is located at a distance of 75-150 m (Fig. 5.7a), followed by a zone of low ^{222}Rn in soil gas activity up to the 255 m distance. In the range from 255 m to 400 m distance, the ^{222}Rn in soil gas activity again shows elevated values.

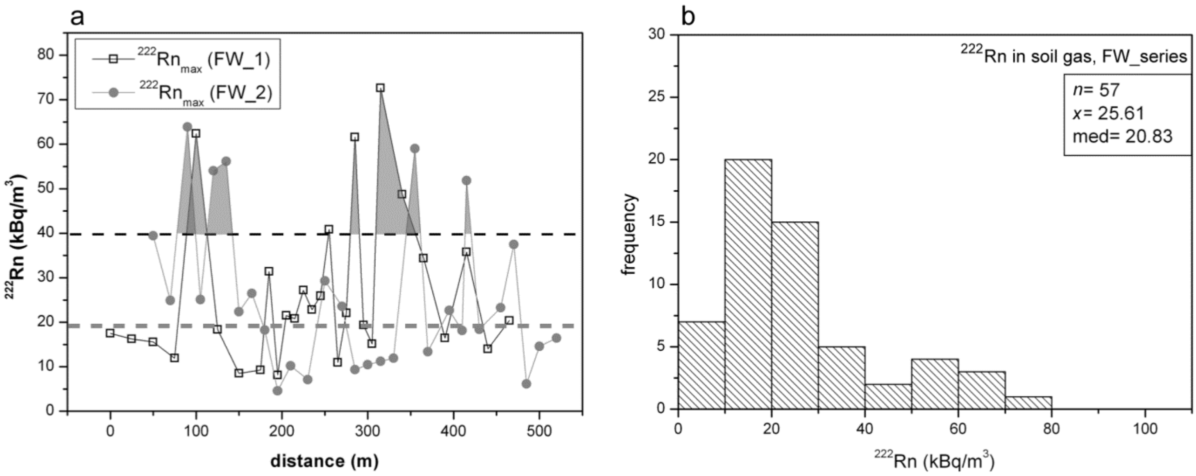

Fig. 5.7: (a) Soil gas profiles FW_1 and FW_2, zones of elevated ^{222}Rn in soil gas values are marked in grey. Black dashed line = bg_{mmax}, grey dashed line = bg_{loc}; (b) frequency distribution of the ^{222}Rn values.

b) Warder

Across the Segeberg-Sülberg salt dome two soil gas profiles were sampled at one site in April and May 2011 (Fig. 5.3b). The traverse WS_1 and WS_2 comprise 25 and 30 sampling points, respectively (Table 5.2). The ^{222}Rn in soil gas concentration ranges from 10 to 103 kBq/m^3. The arithmetical mean is 37 kBq/m^3 and the median value lies around 34 kBq/m^3 (Table 5.2; Fig. 5.8b). The ^{222}Rn in soil gas activity of traverse WS_1 ranges from 10 up to 103 kBq/m^3 and the average value is 37 kBq/m^3. With reference to the bg_{mmax}, there are 4 zones of elevated ^{222}Rn in soil gas activity, one at 0–100 m, one at 250–300 m, one at 375–450 m and one at 600 m distance (Fig. 5.8a). The elevated ^{222}Rn in soil gas concentration is about 70 kBq/m^3, except for the maximum value measured at the last sampling point of this traverse. The bg_{loc} value is about 28 kBq/m^3.

The traverse WS_2 starts at the 200 m distance of WS_1 (Fig. 5.8a). The ^{222}Rn activity of the measured soil gas samples range from 12 up to 99 kBq/m^3, the average value is about 36 kBq/m^3 (Table 5.2). Several zones of elevated ^{222}Rn in soil gas activity can be distinguished; the most obvious is the maximum value at 430 m distance (Fig. 5.8a). The local background is about 26 kBq/m^3.

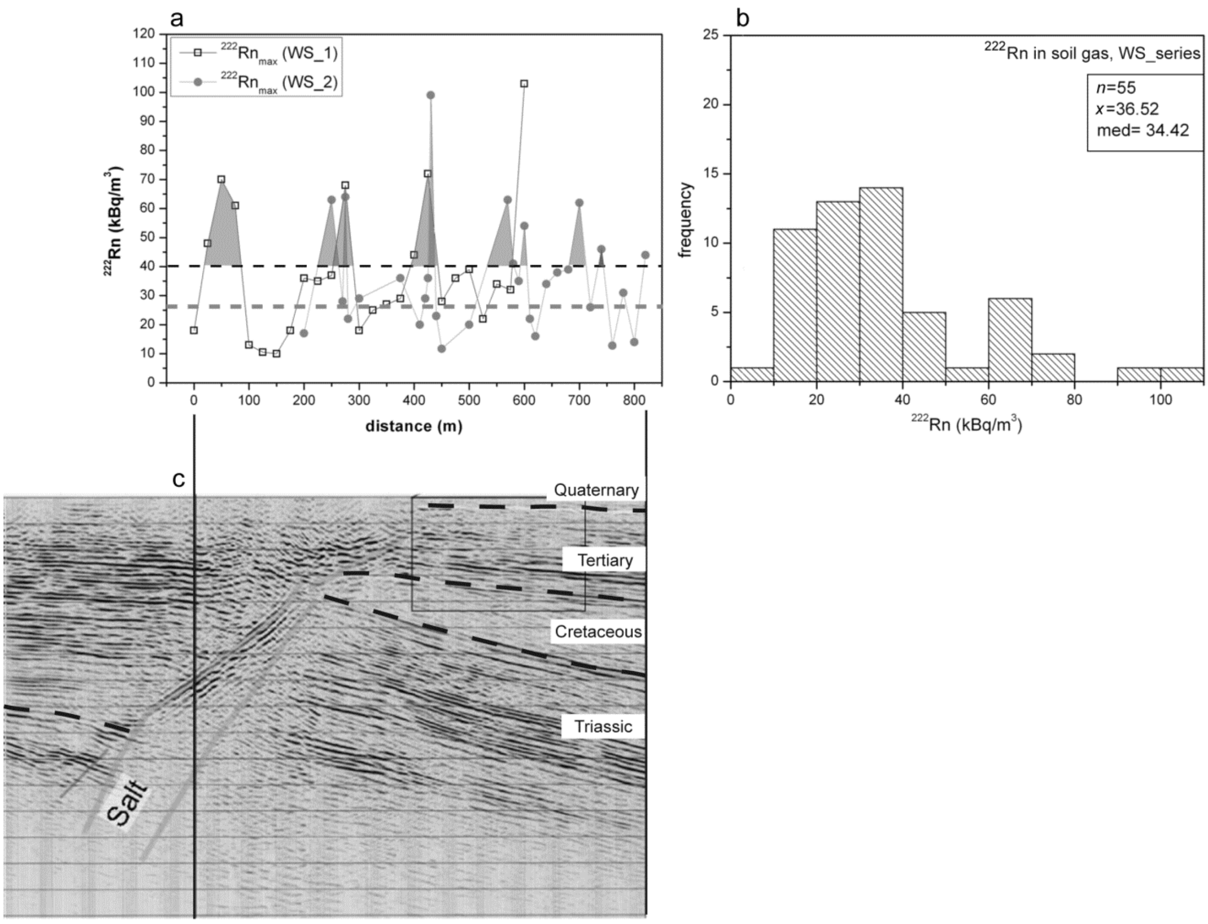

Fig. 5.8: (a) Soil gas profiles WS_1 and WS_2, zones of elevated ^{222}Rn in soil gas values are marked in grey, black dashed line = bg_{mmax}, grey dashed line = bg_{loc}; (b) frequency distribution of the ^{222}Rn values; (c) seismic profile adopted from Wiederhold et al. (2003), fitted into position of the soil gas profile.

Fig. 5.8a shows the overlay of both WS_1 and WS_2. The distance between the sampling points of WS_2 is closer and it follows that the second peakzone recognised in WS_1 in this higher resolution sampling splits into two peaks. The third peakzone of WS_1 is also present in WS_2 and reveals even higher ^{222}Rn in soil gas values. The opposite situation is found in the fourth peakzone, the maximum value of WS_1 is not present in WS_2. Despite this, a peakzone (twin peak zone) is present in WS_2 between 500 and 600 m distance. A fifth peak appears in profile WS_2 at 700 m distance. Both traverses are in good agreement with each other, as the trends are unambiguously reproducible. The WS-traverses expand parallel to a seismic profile published in Wiederhold et al. (2003) which is shown in Fig. 5.8c. The rising salt produces several normal faults in the overlying Tertiary sediments. Baldschuhn et al. (2001) describe a westward-oriented normal fault related with the salt structures, the Segeberg-Plön structure zone. It expands parallel to the margin of the Eastholstein Block. Along this fault salt intruded. The seismic profile shows a NW directed normal fault with a dip of 35° (Fig. 5.8a). The soil gas profile shows five zones of elevated ^{222}Rn in soil gas values, three of them are located in the overlapping area of WS_1 and WS_2 and could be detected twice, thus possibly caused by fault related pathways.

5.4.3 Vertical sampling

Table 5.4 and Fig. 5.9 show the results of the vertical sampling of ^{222}Rn in soil gas. A clear trend can be observed, as the results for -25 cm depth throughout the depth profiles are lower compared to the ^{222}Rn in soil gas concentration in -150 cm depth.

Table 5.4: Results of the vertical sampling of ^{222}Rn in soil gas measurements.

Name	-25 cm kBq/m^3	-50 cm kBq/m^3	-75 cm kBq/m^3	-100 cm kBq/m^3	-125 cm kBq/m^3	-150 cm kBq/m^3	mean kBq/m^3	med kBq/m^3
Siek vertical sampling								
BT_1	6	15	19	23	39	48	25	21
BT_2	6	29	38	45	51	68	40	42
FT_1	6	11	14	23	24	31	18	19
FT_2	6	11	16	21	33	35	20	19
Warder vertical sampling								
WT_1	12	30	42	54	87	120	57	48
WT_2	9	22	25	28	40	33	26	27
Wartenberge moraine vertical sampling								
MT_1	9	13	20	21	24	30	19	19

Most of the vertical profiles show a continuous increase of the ^{222}Rn concentration with depth, except the -125 cm value in FT_1 and the -100 cm value in MT_2 (Fig. 5.9). In the course of the vertical samplings the 100 cm depth was also sampled, delivering additional information of the general ^{222}Rn in soil gas concentration one to two month after the profile sampling. A comparison of the ^{222}Rn in soil gas values of these triple sampled points along with the large differences the values reveal is summarised in Fig. 5.10.

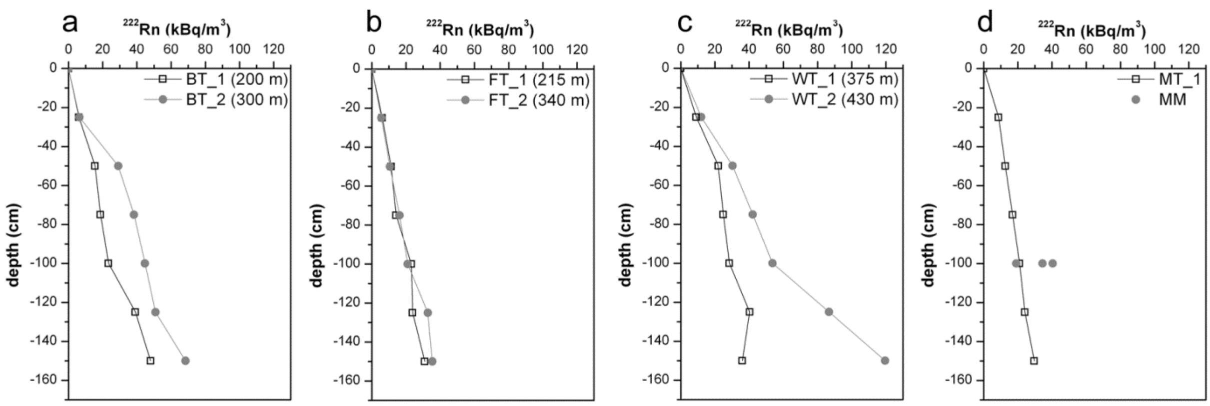

Fig. 5.9: ^{222}Rn in soil gas results of the vertical samplings; (a) BB_series, vertical sampling at 200 and 300 m distance; (b) FW_series, vertical sampling at 215 and 340 m distance; (c) WS_series, vertical sampling at 375 and 430 m distance; (d) moraine measurement, MM_series, MM points = map sampling strategy (Table 5.2).

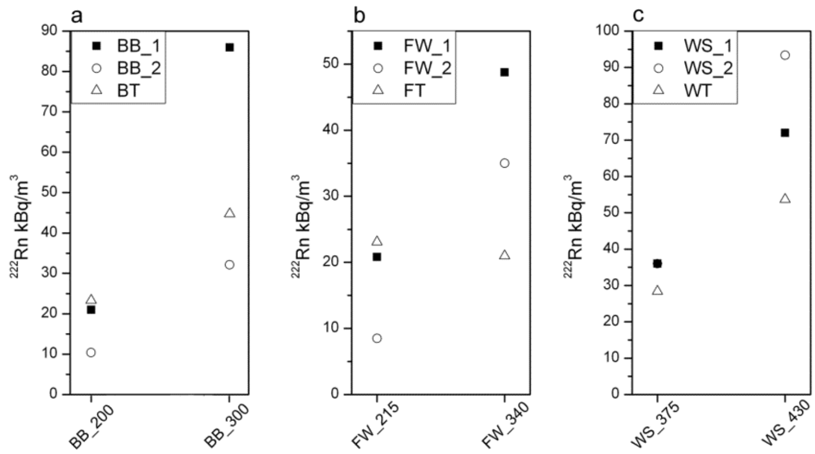

Fig. 5.10: Comparison of the triple sampled points (vertical sampling and 2 profile samplings); (a) BB_series; (b) FW_series; (c) WS_series.

5.5 Discussion

The investigations of Kemski et al. (1999, 2002) showed that the ^{222}Rn in soil gas distribution in northern Germany correlates with the distribution of the geological units. The highest ^{222}Rn in soil gas activity is concentrated at the eastern part of Schleswig-Holstein, where the sediments of the Weichselian glacier prevail. In comparison to the older Elster and Saale glaciations, the Weichsel deposits are characterised by granitic and porphyry boulder material which implies high radionuclide contents and enhanced ^{222}Rn in soil gas potential. Further, the authors ascribe a rather high permeability to the glacial sediments, which supports a high emanation and migration rate. They measured local ^{222}Rn activities higher than 100 kBq/m^3.

The interpretation of Kemski et al. (1996b, 1999) that the elevated ^{222}Rn in soil gas concentration correlates with the Weichselian deposits is supported by the results of Birke et al. (2009), who demonstrated elevated uranium concentration in the area covered by the granitic till of the Weichselian glacier. Because the maximum value of ^{222}Rn in soil gas values that we measured in Wartenberge are 40 kBq/m^3 at 100 cm depth, we cannot assume that the radionuclide rich boulder material is the source of our elevated ^{222}Rn in soil gas concentrations which range up to 105 kBq/m^3. Since ^{222}Rn is mobile and can escape from its precursor, the correlation between a measured ^{222}Rn in soil gas concentration and the ^{226}Ra concentration in the adjacent materials is complicated (UNSCEAR, 1982). Migration paths as well as carriers and factors influencing the emanation must be taken into account.

The impact of glacial cover on ^{222}Rn in soil gas signals from a faulted bedrock has been investigated by Gates et al. (1990). These authors measured ^{222}Rn activity in soil gas above an inactive fault characterised by radionuclide rich pegmatite intrusions. The study revealed that the till cover superimposes the bedrock ^{222}Rn signal and the measured values reflect the till´s ^{222}Rn characteristics, which are highly variable. We measured ^{222}Rn in soil gas in till cover over active structures which cater for migration possibilities, maybe enhanced emanation and possibly radionuclide supply. The ^{222}Rn values along the sampled distances show significant variations, which visually form domains of high and low ^{222}Rn activity. Each traverse reveals at least one zone of elevated ^{222}Rn in soil gas concentration, evidently distinguishable from the bg_{mmax} and the bg_{loc} (Figs. 5.6a, b; 5.7a; 5.8a). The elevated ^{222}Rn concentrations vary with time. In the following section we give a general outline for the generation of ^{222}Rn.

Generally, the primary source of ^{222}Rn in soil gas is the geochemistry of the bedrock and the present amount of parent nuclides. ^{222}Rn is produced by α-decay from its parent nuclide ^{226}Ra. Due to the recoil effect ^{222}Rn atoms can be released from the mineral grain into the pore space; the amount of ^{222}Rn which reaches the pore space from a mineral grain is the emanation. The emanation or emanation power strongly depends on the location of the parent nuclide in the mineral grain, as the recoil range of a ^{222}Rn atom is about 20–70 nm (Monnin and Seidel, 1992). Despite reaching the pore space and remaining in there, the ^{222}Rn atoms can either penetrate into the adjacent mineral grains or stay in the source grain. Due to the above mentioned importance of the location of the parent nuclide in the grain, the emanation is strongly dependent on the medium`s grain size. Fracturing and cracking of rocks by faulting, seismic activity and alteration processes increase the inner surface and enhance the ^{226}Ra disposability for ^{222}Rn release.

Moisture has a further influence on the amount of ^{222}Rn atoms disposable in the pores, as water absorbs the kinetic energy of the recoil and prevents the irruption of ^{222}Rn atoms to adjacent mineral grains. Water molecules further occupy adsorption places at mineral surfaces, thus reducing the amount of adsorbing ^{222}Rn atoms.

The theory of ^{222}Rn release from the geological environment is described in Tanner (1964, 1980) and various empirical emanation rates for different rocks and soils exist in the literature. Once generated and having reached the pore space ^{222}Rn atoms move from their source by diffusion or advection; the driving forces are concentration gradients and pressure gradients, respectively (Etiope and Martinelli, 2002). Subordinate, ^{222}Rn can diffuse inside a solid lattice. The width of migration is strongly dependent on the permeability of the bedrock and soil cover. The ability to migrate and the special properties of ^{222}Rn make it so important in the earth sciences. Its inertness inhibits chemical reactions and the short half life constraints the moving distances and leads to the self-evident topicality of the ^{222}Rn occurrence measured near the surface. The physical diffusion- and advection processes are elaborately described by several authors, e.g. Etiope and Martinelli (2002); Kemski (1993). Both processes can be superimposed, whereas diffusion is independent of advection. Diffusion processes account for migration distances up to meters in dry media. In saturated media the diffusion width is even lower. Advection of ^{222}Rn in soil can occur in the gas phase in a dry medium and also in a wet medium by bubble motion. ^{222}Rn can also be solved in water and transported by water phase advection.

Several studies showed that the parent nuclide concentration measured in proximity to ^{222}Rn detectors is often lower than the measured ^{222}Rn signals in soil gas (Etiope and Martinelli, 2002) or ground water (Sundal et al., 2004; Wanty et al., 1991). Nevertheless, ^{222}Rn maps clearly show that uranium rich geological formations give rise to high ^{222}Rn risk (Appleton and Miles, 2010).

Due to the limited migration distance of ^{222}Rn caused by diffusion, the scientific community suggests advective migration of ^{222}Rn by carrier gases as the important process accounting for elevated ^{222}Rn concentrations related to geodynamic events and crustal deformation (Monnin and Seidel, 1992). Likewise, the transport by groundwater flow may account for limited spatial transport. Yet the mere existence of a carrier gas which moves meters a day makes the diffusion distance of ^{222}Rn negligible (Etiope and Martinelli, 2002). Advection of noble gases requires sufficient gas concentrations to react to pressure gradients. The amount of rare gases in the geological subsurface is too small and consequently the presence of carriers is essential for a larger distance transport. CH_4 and CO_2 are the most common carriers in the geological environment and their ascent flow along structural pathways is a well known phenomenon.

Exogene influences on ^{222}Rn in soil gas activity provide the meteorological conditions as reported by King and Minissale (1994) and Washington and Rose (1992). Up to certain moisture content, the ^{222}Rn emanation increases with increasing moisture content (Sundal et al., 2004). In the present work we compare ^{222}Rn values measured at equal points but different dates with the correspondent precipitation rates, which would provide a rationale for the occurred variations other than implied by tectonics. The variation of ^{222}Rn in soil gas values obtained during this work is shown in Table 5.5. The amount of precipitation over a period of 14 days before the sampling date was consulted in two meteorological archives of Germany. For clarity, we distributed numbers (1–3) from the lowest to highest ^{222}Rn value, respectively. The arithmetical mean of these classes shows the relative dimension of the results of distinct measurement dates. By assigning the appropriate precipitation rates it becomes evident that there is no trend that correlates precipitation rates and ^{222}Rn values based on the examined data (Table 5.5).

A dependency between moisture content of the soil and ^{222}Rn in soil gas activity has been reported in Menetrez and Mosley (1996) and Papastefanou (2010). Generally, plotting the water content of soil samples and the bulk dry density versus the ^{222}Rn activity in soil gas of all samples acquired during this work shows no correlation.

Table 5.5: Relative correlation between triple sampled points and precipitation within two weeks before the sampling and measurement took place; (a) BB_series; (b) FW_series; (c) WS-series.

a	11.04	13.04	27.06.
	BB_1	**BB_2**	**BT**
BB_200	*2*	*1*	*3*
BB_300	*3*	*1*	*2*
x	**2.5**	**1**	**2.5**
prec.			

b	09.05	11.05	27.06.
	FW_1	**FW_2**	**FT**
FW_215	*2*	*1*	*3*
FW_340	*3*	*2*	*1*
	2.5	**1.5**	**2**
prec.			

c	26.04	02.05	29.06.
	WS_1	**WS_2**	**WT**
WS_375	*2*	*2*	*1*
WS_430	*2*	*3*	*1*
	2	**2.5**	**1**
prec.			

precipitation high

precipitation low

In the following, we want to outline the structural and physical aspects related to the research area in order to infer other possible sources than till cover for elevated ^{222}Rn activities in soil gas. The geological environment in the research area can be briefly described in terms of sedimentary basin environment strongly influenced by salt tectonics and multiple glacial events. The existence of a nearly vertical salt dome rising up to the surface provides special conditions as salt influences the temperature, salinity and permeability of its environment. Apart from the glacial deposits as source for elevated ^{222}Rn in soil gas signals, the structural conditions implied by the salt dome itself and its influence on chemical and physical conditions in the environment may have an impact on ^{222}Rn activity in soil gas.

Kristiansson and Malmqvist (1982) developed a theory of geogas upflow through waterfilled fractures and ^{222}Rn transport by microbubbles. The experiments of Varhegyi et al. (1992) of microbubble transport of ^{222}Rn in water or water-saturated media proved the validity of the theory even for migration distances greater than 100 m. Heinicke and Koch (2000) investigated the role of bubble advection reacting on seismic activity and revealed hydrogeochemical anomalies related to earthquakes induced due to slug flow of CO_2 in water filled faults, with velocities up to 7–8 cm/s (Etiope and Martinelli, 2002). This high velocity allows deep source ^{222}Rn to reach the surface. Etiope and Lombardi (1995) describe high ^{222}Rn in soil gas values in faulted low-Ra clay and as explanation they took into consideration the carrier effect of ascending microbubbles. On their rise these microbubbles collect radionuclides from the geological formations, hence leading to a release at the groundwater surface and consequently an accumulation of ^{222}Rn and its precursors. Etiope and Lombardi (1996) observed the transport of radioactive particles through sand after bubbling the test column with air. The data suggest that elevated ^{222}Rn in soil gas occurrence caused by ascending microbubbles does not require a located source accumulation (Etiope and Lombardi, 1995). In the salt dome environment, a potential microbubble ascent would be supported by the Ostwald coefficient K for ^{222}Rn, which decreases with temperature and salinity increase (Clever, 1979). The role of ^{226}Ra transport by microbubbles is not completely investigated yet, but some authors reported that ^{226}Ra is transported mainly by gas flow (Spivak et al., 2008).

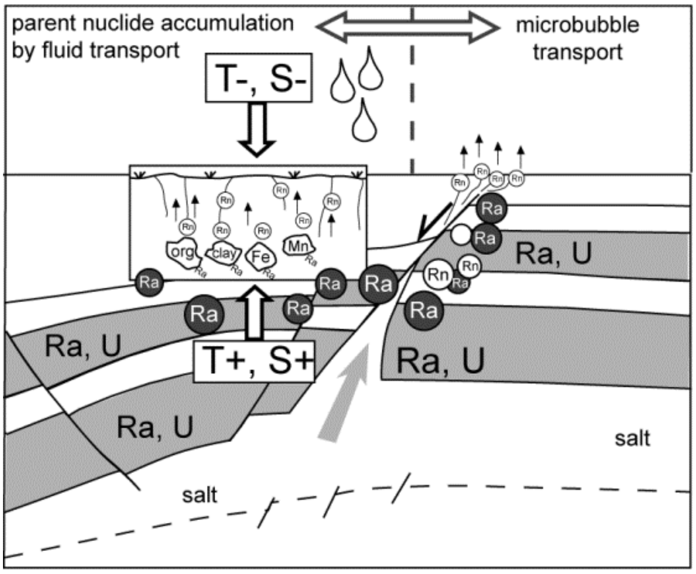

Fig. 5.11: Schematic sketch summarising the possible sources for elevated ^{222}Rn activities in the soil gas of a salt dome environment; T= temperature, S= salinity, Mn and Fe stand for Fe- and Mn-oxides and -hydroxides and org = organic matter, see text for explanation.

In Fig. 5.11 we present a theoretical model which can account for the existence of elevated ^{222}Rn concentrations in soil gas in a salt structure environment. As mentioned above, groundwater as direct carrier for ^{222}Rn is too slow to manage geologically important distances. Nevertheless, it can be responsible for the supply of parent nuclides. A shallow salt dome influences groundwater transport. The water motion is driven by density gradients due to salinity and thermal effects of the salt (Evans and Nunn, 1989; Magri et al., 2009). Magri et al. (2005) modeled the groundwater behaviour east of the Bad Segeberg salt diapir in the south of the Warder research area. Their study revealed interplay between thermohaline convection and saline brine flow. Salty waters form in 4 km depth and rise up to the surface by thermal buoyant forces. Jensen (1983) described high temperatures above salt domes as a result of enhanced heat flow due to the thermal conductivity of salt and surface layers of low conductivity. This implies a possible upward motion of deeper fluids due to convection (Khutorskoi et al., 2009; Nagihara et al., 1992). Fresh water can enter through the same pathways that account for the partial dissolution of the salt dome margins which give rise to density driven thermohaline convection.

Provided that vertical consistent permeability conditions prevail, the particular conditions adjacent to a salt dome support the rise of deep salty water with high ^{226}Ra contents and thus the transport of parent nuclides to the surface. ^{226}Ra can adsorb on the surface of precipitated Fe- and Mn-oxides and -hydroxides, organic materials and clay minerals, promoting a potential ^{222}Rn in soil gas source. A similar process is described in Surbeck (2005). The surface soil cover in the research areas complies with the conditions for ^{226}Ra accumulation. In the Siek research area the traverses are located in podzolic soil. Podzol is characterised by leaching of Fe- and Mn-oxides (sesquioxides) from the surface soil and their accumulation in the subsoil. Thus the chemical preconditions for ^{226}Ra adsorption do exist. The pseudogley cover in the Warder research area is characterised by alternating reducing and oxidizing conditions. Under oxidizing conditions the sesquioxides tend to precipitate. The fissured morphology above the salt structure provides pathways for outgassing. Enhanced degassing over salt domes was reported by McGinnis et al. (2011) and Taylor et al. (2000). The Quaternary sediments in the research areas are boulder materials constituted of sands, clays and boulder, thus providing clay minerals as potential adsorbers of ^{226}Ra. Likewise the deeper Tertiary deposits are composed of alternating sands and clays. As the measured variations are not caused by exogene factors and petrophysical soil parameters investigated here, the emphasis should be placed on the conditions implied by the halokinetic environment.

5.6 Conclusions

In Schleswig-Holstein we investigated the ^{222}Rn in soil gas activity above the margin of the Siek and Segeberg salt diapirs. The results of our work unequivocally show that the salt structure margins are characterised by zones of elevated ^{222}Rn activity in soil gas. The position of these zones of elevated concentrations could be approved by repeated measurements. Nonetheless, the elevated ^{222}Rn activities vary with time. This phenomenon was observed in the soil gas ^{222}Rn activity across faults in the Cantabrian Mountains, northern Spain (Künze et al., 2012). The here presented data were acquired in a narrow time frame and the variations in ^{222}Rn concentration are not caused by moisture content of the soil, as there is no evident correlation. Supplementary to the so far recognised correlation between radionuclide rich Weichselian boulder deposits and elevated ^{222}Rn in soil gas activity, this work gives a first approach to the structural influence of an active halokinetic salt diapir environment that must be taken into account. In summary, the assumed geological facts given in the research area alone and interplay of these possibly provide appropriate conditions for elevated ^{222}Rn activities in soil gas generated by salt movements:

- The permeability required for advective ^{222}Rn migration is given by faults created by the rising diapir and eventually the poorly sorted glacial boulder deposits (despite impermeable clay horizons).
- Rising salt contributes to the breakup of rock components in the pierced and deformed deposits adjacent to the margins of the diapirs, thus increasing the emanation power.
- Enhanced outgassing above salt structures has been monitored.

- Dilution of salt by infiltration of fresh water increases the salinity of the groundwater and hence leads to a density driven thermohaline convection, bringing warm deep salty water to the surface with generally higher content in ^{226}Ra.
- ^{226}Ra supplied by this processes is adsorbed by sesquioxides, clay minerals and organic material, providing a source for ^{222}Rn release.
- Microbubble transport through faults from deep sources or shallower realms provides a possibility for an efficient migration of ^{226}Ra and ^{222}Rn.

More information about ^{222}Rn behaviour in a salt dome environment would deliver the determination of ^{226}Ra concentration in soil. To ensure the halokinetic contribution to the ^{222}Rn in soil gas activity measured in Schleswig-Holstein, the correlation of ^{222}Rn with CO_2 should be investigated.

6 Introduction into the behaviour of Ra in the environment

Ra is a member of the ^{238}U-decay series. In nature four Ra isotopes are found, all of which are radioactive (Table 6.1). ^{226}Ra is the most important isotope of these regarding the ubiquity of ^{238}U in the environment, the long half life of 1600 years and the decay into ^{222}Rn (Smith and Amonette, 2006). About 30 years after the discovery of Ra in 1898 by Marie and Pierre Curie, its toxicity for humans was realized. In the 1950´s it was initially identified as pollutant for the environment (IAEA, 2010). Ra belongs to the group of alkaline earth metals and its behaviour is very similar to Ba (Kozak et al., 2005; Langmuir and Riese, 1985; Vandenhove et al., 2010). In the human body Ra acts as a Ca analogue and thus affects the bone tissue.

Table 6.1: Basic data of four natural occurring Ra isotopes (Smith and Amonette, 2006).

Isotope	Half life	Primary decay mode	Decay Series
^{228}Ra	5.75 years	ß	^{232}Th
^{226}Ra	1600 years	α,γ	^{238}U
^{224}Ra	3.66 days	α,γ	^{232}Th
^{223}Ra	11.44 days	α,γ	^{235}U

The determination of radionuclide concentrations in the environment became increasingly important in the context of nuclear waste deposition. The determination of Ra is of special interest as its occurrence can be used as indicator of environmental radioactive contamination (Akyil et al., 2002). Regions with elevated concentrations of radionuclides imply a higher risk for their ingestion as they may enter into the food chain (Iyengar, 1990). Ra belongs to the “natural occurring radioactive materials” termed as NORM (IAEA, 2010). Increased concentrations of Ra may be a result of the natural abundance of parent nuclides in the geological environment or the enrichment or translocation by chemical or physical processes. Ra is a byproduct of uranium mining and -milling, underground mining of raw materials (e.g. coal, heavy sands, gold), phosphate fertilizer production and oil and gas exploitation (IAEA, 2010). The investigation of the occurrence and the behaviour of Ra and radionuclides in general revealed their usefulness and potential for scientific applications such as dating methods. Additionally, their function as natural geochemical tracers for geochemical processes, dynamics in aqueous systems and the possibility of risk estimation for radioactive wastes as well as the identification of regions with higher risk of Ra occurrence (IAEA, 2010) make them interesting candidates for geochemical investigations.

The primary sources of ^{226}Ra are U- and Th-bearing minerals in the earth´s crust (Jaworowski, 1990). ^{226}Ra is continuously formed from the decay of its parents (Molinari and Snodgrass, 1990). The distribution of the parent nuclides therefore reflects the distribution of ^{226}Ra, though deviations of the secular equilibrium must be taken into account regarding the different chemical behaviour of ^{226}Ra and its parents (Molinari and Snodgrass, 1990).

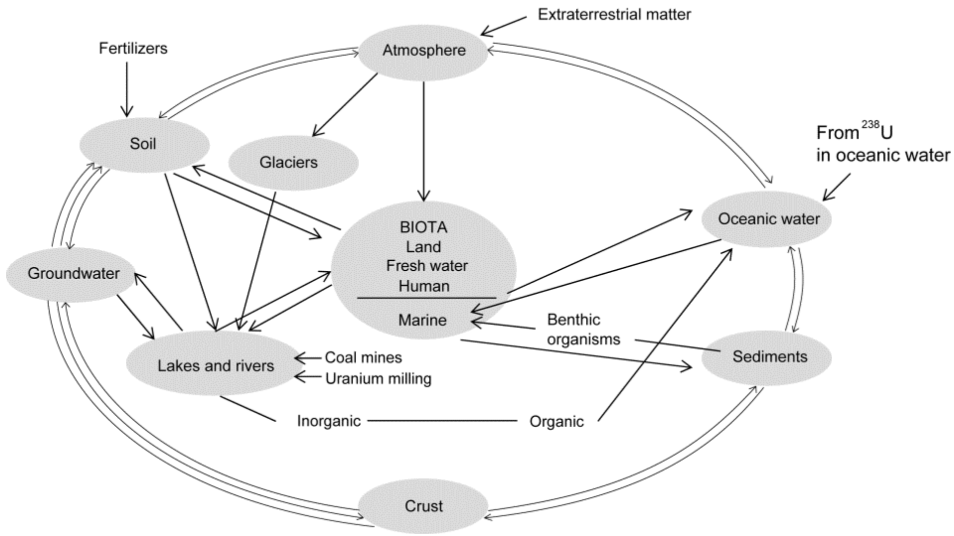

Fig. 6.1: Global cycle of ^{226}Ra, adopted from Jaworowski (1990).

Fig. 6.1 represents the global cycle of ^{226}Ra in the environment. The concentration of ^{226}Ra in crustal rocks depends on the occurrence of U- and Th-enriched minerals. From the crust ^{226}Ra may reach soil, sediments and groundwater. The transition of ^{226}Ra from the crust to sediments and soil occurs via weathering, erosion and subsequent soil or sediment formation. Enrichment of groundwater in ^{226}Ra occurs due to different processes as desorption, exchange, rock dissolution or leaching (Dragović et al., 2012). The damage caused by the recoil effect of an atom when it decays emitting a α-particle generally results in an increase of mobility of daughters (Molinari and Snodgrass, 1990). The extent of ^{226}Ra transfer will depend on the type of ^{226}Ra containing mineral, distribution of ^{226}Ra within the mineral grains, the size of the grains, the frequency of fractures and other parameters affecting the contact area between the groundwater and the mineral grains. Likewise, the occurrence of ^{226}Ra in water is dependent on the concentration and distribution (i.e. location) of parent nuclides in the rock, the solubility of the parent nuclides and the solubility of the radionuclide itself. The occurrence is further controlled by the rate of geochemical reactions that control the mobility of the radionuclide relative to the release of the nuclide by weathering, leaching and recoil processes and the residence time of the radionuclide in water (Szabo et al., 2012). However, it must be considered that rock complexes of same geotectonic units can differ in their ^{226}Ra concentrations (Dragović et al., 2012).

The separation of ^{226}Ra from its parents in rocks is evident from elevated concentrations of ^{226}Ra daughters in microfractures and along grain boundaries of low ^{226}Ra containing rocks

(Molinari and Snodgrass, 1990). According to Dickson (1990) highly saline waters, i.e. at high ionic strength, frequently contain high concentrations of ^{226}Ra without having been in contact with U-enriched rocks. The results of several investigations summarised by Dickson (1990) show that the concentration of ^{226}Ra in solution is related to groundwater chemistry rather than to the concentration in host rocks. Elevated ^{226}Ra concentrations in water at high ionic strength have been reported in e.g. Ames et al. (1983b), Dragović et al. (2012) and Nathwani and Phillips (1979).

Together with Ba, Ra is the unique divalent cation, which is not redox sensible (Kozak et al., 2003) while its parent U is subjected to weathering under oxidizing conditions, e.g. in near surface groundwater, leading to an elevated disposability of Ra. Hence, Ra accumulation near the surface may occur due to the co-precipitation of Ra adsorbed onto Fe- and Mn-oxyhydroxides as well as Ca and Mg carbonates that form due to CO_2 loss when water reaches atmospheric pressure conditions (Molinari and Snodgrass, 1990). Related to ^{222}Rn in soil gas occurrence, transport of ^{226}Ra with groundwater or soil gas has been proposed by Keller et al. (1992). The theory of geogas upflow (Etiope, 1998; Etiope and Martinelli, 2002; Kristiansson and Malmqvist, 1982) provides a mechanism for fast transport of trace elements attached to or caught in bubbles, that rise through water filled fractures. The authors assumed that the fault gouge is the source material. Migration of Ra in soil (porous media) has been controversially discussed by Frissel and Köster (1990) and is of special interest regarding nuclear waste deposition. These authors concluded that Ra does not migrate through soil, except for dispersed or dissolved Ra (Boscov et al., 2001; Frissel and Köster, 1990).

The mechanisms of ^{226}Ra transport in the solute state in a porous medium are advection, molecular dispersion, molecular diffusion and chemical reactions in the solution (Boscov et al., 2001). Generally, in water ^{226}Ra is not in equilibrium with mother nuclides (Dickson, 1990). Within dilute water being in contact with soil the concentration of ^{226}Ra is limited by sorption onto Fe- and Mn-oxyhydroxides and onto clay minerals (Ames et al., 1983a, 1983b; Moore and Reid, 1973; Szabo et al., 2012) as well as co-precipitation reactions with Ba, Sr and Ca sulfates (barite, celestite and gypsum respectively) (Molinari and Snodgrass, 1990; Vandenhove et al., 2010). In aqueous solution ^{226}Ra is the smallest hydrated ion compared to Ca and Mg. This implies a high ionic radius and accordingly a high selectivity for ^{226}Ra by ion exchange substrates like clay minerals and organic matter (Rachkova et al., 2010; Vandenhove et al., 2010). According to Rachkova et al. (2010) sorption with Fe- hydroxides and co-precipitation with ions of alkaline earth elements are most important for fixation of Ra in soils. General factors that influence the sorption of materials are summarised in Smith and Amonette (2006). As a result, dissolution of Fe- and Mn-oxyhydroxides releases ^{226}Ra to the water. Sorption and desorption studies reported in Smith and Amonette (2006) and USEPA (2004) imply that ^{226}Ra

sorption is completely reversible. The mobility of ^{226}Ra in water increases with increasing ionic strength due to the competitive exchange with similar ions.

The measurement of ^{226}Ra in environmental samples is complicated by the co-precipitation with other members of the alkaline earth metal group. Precipitation is the dominant process in waters containing high sulfate concentrations and may distort the measurement of adsorption quantities as well as the amount of dissolved ^{226}Ra.

In summary, the mobility of Ra in solution is directly influenced by sorption, desorption and exchange processes as well as co-precipitation and dissolution/leaching (Molinari and Snodgrass, 1990; Szabo et al., 2012). As stated above, the degree of fractures influences the Ra concentrations in groundwater. Water with high Ra activity may thus indicate fractured or brecciated rocks with a high surface to volume ratio, though conversely, a fracture zone containing water enriched in Ra may be acting as a conduit to bring such water from a depth to surface.

7 ^{226}Ra and ^{222}Rn in soil concentrations: trends across different geological structures in northern Spain and northern Germany

Manuscript in preparation

Abstract:

^{226}Ra and ^{222}Rn in soil and in soil gas, respectively, were measured across the Sabero-Gordón Fault in northern Spain and across the Bad Segeberg-Sülberg salt structure in northern Germany. Previously, no seismic activity has been reported related to the Sabero-Gordón Fault. Nonetheless, ^{222}Rn in soil gas surveys revealed elevated concentrations and ranges between 20 and 200 kBq/m^3 (autumn measurement program). The elevated values are assumed to be induced by the presence of aseismic fault slip that results from the recurrence of changes in the stress field. Previously, different studies have reported the current uplift of the Bad Segeberg-Sülberg salt structure. The ^{222}Rn concentration was shown to be elevated across a salt intruded fault and varies between 10 and 100 kBq/m^3. We surveyed daughter and mother nuclide activity trends in both research areas aiming to separate the geochemically induced ^{222}Rn signal from the structural component of the soil gas signal. Additionally, the diffusive ^{222}Rn component was calculated using the ^{226}Ra activity value and petrophysical soil parameters. The comparison of ^{222}Rn in soil gas concentrations with the ^{226}Ra in soil activities is not clear-cut and both correlated trends and non-correlated trends are observed.

7.1 Introduction

In a closed system, the ^{226}Ra activity concentration in soil should highly correlate with ^{222}Rn activity in soil gas (Molinari and Snodgrass, 1990). The natural environment is an open system, and hence the direct positive correlation between mother and daughter nuclides is complicated by migration processes (Etiope and Martinelli, 2002; Kemski, 1993). In this study we compare lateral distribution trends of ^{226}Ra in soil with ^{222}Rn in soil gas across geological subsurface structures. ^{222}Rn in soil gas is generated by α-recoil of ^{226}Ra located in mineral grains or in secondary coats on the surface of soil components. Generally, elevated ^{222}Rn concentrations in soil gas are found near rocks rich in U and Ra, e.g. acidic crystalline rocks, black shales (Swakón et al., 2004) or in the vicinity of faults or fissured rocks (Kemski et al., 1992; Kristiansson and Malmqvist, 1982). Once having reached the pore space ^{222}Rn is able to migrate by diffusive and advective processes through soil pores or structural pathways, thus moving away from its source and inducing deviations of the secular equilibrium. ^{222}Rn is soluble in water, thus transport by groundwater is a further migration process. ^{222}Rn measurements are frequently applied in geodynamic contexts as ^{222}Rn serves as geophysical tracer for locating active and potentially active faults (e.g. Ciotoli et al., 1999; Etiope and Lombardi, 1995;

González-Díez et al., 2009; Ioannides et al., 2003; King et al., 1996; Lombardi and Voltattorni, 2010; Tanner, 1964, 1980). Active fault movements contribute to enhanced emanation of ^{222}Rn as the grain size of rocks and soil components will reduce due to the formation of microcracks (Igarashi et al., 1995; Torgersen et al., 1990). Holub and Brady (1981) reported significant changes in ^{222}Rn emanated from a rock volume induced by small changes in applied stresses. A ^{222}Rn signal measured in soil is composed of an autochthonous component which reaches the pore space by diffusive processes induced by ^{226}Ra located within the recoil range and possibly of an allochthonous component which includes ^{222}Rn generated away from the sampling point and having migrated by advective processes. Advection requires pathways such as faults, joints and fissures (Kemski et al., 1992) and a certain amount of gas to be sensitive to pressure gradients (Etiope and Martinelli, 2002). In the field of fault detection by ^{222}Rn measurements, the zones of elevated values visually form peaks in the graphs often designated as ^{222}Rn anomalies. Nevertheless, these zones of elevated values may be the result of radionuclide accumulation adjacent to the sampling point and thus displaying a geochemical signal. In order to ensure that high levels of ^{222}Rn are the result of geological structures it is important to probe the distribution of its parent nuclides at particular sampling points. Further, careful analysis of the components that contribute to a measured signal is needed to differentiate between them. Thus, the determination of the direct parent ^{226}Ra in the soil surrounding soil gas sampling points is useful as diffusively formed ^{222}Rn in soil gas can be estimated knowing the activity concentration of its parent nuclide and soil parameters. Determination of ^{238}U in soil allows the determination of ^{226}Ra activity through the assumption of a secular equilibrium. However, it has been shown that in an open system Ra may be separated by different processes from its parent (e.g. Nazaroff, 1992). Unfortunately, data of radionuclide or ^{226}Ra content of the probed soil is lacking in many cases. Thus, usually one works with calculated backgrounds resulting from typical ^{222}Rn activities for the particular soils in order to define zones of elevated concentrations (e.g. King et al., 1996). Another approach is to combine ^{222}Rn with CO_2 and CH_4 as well as He measurements. CO_2 and CH_4 are the preliminary carrier gases for ^{222}Rn and He and allow for a fast migration (Baubron et al., 2002; Ciotoli et al., 1999; Etiope and Lombardi, 1995; Guerra and Lombardi, 2001). In case of positive correlation between ^{222}Rn activities in soil gas and the presence of carrier gases, the existence of ^{222}Rn signals due to geodynamic processes is most likely, because advective transport by carrier gases requires pathways which are supposed to be promoted by active faults.

According to Kemski (1993) and Kemski et al. (1992) the subtraction of the local (diffusive) ^{222}Rn signal from the measured one results in the advective signal which is structurally implied. Nonetheless, several publications on fault localization by ^{222}Rn measurements also associated enhanced ^{222}Rn signals with elevated ^{226}Ra concentrations of fault zones (e.g. Clamp and Pritchard, 1998; Koike et al., 2009).

In the past two years we investigated ^{222}Rn in soil gas in two geological very distinct areas, one of which is based in northern Spain (Künze et al., 2012) and the other in northern Germany (Chapter 5). In Spain we detected elevated ^{222}Rn concentrations (up to 200 kBq/m^3, autumn measurement program) across the Sabero-Gordón Fault, a Variscan fault, which was reactivated during the Alpidic Orogeny. No seismicity has been reported from this fault and the geochemical activity coinciding with the fault outcrop indicates an aseismic fault slip under the present stress regime. In northern Germany the subsurface is characterised by active salt structures provoking faults in the sedimentary cover. Elevated ^{222}Rn concentrations were shown to prevail across the salt structure margin indicating geochemical activity. Local ^{222}Rn concentrations in soil gas reached levels of up to 100 kBq/m^3. Subsurface salt structures have an impact on groundwater, thus influencing the behaviour of migration processes. In this context the ^{226}Ra migration is of interest, due to the short half life time of ^{222}Rn and the longer disposability of ^{226}Ra within the system. In this paper we first report measurements of ^{226}Ra and ^{222}Rn in traverses crossing geological subsurface structures, and secondly, compare the trends. The possible mechanisms leading to fault-related ^{226}Ra occurrence and the validity of structural ^{222}Rn signal determination by geochemical thresholds are discussed.

7.2 Material and Methods

7.2.1 Sampling Locations

The research areas are close Veneros, near Boñar in the southern Cantabrian Mountains, northern Spain and close to Warder in Schleswig-Holstein, northern Germany. The soil samples for the analysis of ^{226}Ra were collected in vicinity of soil gas sampling points for ^{222}Rn analysis. The results of ^{222}Rn analysis of both areas have been published previously in Künze et al. (2012) or are submitted for publication in Künze et al. (see Chapter 5).

<u>Northern Spain</u>

In 2010 ^{222}Rn in soil gas was measured across the Sabero-Gordón Fault (SGF) near Boñar in the southern Cantabrian Mountains, NW Spain. The soil samples investigated in the present work were collected along two parallel traverses ("SG" and "S4" in Künze et al., 2012) that cross the SGF. The soil cover is classified as Alfisol which is characterised by argillaceous accumulation horizons (http://sig.marm.es/siga/). Details of sampling points are given in Künze et al. (2012).

<u>Schleswig-Holstein, northern Germany</u>

In 2011 we collected ^{222}Rn in soil gas samples in Warder near Bad Segeberg, Schleswig-Holstein, in order to assess the possible contribution of a salt dome environment on the ^{222}Rn in soil gas signal (Chapter 5). The research area "Warder" was chosen after examination of data published in

"Geotektonischer Atlas von Nordwestdeutschland und dem deutschen Nordsee-Sektor" (Baldschuhn et al., 2001). The Warder research area crosses the margin of the Bad Segeberg-Sülberg salt structure that reaches the surface in Bad Segeberg and is related to a normal fault in the area under investigation. In proximity to the village Warder, a traverse extending about 580 m in NW-SE direction was sampled (WS_2, Chapter 5.2.4). The soil is classified as pseudogley consisting of boulder clay and boulder sand of the Weichsel glacier (BGR, 2007). 28 soil samples were collected along with soil gas samples for ^{222}Rn detection. Details of the geographical and geological situation as well as the sampling points are given in Chapter 5.2.4.

7.2.2 Samples

Soil gas for ^{222}Rn determination and soil samples for petrophysical parameter and ^{226}Ra activity determination were collected. The soil gas was extracted from a depth of 1 m by a syringe through a drill rod and directly pumped into the Lucas cell, which was evacuated prior to sampling. The soil samples were taken in the vicinity of the soil-gas sampling points from a depth of 1 m using a stainless steel sampling tube. The lower part of the core (10 cm) selected for analysis was placed in a plastic bag and hermetically closed in order to minimize the effect of evaporation during the transport to the laboratory.

7.2.3 Analytical procedure

Petrophysical soil parameters

The water content was determined by drying the soil samples in an oven at T = 105 °C until a constant weight was reached. The wet bulk density was estimated by weighing 8 cm^3 of undisturbed soil core. The grain density was measured by kerosene-pycnometry. Approximately 7 g of the sample were placed into the pycnometer which was subsequently filled with kerosene while continuously removing the air by a vacuum pump. The rock sample volume was calculated as the difference between the volume of kerosene in the pycnometer with and without the rock material. A detailed description of this method was given by Koroleva et al. (2011). The dry bulk density was calculated using measured bulk wet densities and natural moisture contents. From the obtained values the physical porosity was calculated.

^{222}Rn in soil gas

Levels of ^{222}Rn in soil gas were measured using Lucas cells and a SISIE device. The measurement of ^{222}Rn is based on the interaction of ionizing radiation with matter. The inside wall of the Lucas cell is coated with silver activated zinc sulfide (ZnS(Ag)), except one end which is covered with a transparent window for coupling to a photomultiplier tube. When a α-particle strikes the wall of the cell, a flash of light is emitted from the coating. The light is detected in SISIE by the photomultiplier tube and translated into an electrical signal. The Lucas cell with gas sample was placed into SISIE after a period of 3 to 24 hours, when ^{222}Rn and its progenies are in radioactive equilibrium.

<u>^{226}Ra in soil samples</u>

Measurement of ^{226}Ra activity of the soil samples was performed using a α-spectrometer. Before α-spectrometric measurements are performed a chemical manipulation is required to obtain α-radiating sources with the desired radiochemical purity. ^{226}Ra was chemically separated from the soil samples according to a (α-spectrometric) method described by Bodrogi et al. (2005) and Morvan et al. (2001). This preparation method is based on the adsorption of ^{226}Ra from a solution on MnO_2-coated discs (Eikenberg et al., 2001; Surbeck, 2000). The method was successfully applied for ^{226}Ra determination in aqueous samples (Bodrogi et al., 2005; Eikenberg et al., 2001; Morvan et al., 2001; Surbeck, 2000). We applied this approach for soil samples.

The amount of soil material varied between approx. 20 g and 60 g. The samples were leached with 3 M HNO_3 at a solid:liquid ratio of 1:2 over 2 hours. Then the extracted solution was filtered and dried. Subsequently, the obtained sediment was dissolved with distilled water. The pH of the obtained solution was adjusted by adding NaOH solution in order to ensure neutral pH conditions. Eikenberg et al. (2001) investigated the effect of pH value on ^{226}Ra sorption. These authors demonstrated that at neutral pH ^{226}Ra sorbs efficiently onto MnO_2 discs. ^{226}Ra in the soil samples was allowed to adsorb onto MnO_2-coated discs by immersing the discs in the obtained solution. Under stirring at room temperature the adsorption time was between 18 and 48 hours. The MnO_2-coated discs were prepared as follows: discs of 20 mm in diameter were stamped from a 1 mm thick polyamide plate (PA6.6). The discs were first cleaned with ethanol and deionized water, and subsequently immersed in $KMnO_4$ solution (12.5 g/l) at 70°C for 2 h in a dark room which results in coating of the disc with a thin MnO_2-layer (Eikenberg et al., 2001; Surbeck, 2000). The chemical recovery of ^{226}Ra was estimated using a correction factor which was determined using a reference ^{226}Ra solution (activity = 0.2 kBq) which was adsorbed under equal conditions onto MnO_2 discs. The correction factor depends on the adsorption time of ^{226}Ra onto MnO_2 discs. Empirical tests were carried out in order to assess the time dependence. It was shown that for adsorption times longer than 18 hours changes of the correction factor only have a negligible impact. Determination of the correction factor resulted in 10.7 for 18 to 48 h (arithmetic mean value from threefold measurements). The MnO_2 discs with adsorbed ^{226}Ra were measured with a α-spectrometer.

<u>Test of ^{226}Ra recovery</u>

As stated above, the MnO_2 adsorption method was successfully applied to water samples. In comparison to water samples the leached soil samples contain higher oxide concentrations which can trap ^{226}Ra from solution. Therefore a test was carried out in order to probe the influence of these oxides. During the leaching procedure of a natural soil sample, the ^{226}Ra reference solution with an activity of 0.2 kBq was added. Afterwards, the sample was prepared and measured according to the protocol described above. From these results it is evident that the difference between the natural ^{226}Ra concentration in the soil sample (measured previously) and the soil sample with added reference solution is 0.18 ± 0.017 kBq, i.e. approx. 90%. However, soil samples are homogeneous throughout the particular profiles; therefore the error should be constant for the investigated samples allowing for a comparison amongst them. The results confirm that the presence of oxides in the solution has no significant influence on the adsorption of ^{226}Ra onto MnO_2 discs regarding the soils under investigation.

7.3 Results and discussion

The grain and bulk dry density of the investigated samples is in the range of 2.59 to 2.81 g/cm^3 and 1.4 to 2.4 g/cm^3, respectively (Table 7.1). The calculated physical porosity ranges from 10 to 49 vol%. It should be noted that if no grain density measurement was performed we assumed it to be 2.70 g/cm^3 (italic letters Table 7.1). The activity values of ^{222}Rn in soil gas vary between 22 and 202 kBq/m^3 in northern Spain, and lie in between 12 and 99 kBq/m^3 in northern Germany (Table 7.1). For the ^{226}Ra content we found activities in the range of 2 and 14 Bq/kg in northern Spain and 1 to 5 Bq/kg in northern Germany (Table 7.1). The resulting profiles across the investigated structures are presented in Fig. 7.1 a–c.

As reported by various authors, petrophysical soil parameters influence the emanation and migration of ^{222}Rn in soil. Various approaches interrelate the ^{222}Rn activities in soil gas to ^{226}Ra activities in soil. Jönsson et al. (1999) calculated the potential ^{222}Rn level in soil gas based on the phenomenological assumption that 1 Bq/kg Ra corresponds to 1700 Bq/m^3 of ^{222}Rn in soil gas. The reported experimental ^{222}Rn concentrations in soils of different regions are significantly lower than the calculated ones. The authors suggest applying a correction factor for each sample because petrophysical factors influence the relationship. An approach including *in situ* petrophysical soil parameters is given in Ciotoli et al. (1999), Gast and Stolz (1982), Keller et al. (1992) and Kemski (1993); the diffusive ^{222}Rn activity may be calculated with the formula:

$$A_{Rn} = \frac{A_{Ra} \cdot E \cdot \rho}{\phi} \tag{1}$$

with A_{Rn}= activity concentration of ^{222}Rn in soil gas (= diffusive component); A_{Ra} = activity concentration of ^{226}Ra; E = emanation coefficient; ρ = bulk dry density and ϕ = specific porosity. According to Gómez-Escobar et al. (1999) the emanation coefficient for solid grains is 0.25 but may vary between 0.02 and 0.5 (Nazaroff, 1992). As there is no protocol for the determination of the emanation coefficient for the soils investigated in the research areas, the ^{222}Rn diffusive component was calculated with by assuming E = 0.25. The results of the measurements and calculations are presented in Table 7.1.

Table 7.1: Results of the measurements and calculations.

Name	^{226}Ra in soil (Bq/kg)	^{222}Rn in soil gas (kBq/m^3)*	Grain dens. (g/cm^3)	Dry bulk dens. (g/cm^3)	Phys. por (vol%)	^{222}Rn $_{calc}$ (kBq/m^3)
sampling traverses northern Spain						
Sg1	1.6	28	2.66	2.3	15.3	6
Sg2	1.6	22	2.65	1.9	29.5	2
Sg4	12.0	77	2.70	2.3	13.0	54
Sg6	13.7	87	2.64	2.3	11.5	69
Sg7	4.9	51	2.68	2.2	17.3	16
S4-1	3.9	115	2.69	2.2	18.7	11
S4-2	10.2	202	2.69	2.4	10.1	61
S4-3	3.2	78	2.68	2.4	12.2	15
S4-4	3.1	88	2.77	2.3	16.4	11
S4-5	1.8	94	2.68	2.1	23.5	4
S4-6	2.9	79	2.81	2.4	15.4	11
S4-7	5.8	79	2.61	2.2	14.6	22
S4-8	7.7	32	2.66	2.2	15.9	27
S4-9	2.0	78	2.63	2.4	9.7	12
S4-10	3.4	34	2.59	2.3	10.8	18
sampling traverse northern Germany						
WS_2-1	1.6	17	-	2.1	*23*	4
WS_2-2	3.5	63	-	2.2	*17*	11
WS_2-3	1.8	28	-	2.2	*20*	5
WS_2-4	3.2	64	-	2.0	*26*	6
WS_2-5	3.0	22	-	2.3	*16*	11
WS_2-6	1.9	29	-	1.9	*30*	3
WS_2-7	1.2	36	-	1.7	*37*	1
WS_2-8	4.7	20	-	2.0	*26*	9
WS_2-9	1.0	29	-	1.4	*49*	1
WS_2-10	1.4	36	-	2.2	*17*	5
WS_2-11	3.6	99	-	2.0	*24*	7
WS_2-12	2.5	23	-	2.0	*27*	5
WS_2-13	1.4	12	-	1.5	*43*	1
WS_2-14	1.8	20	-	2.0	*26*	3
WS_2-15	1.6	63	-	2.0	*26*	3
WS_2-16	1.5	41	-	2.1	*22*	4
WS_2-17	1.7	35	-	1.8	*35*	2
WS_2-18	1.2	54	-	1.7	*37*	1
WS_2-19	1.3	22	-	2.1	*23*	3
WS_2-20	1.8	16	-	1.6	*40*	2
WS_2-21	1.1	34	-	1.7	*38*	1
WS_2-22	1.8	38	-	1.6	*41*	2
WS_2-23	1.9	39	-	2.2	*18*	6
WS_2-24	1.0	62	-	2.2	*19*	3
WS_2-25	1.4	26	-	1.9	*31*	2
S_2-26	1.4	46	-	2.0	*25*	3
WS_2-27	1.2	13	-	1.8	*32*	2
WS_2-28	1.6	31	-	2.0	*26*	3

*positive relative standard deviation is about 20-30% for 1-20 kBq/m^3; 10-20% for 20-40 kBq/m^3 and ≤10% for results > 40 kBq/m^3

In the present study we focus on the activity of each sample relative to the other samples. Calculated ^{222}Rn activity values are lower than the measured ones (Table 7.1). This could be explained by

a) high uncertainty of the α-spectrometric measurement. As mentioned above, the radiochemical yield of tracer ^{226}Ra is approximately 90%.
b) in an open system additional ^{222}Rn sources cannot be excluded.

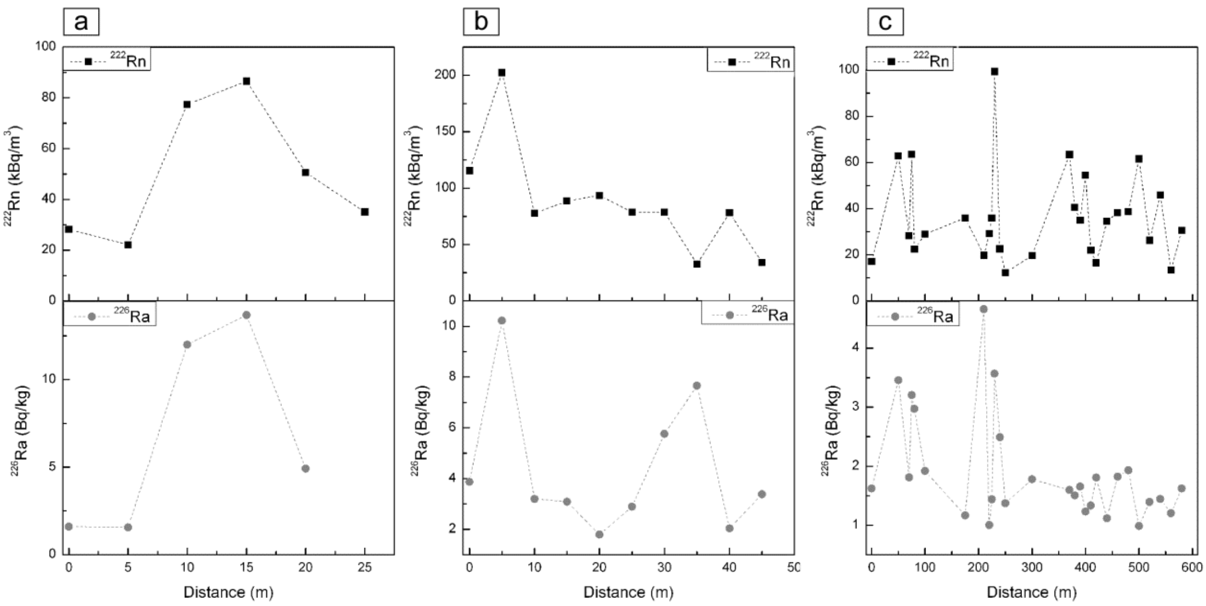

Fig. 7.1: (a) ^{222}Rn in soil gas and ^{226}Ra in soil concentrations along the traverse "SG", crossing the SGF; (b) ^{222}Rn in soil gas and ^{226}Ra in soil concentrations along the traverse "S4" crossing the SGF; (c) ^{222}Rn in soil gas and ^{226}Ra in soil concentration along the traverse "WS_2" that crosses the margin of the Segeberg-Sülberg salt structure.

Northern Spain:

The trend of the ^{222}Rn in soil gas signal (kBq/m^3) and ^{226}Ra (Bq/kg) in soil shows a good correlation along the traverse "SG". The increase in ^{222}Rn concentration corresponds to an even stronger increase of ^{226}Ra activity in soil. Analogously, the decrease in ^{222}Rn concentration is accompanied by a decrease of radionuclide activity in soil (Fig. 7.1a). Likewise, the activity concentrations of ^{222}Rn in soil gas and ^{226}Ra in soil seem to behave similarly in the first 10 m along the traverse "S4" (Fig. 7.1b). This first peak (0–10 m distance) is followed by relatively uniform ^{222}Rn activities up to the 30 m distance. This trend is not reflected by ^{226}Ra activity of the soil. The ^{226}Ra activity concentration has a minimum at a distance of 20 m and shows a renewed strong increase before reaching the 35 m distance, which coincides with a minimum in ^{222}Rn concentration in soil. Despite the correlation found for the first 3 samples, comparison of ^{222}Rn in soil gas and ^{226}Ra in soil rather displays an uncorrelated behaviour along traverse "S4".

Schleswig-Holstein, northern Germany:

The trends displayed by the ^{222}Rn in soil gas signal measured in the Warder research area are shown in Fig. 7.1c. The first zone of elevated ^{222}Rn in soil gas signal between 0 and 75 m correlates satisfyingly well with the results of the ^{226}Ra in soil concentrations. At a distance of about 175 m along the traverse, the ^{226}Ra signal shows a minimum. This is not displayed by the ^{222}Rn in soil gas signal. However, the maximum value at about 230 m is supported by a sharp increase of ^{226}Ra activity in soil, which reveals a twin peak feature not displayed by ^{222}Rn in soil gas concentration. From 300 m to the end of the traverse both signals are again uncorrelated.

In summary the results shown in Fig. 7.1 reveal somewhat ambiguous trends: similar trends of ^{222}Rn in soil gas concentration and ^{226}Ra activity in soil on one hand (e.g. “SG”,Fig. 7.1a; 0–10m of profile “S4”, Fig. 7.1b and 0–200 m of profile “WS_2”, Fig. 7.1c) and uncorrelated trends on the other hand (e.g. 10–45 m of profile “S4”, Fig. 7.1b and 250–580 m of profile “WS_2”, Fig. 7.1c). Fig. 7.2 a–c shows the correlation between $^{222}Rn_{calc}$ and $^{222}Rn_{meas}$. Despite the statistical significant positive correlation of $^{222}Rn_{calc}$ with $^{222}Rn_{meas}$ along the traverse “SG” (r = 0.975; confidence level 95%) there is no significant correlation for the traverses “S4” and “WS_2” (Fig. 7.2).

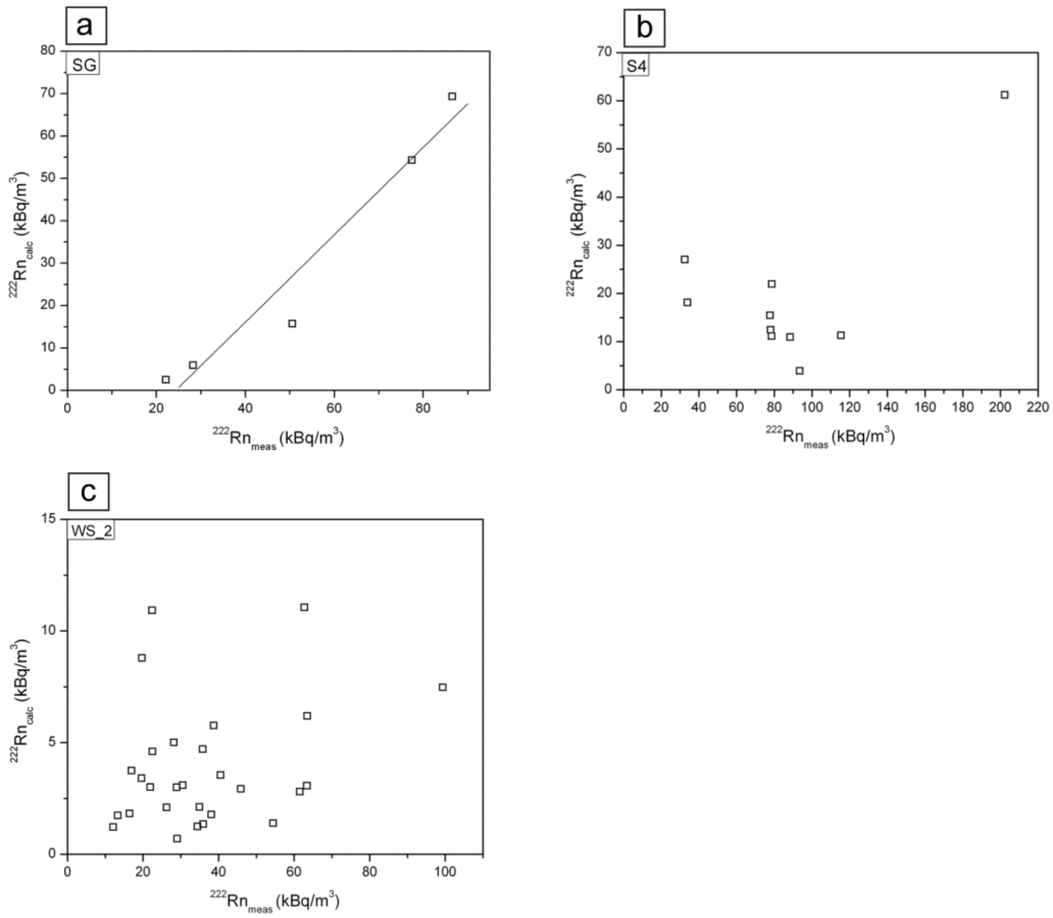

Fig. 7.2: Correlations between $^{222}Rn_{meas}$ and $^{222}Rn_{calc}$;(a) traverse “SG”;(b) traverse “S4”;(c) traverse “WS_2”.

As mentioned above, in the field of research of active fault localization by ^{222}Rn in soil gas measurements, the existence of ^{222}Rn signals related to faults is usually explained by the fact that faults are zones of lowest strength thus providing pathways for enhanced fluid flow allowing ^{222}Rn from deeper strata to reach the surface. The fluid flow may be triggered by changes in the fault´s stress states and fracturing processes related to seismic or aseismic activity. In turn, fracturing processes account for an increase of the inner surface of the present components thus enhancing the

^{226}Ra disposability. According to Toutain and Baubron (1999) geochemical anomalies that correspond to deep gas are termed “direct leak anomalies”. Despite these direct leaks, “secondary anomalies” exist, which are related to the different rocks that constitute the fault (Toutain and Baubron, 1999). In the studies of Kemski (1993) and Kemski et al. (1992) calculated ^{222}Rn concentrations based on radionuclide activity are significantly lower than measured ^{222}Rn concentrations but both show similar trends in selected cases. However, the elevated ^{222}Rn in soil gas signals are interpreted as fault-induced anomalies as they coincide with CO_2 leaks. The presence of a carrier gas and a gas leak does not necessarily account for elevated ^{222}Rn in soil gas concentrations. In the case of active faults gas leaks cater for enhanced transport from deep strata but in the same way the carrier may account for leaching the diffusive ^{222}Rn which is generated in soil. This mechanism could explain the strong ^{226}Ra increase in the second half of profile “S4” which does not correspond to an increase in ^{222}Rn in soil gas concentration. Otherwise, dilution with atmospheric air may steadily alter ^{222}Rn concentrations in soil gas.

The correlation of trends evokes the need for a mechanism explaining the enhanced concentration of radionuclides in fault zones and raises the question if the determination of the diffusive ^{222}Rn component is applicable to define fault-related ^{222}Rn in soil gas anomalies. Authors who detected similar patterns when comparing radionuclide concentrations to ^{222}Rn in soil gas concentrations, favoured a scenario where the close correlation would be unlikely to occur in the case of ^{222}Rn activity due to enhanced flow through the fault (e.g. Clamp and Pritchard, 1998; Koike et al., 2009). Incorporating the fault constituting rocks and soils into the model provides further explanation. Sugisaki et al. (1980) investigated the chemical characteristics of fault gouge and found that fault gases and fault gouges show geochemical anomalies. According to Bottrell (1993) increased ^{222}Rn activity may be due to weathered U-bearing minerals and associated fluids being transported and deposited remote from their source. Clamp and Pritchard (1998) showed enhanced ^{226}Ra activity along the Cronkston Fault in north Derbyshire. U is known to accumulate along structural features when deep waters are carried upwards (Lyle, 2007). Although the mobility of ^{226}Ra is restricted, ^{226}Ra is found in soils derived from low uranium rocks (Tanner, 1986). Processes of soil formation may leave behind materials enriched with residual materials, including radionuclides. Faults may trigger deep waters which are enriched in dissolved ^{226}Ra to migrate upwards. ^{226}Ra may easily adsorb onto the surfaces of minerals, especially clays (Koike et al., 2009). An interesting approach is given by Koike and co-workers (2009) who describe that the parents of ^{222}Rn may accumulate in fault gouges, originating from deep crust carried up by fluids or high pressure gas released during dynamic events. According to these authors, essential requirements for the occurrence of high ^{222}Rn concentrations are the repetition and recentness of fault movements. Regarding the salt structure environment, the flanks of a salt dome (Müller-Hoeppe et al., 2000) or the presence of faults provide pathways for radionuclide transport. Poliakov et al. (1996) have shown that sedimentary rocks above a salt diapir may deform in a brittle as well as viscous way. Possible mechanisms of radionuclide accumulation in faulted zones around a salt structure and possible fast transport mechanisms for ^{222}Rn from deeper strata are presented in Chapter 5.5 The presence of a salt structure influences the temperature, salinity and permeability of its environment. The structural conditions that develop adjacent to salt structures as well as the influence on chemical and physical conditions that is induced by the presence of buried salt deposits may influence the ^{222}Rn activity in soil gas as well as the disposability of its mother nuclide.

7.4 Conclusions

^{226}Ra and ^{222}Rn in soil and soil gas, respectively, were measured in northern Germany and northern Spain. The results obtained from the comparison of ^{226}Ra in soil distributions corresponding to ^{222}Rn in soil gas profiles are less than clear-cut. In one of the investigated profiles that were sampled across the Sabero-Gordón Fault in northern Spain the trends are consistent (profile SG). In a parallel profile (S4) the behaviour of ^{222}Rn and ^{226}Ra is partly similar but shows uncorrelated trends approaching the end of the profile. Likewise, coinciding trends as well as uncorrelated trends are obtained in a profile that crosses the Bad Segeberg-Sülberg salt structure in northern Germany. Fault related elevated ^{222}Rn concentrations in soil gas are usually defined as anomaly, suggesting that faults constitute pathways for enhanced gas migration from deeper strata. The distinction between structurally induced ^{222}Rn signal and the geochemical ^{222}Rn is achieved by the subtraction of the diffusive ^{222}Rn signal which is calculated using ^{226}Ra activity and petrophysical soil parameters. Because the focus of this paper lies on the comparison of trends of mother and daughter nuclides (^{226}Ra-^{222}Rn), the measurements of ^{226}Ra activity were carried out using a α-spectrometer. The partly consistent trends between ^{226}Ra and ^{222}Rn suggest that faults provide likewise suitable conditions for enhanced ^{226}Ra activity. The results of this work indicate that the validity of structural ^{222}Rn signal determination by geochemical thresholds based on ^{226}Ra activity has to be reconsidered.

8 Conclusions and outlook

In this thesis, ^{222}Rn in soil gas surveys were successfully applied to trace subsurface geological structures in unconsolidated sediments. The research areas are located in northern Spain and northern Germany and the measured ^{222}Rn in soil gas activities reach up to 440 kBq/m^3 and 105 kBq/m^3, respectively.

Northern Spain:

In northern Spain, the ^{222}Rn activity in soil gas was investigated during two measurement programs, along with petrophysical parameters in soil samples across the seismically active Ventaniella Fault and the seismically inactive Sabero-Gordón Fault. During the first measurement program (summer) both faults showed elevated ^{222}Rn concentrations in soil gas, whereas the strongly elevated results obtained across the SGF are outstanding. A ^{222}Rn in soil gas map was carried out to separate the zones of elevated concentration from the background values and revealed results comparable with the calculation of background values by statistical methods. In the second measurement program (autumn) we focussed on a detailed investigation by establishing parallel profiles across the SGF, which showed unexpectedly high ^{222}Rn signals compared to the VF according to the data collected in the summer program. The difference of peak values was of factor five between summer and autumn measurement programs. Meteorological influences recorded during the field measurements together with the determination of petrophysical soil parameters are not responsible for this difference in the magnitude of ^{222}Rn activity. A slight shift in the position of the maximum ^{222}Rn concentration indicates that ^{222}Rn measured in the soil gas signal derives from a deeper source. The mechanism proposed is advective transport of ^{222}Rn. Aseismic slip of the SGF under the present stress regime would provide a mechanism for the active formation of pathways, which allows enhanced gas migration. By comparing the results of the measured traverses over both investigated fault segments, it is evident that the magnitude of ^{222}Rn activities in soil gas in these cases does not reveal if a fault´s behaviour is aseismic or seismic.

As no seismic activity has been reported from the SGF, the structural field work carried out in the research area provides an approach to get information on the most recent stress patterns affecting the research area. The results of the quantitative palaeostress analysis based on the theoretical inversion of fault-striae data reveal that the most recent stress orientations (Shmax) recorded in the area of the SGF are N–S and the NW–SE oriented, which would allow reverse as well as dextral strike-slip movement along the weakness zone that provides the fault. Along with the current stress orientations, slip occurring along the Sabero-Gordón Fault is highly probable.

Northern Germany

In Schleswig-Holstein ^{222}Rn in soil gas activity above the margin of the Siek and Segeberg-Sülberg salt diapirs was investigated. The results of this thesis evidently show that the margins of these salt structures are characterised by zones of elevated ^{222}Rn activity in soil gas. So far, elevated ^{222}Rn in soil gas concentrations in northern Germany have been ascribed to radionuclide rich boulder material deposits. However, the reported ^{222}Rn concentrations in the soil gas related to glacial deposits as well as the reference measurements conducted during this thesis are significantly lower than the concentrations measured across the salt structure margins.

The salt structures under investigation are in an active stage, thus moving and causing strain rates that are in the range of strain rates noticeable in ^{222}Rn acitivities. The geological facts related to a salt structure environment and interplay of these provide appropriate conditions for elevated ^{222}Rn in soil gas activities generated due to halokinetic activity. A first theoretical model was developed that summarises the environmental conditions that may have an impact on ^{222}Rn in soil gas activity as well as the distribution of parent nuclides. The permeability required for enhanced ^{222}Rn migration is given by faults associated with the salt structure and by the poorly sorted glacial boulder deposits (despite impermeable clay horizons). The rising diapir may contribute to the breakup of rock components in the pierced and deformed sediments, thus increasing ^{222}Rn release. ^{226}Ra is known to be transported by rising deep salty waters and may adsorb on clay minerals, organic matter and Mn- and Fe-oxyhydroxides, providing an efficient source for ^{222}Rn release. Long distance transport of ^{222}Rn and eventually of ^{226}Ra has been reported by rising microbubbles in waterfilled fractures, thus providing an efficient transport way.

Summary

Zones of elevated ^{222}Rn concentrations in soil gas measured across the SGF as well as the Siek and Segeberg-Sülberg salt structures were found to be consistent in time and space as was approved by repeated measurements. Nonetheless, the values of the elevated ^{222}Rn activities in soil gas vary as well as maximum positions shift slightly. The exogene factors that influence the magnitude of the signal, as temperature, atmospheric pressure and air moisture content, do not show any correlation with the variation of ^{222}Rn in soil gas signals. Likewise, the petrophysical soil parameters determined along with soil gas samplings have no correlatable influence on the measured signal as was reported by other authors.

The investigation of ^{226}Ra concentration in soil brought further insight into the complexity of using ^{222}Rn activity in soil gas to detect active faults. Correlated trends as well as uncorrelated trends of both radionuclides resulted. The correlation of ^{226}Ra and ^{222}Rn in soil gas maxima in the fault zone raises the question if approaches applying geochemical thresholds to separate ^{222}Rn anomalies from local background values yield reliable results. As reported in other publications, even fault zones in unconsolidated sediments provide pathways for fluid migration, which involves the parent nuclide accumulation as well as the enhanced fast long distance migration for ^{222}Rn.

The data collected in this thesis support the successful application of ^{222}Rn measurements to detect different active geological subsurface structures, providing first results regarding the application of the method to identify possible active faults in the Cantabrian Mountains and to trace active salt structures. Certainly, there is a need for more thorough investigations. Nevertheless, ^{222}Rn measurements to trace the margins of active salt structures provide a new approach in the field of soil gas investigations related to active tectonics. Emphasis should be put on ^{222}Rn activity of crustal discontinuities from which no seismic activity has been reported. The structures investigated in this thesis do not directly constitute a hazard to safety and health due to their geodynamic activity, as movements are slow. Nevertheless, they were shown to reveal geochemical activity that may constitute a health risk for the general public under certain circumstances. Detailed monitoring of such structures would help to assess the imposed health risk for dwellings located adjacent to these.

Open questions

During the work on this thesis, new questions emerged which need to be adressed in order to broaden the application field of ^{222}Rn in soil gas measurements and the validity of the measured signals. Further ^{222}Rn surveys above salt structures should be carried out. The soil gas sampling of further faults in the Cantabrian Mountains would complete information about potentially active faults. For the investigated areas long time ^{222}Rn surveys would reveal the seasonal influences on ^{222}Rn in soil gas behaviour. The application of creepmeter surveys would deliver further information about aseismic slip in the SGF area, as well as the movements of faults coupled with salt structures and related ^{222}Rn degassings. Dating of mineral fibres would allow for a chronological order of the stress patterns that resulted from palaeostress analysis in northern Spain. These would thus give insight into the geodynamical history of the Cantabrian Mountains. Several publications reported ^{222}Rn concentrations combined with potential carrier gases such as CO_2 or CH_4, as well as other trace gases such as He. Based on the results obtained during this thesis, a detailed CO_2 survey will be carried out in the Warder research area, in order to find out if a correlation between the two gases can be deduced. The determination of He would provide information about a potential deep source and the continuous monitoring along with ^{222}Rn would provide an approach to determine the contribution of deep gas transfer. CH_4 is known to be released in proximity to crustal discontinuities in active tectonic environments. Carefully interpreted data of positive correlations with other gases would support the suggestion of advective ^{222}Rn migration. In the present thesis it was shown that the application of geochemical thresholds based on the determination of the diffusive ^{222}Rn potential did not reveal clear-cut results. Detailed quantitative analysis of mother nuclides applying mass spectrometric methods and determination of emanation factors of investigated soils in laboratory experiments would provide further insight into the occurrence of both nuclides in fault zones.

Danksagung

An erster Stelle möchte ich Ihnen danken, Herr Prof. Dr. C.-D. Reuther, für die Vergabe dieser Doktorarbeit, für Ihr Vertrauen in das Gelingen und für Ihre kontinuierliche und bereitwillige fachliche Unterstützung. Unsere interessanten Diskussionen haben mich stets weitergebracht, auch in scheinbar aussichtslosen Situationen. Ganz besonders möchte ich mich auch dafür bedanken, dass ich bei der Gestaltung Ihres Buches mitwirken durfte. Ihre Begeisterung für die Geologie hat mich seit dem ersten Semester an der Universität beeindruckt und ich bin sehr dankbar, dass ich in den letzten drei Jahren sowohl im Gelände als auch im Institut daran teilhaben durfte.

Frau Dr. M. Koroleva möchte ich für Ihre Hilfe und Unterstützung während der Anfertigung dieser Dissertation danken. Besonders Ihre Fähigkeit zur Strukturierung der Kapitel und Manuskripte, die im Laufe dieser Arbeit entstanden sind und unsere fachlichen Diskussionen haben mich oft aus der leider so typischen Bäume-und Wald-Situation gerettet.

Ferner möchte ich den Mitarbeitern der Universität Hamburg danken, die zum Gelingen dieser Dissertation beigetragen haben. Herrn Prof. Dr. H. Schleicher möchte ich für das Alphaspektrometer danken, das er uns zur Verfügung gestellt hat. Herrn Dr. S. Lindhorst danke ich herzlich für die Unterstützung im Labor. Frau Thun aus dem geochemischen Labor danke ich für die Dichtebestimmungen. Frau Richarz möchte ich für die gewissenhafte und zügige Anfertigung der so zahlreichen Proben für das Alphaspektrometer danken. Frau Vinx danke ich für die Bereitstellung der verfügbaren Mittel aus dem Labor. Herzlichen Dank an Frau Schütt, für die unkomplizierte Hilfe bei der Beschaffung scheinbar unauffindbarer Literatur!

Jani, Niklas, Kathrin, Philipp, Julio und Sasha - Euch möchte ich für eine unvergessliche Zeit in Lugueros danken. Revival? Ich möchte ferner Niko für die gute Geländezeit danken, die wir zusammen im Kantabrischen Gebirge verbringen durften. Ein großes Dankeschön geht auch an die BSc-Studenten, für die Gelände- und Laborunterstützung!

Sebastian Cäsar möchte ich für die Begleitung durch diese Zeit danken. Ich bin froh, dass wir auch diese Reise durch die Universität gemeinsam mit ähnlichen Sorgen und Herausforderungen und mit gemeinsamen Ablenkungen verbringen konnten!

Danke an meine beiden Berliner Kleinfamilien, für die schönen Wochenenden, die für mich immer eine Reise zum Wesentlichen bedeuteten. Danke, für Eure Unterstützung und für Euer Verständnis. Ich hoffe auf noch viele Wochenenden, ausgedehnte…

Danke an Christina, ich bin so froh, dass wir nach Granada gegangen sind, damit wir uns endlich unterhalten konnten. Danke für das Gefühl, dass es auch so geht.

Ich möchte mich bei Dir bedanken, Lena. Für Deine Freundschaft! Danke, dass Du so viel zugehört hast, dass Du immer da warst. Für das kulinarische Verwöhnen. Für das Wissen um einen schönen Ort mit einem großartigen Menschen!

Tobi, Dr. Krämer. Du weißt, dass ich nie vergessen werde, wie viel Arbeit und Geduld Du in das Lektorat meiner Arbeit gesteckt hast. Danke für Deine so großartige Hilfsbereitschaft!

Und Dir möchte ich danken, Olli. Für das Zuhause-Gefühl, dass Du mir geben konntest, wenn ich nicht dazu in der Lage war. Und für die Ruhe, die ich oft nicht hatte, besonders in den letzten Monaten. Dafür, dass Du an meiner Seite bist.

Das Ende dieser Danksagung möchte ich meinen Eltern widmen. Ohne Euch hätte ich diesen Weg nicht gehen können. Danken möchte ich Euch für so Vieles. Für Euer bedingungsloses Vertrauen in mich und die Dinge, die ich tue. Für alles, was ich von Euch lernen durfte und noch lernen darf. Für Eure Liebe und den Regenbogen.

References

Ahmed Khan, H., 1991. Radon: A friend or a foe? International Journal of Radiation Applications and Instrumentation. Part D. Nuclear Tracks and Radiation Measurements 19, 353-362.

Akyil, S., Aslani, M., Gurboga, G., Aytas, S., Eral, M., 2002. Activity concentration of radium-226 in agricultural soils. J. Rad. Nucl. Chem. 254, 9-14.

Al-Hilal, M., Al-Ali, A., 2010. The role of soil gas radon survey in exploring unknown subsurface faults at Afamia B dam, Syria. Radiat. Meas. 45, 219-224.

Aller, J., Bastida, F., Rodríguez-Fernández, L.R., 2002. Cantabrian Zone: General geological features, in: García Lopez, S., Bastida, F. (Eds.), Palaeozoic conodonts from Northern Spain. Instituto Geológico y Minero de España, Cuadernos del Museo Geominero, Madrid, pp. 3-33.

Alonso, J.L., Heredia, N., Rodríguez-Fernández, L.R., 1990. Memoria, Mapa geológico de España, 1:50 000, Riaño. ITGE, pp. 93-116.

Alonso, J.L., Pulgar, J.A., García-Ramos, J.C., Barba, P., 1996. Tertiary basins and Alpine tectonics in the Cantabrian Mountains (NW Spain), in: Friend, P.F., Dabrio, C.J. (Eds.), Tertiary basins of Spain: the stratigraphical record of crustal kinematics. Cambridge University Press, Cambridge, pp. 214-227.

Alonso, J.L., Pulgar, J.A., Pedreira, D., 2007. El relieve de la Cordillera Cantábrica. Enseñanza de las Ciencias de la Tierra 15, 151-163.

Alonso, J.L., Marcos, A., Suárez, A., 2009. Paleogeographic inversion resulting from large out of sequence breaching thrusts: The León Fault (Cantabrian Zone, NW Iberia). A new picture of the external Variscan Thrust Belt in the Ibero-Armorican Arc. Geologica acta: an international earth science journal 7, 451-474.

Ames, L.L., McGarrah, J.E., Walker, B.A., 1983a. Sorption of uranium and radium by biotite, muscovite and phlogopite. Clays and Clay Minerals 31, 343-351.

Ames, L.L., McGarrah, J.E., Walker, B.A., 1983b. Sorption of trace constituents from aqueous solutions onto secondary minerals II. Radium. Clays and Clay Minerals 31, 335-342.

Amponsah, P., Banoeng-Yakubo, B., Andam, A., Asiedu, D., 2008. Soil radon concentration along fault systems in parts of south eastern Ghana. J. Afr. Earth Sci. 51, 39-48.

Andeweg, B., 2002. Cenozoic tectonic evolution of the Iberian Peninsula: effects and causes of changing stress fields. PhD Thesis. Vrije Universiteit, Amsterdam,. 178 pp.

Angelier, J., 1994. Fault slip analysis and paleostress reconstruction, in: Hancock, P. (Ed.), Continental Deformation. Pergamon, Oxford, pp. 101-120.

Angelier, J., Mechler, P., 1977. Sur une méthode graphique de recherche des contraintes principales également utilisables en tectonique et en séismologie: la méthode des diédres droits. Bull. Soc. Géol. France VII, 1309-1318.

Antón, L., Muñoz-Martín, A., De Vicente, G., 2010. Alpine paleostress reconstruction and active faulting in western Iberia. Cent. Eur. J. Geosci. 2, 152-164.

Appleton, J.D., Miles, J.C.H., 2010. A statistical evaluation of the geogenic controls on indoor radon concentrations and radon risk. J. Environ. Radioact. 101, 799-803.

Arthaud, F., Matte, P., 1975. Les décrochements tardi-hercyniens du sud-ouest de l`Europe. Géometrie et essai de reconstitution des condition de la déformation. Tectonophysics 25, 139-171.

Bachmann, G.H., Voigt, T., Bayer, U., von Eynatten, H., Legler, B., Littke, R., 2008. Depositional history and sedimentary cycles in the Central European Basin System, in: Littke, R., Bayer, U., Gajewski, D., Nelskamp, S. (Eds.), Dynamics of Complex Intracontinental Basins - The Central European Basin System. Springer Verlag, Heidelberg, pp. 157-169.

Baldschuhn, R., Binot, F., Fleig, S., Kockel, F., 2001. Geotektonischer Atlas von Nordwest-Deutschland und dem deutschen Nordsee-Sektor. Geologisches Jahrbuch Reihe A, Heft 153, 3-95.

Bastida, F., Marcos, A., Pérez-Estaún, A., Pulgar, J.A., 1984. Geometría y evolución estructural del Manto de Somiedo. Bol. Inst. Geol. Min. Esp. 95, 517-539.

Baubron, J.-C., 1991. Soil gas emanations as precursory indicators of volcanic eruptions. J. Geol. Soc. Lond. 146, 571-576.

Baubron, J.-C., Rigo, A., Toutain, J.-P., 2002. Soil gas profiles as a tool to characterize active tectonic areas: the Jaut Pass example (Pyrenees, France). Earth Planet. Sci. Lett. 196, 69-81.

Baykulov, M., Brink, H.-J., Gajewski, D., Yoon, M.-K., 2009. Revisiting the structural setting of the Glueckstadt Graben salt stock family, North German Basin. Tectonophysics 470, 162-172.

Bense, V.F., Van den Berg, E.H., Van Balen, R.T., 2003. Deformation mechanisms in hydraulic properties of fault zones in unconsolidated sediments; the Roer Valley Rift System, The Netherlands. Hydrogeology Journal 11, 319-332.

Berger, P., 2011. Messungen natürlicher (geogener) elektromagnetischer Emissionen und ihre Aussagekraft bezüglich aktiver Horizontalspannungen in der Oberen Erdkruste im südlichen Kantabrischen Gebirge, Curueño- und Toriotraverse, Castilla y León, Spanien. Unpublished Diploma Thesis. Geologisch-Paläontologisches Institut, Universität Hamburg, Hamburg, 162 pp.

Bernard, P., 1992. Plausibility of long distance electrotelluric precursors to earthquakes. J. Geophys. Res. 97, 17531-17546.

Bernard, P., 2001. From the search of 'prescursors' to the research on 'crustal transients'. Tectonophysics 338, 225-232.

BGR, 2007. BGR Geologie: GK1000 Grundgestein und Deckschicht, Hannover.

Birke, M., Rauch, U., Lorenz, H., 2009. Uranium in stream and mineral water of the Federal Republic of Germany. Environ. Geochem. Hlth. 31, 693-706.

Bodrogi, E., Kovács, T., Jobbágy, V., Somlai, J., 2005. Application of MnO_2-coated discs in the case of the measurement of ^{226}Ra with alpha-spectrometric method. Radioprotection 40, S833-S837.

Boillot, G., 1986. Comparison between the Galicia and Aquitaine margins. Tectonophysics 129, 243-255.

Boillot, G., Capdevila, R., 1977. The Pyrenees: subduction and collision? Earth Planet. Sci. Lett. 35, 151-160.

Boillot, G., Malod, J., 1988. The north and north-west Spanish continental margin: A review. Rev. Soc. Geol. España 1, 295-316.

Boscov, M.E.G., Cunha, I.I.L., Saito, R.T., 2001. Radium migration through clay liners at waste disposal sites. Sci. Total Environ. 266, 259-264.

Bossew, P., 2003. The radon emanation power of building materials, soils and rocks. Appl. Radiat. Isot. 59, 389-392.

Bott, M.H.P., 1959. The mechanics of oblique slip faulting. Geol. Mag. 96, 109-117.

Bottrell, S.H., 1993. Redistribution of uranium by physical processes during weathering and implications for radon production. Environ. Geochem. Hlth. 15, 21-25.

Brace, W., Byerlee, J.D., 1966. Stick-slip as mechanism for earthquakes. Science 153, 990-992.

Breitkreuz, C., Geißler, M., Schneider, J., Kiersnowski, H., 2008. Basin initiation: Volcanism and sedimentation, in: Littke, R., Bayer, U., Gajewski, D., Nelskamp, S. (Eds.), Dynamics of Complex Intracontinental Basins - The Central European Basin System. Springer Verlag, Heidelberg, pp. 173-179.

Burton, M., Neri, M., Condarelli, D., 2004. High spatial resolution radon measurements reveal hidden active faults on Mt. Etna. Geophys. Res. Lett. 31, L07618.

Chinnery, M.A., 1966. Secondary faulting II. Geological aspects. Can. J. of Earth Sci. 3, 175-190.

Choukrone, P., 1992. Tectonic evolution of the Pyrenees. Annu. Rev. Earth Planet. Sci 20, 143-158.

Ciotoli, G., Etiope, G., Guerra, M., Lombardi, S., 1999. The detection of concealed faults in the Ofanto Basin using the correlation between soil-gas fracture surveys. Tectonophysics 301, 321-332.

Clamp, G.E., Pritchard, J., 1998. Investigation of fault position and sources of radon by measurement of ^{238}U decay series radionuclide activity in soil samples. Environ. Geochem. Hlth. 20, 39-44.

Clever, H.L. (Ed.) 1979. Krypton-, xenon-, radon gas solubilities. Solubility Data Series, Vol. 2 Pergamon Press, Oxford.

Cloetingh, S., Burov, E., Beekman, F., Andeweg, B., Andriessen, P.A.M., Garcia-Castellanos, D., De Vicente, G., Vegas, R., 2002. Lithospheric folding in Iberia. Tectonics 21, 1-26.

Cloetingh, S., Ziegler, P.A., Beekman, F., Andriessen, P.A.M., Matenco, L., Bada, G., Garcia-Castellanos, D., Hardebol, N., Dèzes, P., Sokoutis, D., 2005. Lithospheric memory, state of stress and rheology: neotectonic controls on Europe's intraplate continental topography. Quat. Sci. Rev. 24, 241-304.

Comte, P., 1959. Recherches sur les terrains anciens de la Cordillere Cantabrique. Mem. Inst. Geol. Min. España 60, 440 pp.

Cothern, C.R., Smith, J.E., 1987. Environmental Radon. Plenum Press, New York.

Crenshaw, W.B., Stoiber, N.B., Richard, E., 1982. Fault location by radon and mercury detection at an active volcano in Nicaragua. Letters to Nature 300, 345-346.

Crone, A.J., Machette, M.N., Bowman, J.R., 1997. Episodic nature of earthquake activity in stable continental regions revealed by paleoseismicity studies of Australian and North American Quaternary faults. Aust. J. Earth. Sci. 44, 203-214.

Darby, S., Hill, D., Auvinen, A., Barros-Dios, J.M., Baysson, H., Bchicchio, F., Deo, H., Falk, R., Forastiere, F., Hakama, M., Heid, I., Kreienbrock, L., Kreuzer, M., Lagarde, F., Mäkeläinen, I., Muirhead, C., Oberaigner, W., Pershagen, G., Ruano-Ravina, A., Ruosteenoja, E., Schaffrath Rosario, A., Tirmarche, M., Tomáscaron, L., Whitley, E., Wichmann, H.-E., Doll, R., (2005). Radon in homes and risk of lung cancer: collaborative analysis of individual data from 13 European case-control studies. Br. Med. J., 330, 223-227. doi: 10.1136/bmj.38308.477650.63.

De Sitter, L.U., 1962. The structure of the southern slope of the Cantabrian Mountains. Leidse Geol. Meded. 26, 255-264.

De Vicente, G., Vegas, R., Cloetingh, S., Munoz, A., Elorza, F.J., Sokoutis, D., Alvarez, J., Olaiz, A., 2005. The Cenozoic constrictive deformation of Iberia. Thrust and Foreland Basins, International Meeting, Rueil-Malmaison, Abstracts Volume, 117-119.

De Vicente, G., Cloetingh, S., Muñoz-Martín, A., Olaiz, A., Stich, D., Vegas, R., Galindo-Zaldívar, J., Fernández-Lozano, J., 2008. Inversion of moment tensor focal mechanisms for active stresses around the microcontinent Iberia: Tectonic implications. Tectonics 27, 1-22.

De Vicente, G., Vegas, R., 2009. Large-scale distributed deformation controlled topography along the western Africa-Eurasia limit: tectonic constraints. Tectonophysics 474, 124-143.

De Vicente, G., Cloetingh, S., Van Wees, J.D., Cunha, P.P., 2011. Tectonic classification of Cenozoic Iberian foreland basins. Tectonophysics 502, 38-61.

DeMets, C., Gordon, R.G., Argus, D.F., Stein, S., 1990. Current plate motions. Geophys. J. Int. 101, 425-478.

Dickson, B.L., 1990. Radium in groundwater, in: IAEA (Ed.), Technical Reports Series No.310, The Environmental Behaviour of Radium, Vol.1, IAEA, Vienna, pp. 335-372.

Dragović, S.D., Janković-Mandić, L.J., Dragović, R.M., Dorđević, M.M., Dokić, M.M., 2012. Spatial distribution of ^{226}Ra activity concentrations in well and spring waters in Serbia and their relation to geological formations. J. Geochem. Explor. 112, 206-211.

Dubois, G., 2005. An overview of radon surveys in Europe. EUR 21892 EN, EC, 168 pp.

Dubois, G., Bossew, P., Tollefsen, T., De Cort, M., 2010. First steps towards a European atlas of natural radiation: status of the European indoor radon map. J. Environ. Radioact. 101, 786-798.

Eikenberg, J., Tricca, A., Vezzu, G., Bajo, S., Ruethi, M., Surbeck, H., 2001. Determination of ^{228}Ra, ^{226}Ra and ^{224}Ra in natural water via adsorption on MnO_2 coated discs. J. Environ. Radioact. 54, 109-131.

Etiope, G., 1998. Transport of radioactive and toxic matter by gas microbubbles in the ground. J. Environ. Radioact. 40, 11-13.

Etiope, G., Lombardi, S., 1995. Evidence for radon transport by carrier gas through faulted clays in Italy. J. Rad. Nucl. Chem. 193, 291-300.

Etiope, G., Lombardi, S., 1996. Laboratory simulation of geogas microbubble flow. Environ. Geol. 27, 226-232.

Etiope, G., Martinelli, G., 2002. Migration of carrier and trace gases in the geosphere: An overview. Phys. Earth Planet. In. 129, 185-204.

Evans, D.G., Nunn, J.A., 1989. Free Thermohaline Convection in Sediments Surrounding a Salt Column. J. Geophys. Res. 94, 12413-12422.

Evers, H.J., 1967. Geology of the Leonides between the Bernesga and Porma rivers, Cantabrian Mountains, NW Spain. Leidse Geol. Meded. 41, 83-151.

Fagereng, A., Toy, V.G., 2011. Geology of the earthquake source: an introduction. Geological Society London, Special Publications 359, 1-16.

Fleischer, R.L., 1981. Dislocation Model for radon response to distant earthquakes. Geophys. Res. Lett. 8, 477-480.

Fleischer, R.L., Mogro-Campero, A., 1978. Mapping of integrated radon emanation for detection of long-distance migration of gases within the Earth: Techniques and principles. J. Geophys. Res. 83, 3539-3549.

Fleischer, R.L., Mogro-Campero, A., 1979. Radon enhancements in the earth: evidence for intermittent upflows? Geophys. Res. Lett. 6, 361-364.

Font, L., Baixeras, C., Moreno, V., Bach, J., 2008. Soil radon levels across the Amer fault. Radiat. Meas. 43, S319-S323.

Frissel, M.J., Köster, H.W., 1990. Radium in soil, in: IAEA (Ed.), Technical Reports Series No.310, The Environmental Behaviour of Radium, Vol.1, IAEA, Vienna, pp. 323-334.

Gallastegui, J., 2000. Estructura cortical de la cordillera y margen continental cantábricos: Perfiles ESCI-N. PhD Thesis. Trab. Geol. Univ. Oviedo 22, 9-234.

Gast, H., Stolz, W., 1982. Beziehungen zwischen meteorologischen Bedingungen und der Radonkonzentration von Bodenluft. Isotopenpraxis 18, 250-253.

Gates, A.E., Gundersen, L.C.S., Malizzi, L.D., 1990. Comparison of radon in soil over faulted crystalline terranes: glaciated versus unglaciated. Geophys. Res. Lett. 17, 813-816.

George, A.C., 2007. World history of radon research and measurement from the early 1900`s to today. Radon Bulletin. Conference of Radiation Control Program Directors, Inc. (CRCPD), Frankfort, Kentucky, 24 pp.

Ghosh, D., Deb, A., Sengupta, R., 2009. Anomalous radon emissions as precursor of earthquake. Journal of Applied Geophysics 69, 67-81.

Gómez-Escobar, V., Tomé, F.V., Lozano, J.C., 1999. Procedures for the determination of ^{222}Rn exhalation and effective ^{226}Ra activity in soil samples. Appl. Radiat. Isot. 50, 1039-1047.

González-Díez, A., Soto, J., Gómez-Arozamena, J., Bonachea, J., Martínez-Díaz, J.J., Cuesta, J.A., Olague, I., Remondo, J., Fernández Maroto, G., Díaz de Terán, J.R., 2009. Identification of latent faults using a radon test. Geomorphology 110, 11-19.

Greeman, D.J., Rose, A.W., 1996. Factors controlling the emanation of radon and thoron in soils of the eastern U.S.A. Chem. Geol. 129, 1-14.

Guerra, M., Lombardi, S., 2001. Soil-gas method for tracing neotectonic faults in clay basins: the Pisticci field (Southern Italy). Tectonophysics 339, 511-522.

Hauksson, E., 1981. Radon content of groundwater as earthquake precursor: evaluation of worldwide data and physical basis. J. Geophys. Res. 86, 9397-9410.

Heinicke, J., Koch, U., 2000. Slug flow - a possible explanation for hydrogeochemical earthquake precursors at Bad Brambach, Germany. Pure Appl. Geophys. 157, 1621-1641.

Hemleben, R., Reuther, C.-D., 1980. Allodapic limestones of the Barcaliente Formation (Namur A) between Luna and Cea Rivers (Southern Cantabrian Mountains, Spain). N. Jbuch. Geol. Pal. Abh. 159, 225-255.

Herraiz, M., de Vicente, G., Giner, J.L., Rodríguez-Pascua, M., Rincón, P., Lindo, R., Vadillo, O., Cabanas, L., Cicuéndez, J.I., Simón, J.L., Casas, A., Cortés, A., González-Casado, J.M., Rodríguez, C., Camacho, A., 1998. Proyecto SIGMA, Análisis del estado de esfuerzos tectónicos, reciente y actual en la Península Ibérica. Consejo de Seguridad Nuclear, Colección Otros Documentos CSN, Referencia ODE-04.05, 239 pp.

Herraiz, M., De Vicente, G., Lindo-Naupari, R., Giner, J., Simón, J.L., González-Casado, J.M., Vadillo, O., Rodríguez-Pascua, M.A., Cicuéndez, J.I., Casas, A., Cabanas, L., Rincón, P., Cortés, A.L., Ramírez, M., Lucini, M., 2000. The recent (upper Miocene to Quaternary) and present tectonic stress distribution in the Iberian Peninsula. Tectonics 19, 762-786.

Heward, A.P., Reading, H.G., 1980. Deposits associated with a Hercynian to late Hercynian Contintental strike-slip system, Cantabrian Mountains, Northern Spain. Spec. Publ. Int. Ass. Sediment 4, 105-125.

Hickman, S., Sibson, R., Bruhn, R., 1995. Introduction to special section: Mechanical involvement of fluids in faulting. J. Geophys. Res. 100, 12,831-12,840.

Hoeppener, R., 1955. Tektonik im Schiefergebirge. Geol. Rdsch. 44, 26-58.

Holub, R.F., Brady, B.T., 1981. The effect of stress on radon emanation from rock. J. Geophys. Res. 86, 1776-1784.

Huerta, A.D., Royden, L.H., Hodges, K.V., 1996. The interdependence of deformational and thermal processes in mountain belts. Science 273, 637-639.

IAEA, 2010. Analytical methodology for the determination of radium isotopes in environmental samples. IAEA/AQ/19, Analytical Quality in Nuclear Applications, International Atomic Energy Agency, Vienna, 2010, 59 pp.

ICRP, 1993. Protection Against Radon-222 at Home and at Work. ICRP Publication 65, Ann. ICRP 23 (2).

ICRP, 2007. The 2007 Recommendations of the International Commission on Radiological Protection. ICRP Publication 103, Ann. ICRP (2-4).

ICRP, 2009. International Commission on Radiological Protection: Statement on Radon. ICRP Ref/00/902/09, 44 pp.

Ielsch, G., Cushing, M.E., Combes, P., Cuney, M., 2010. Mapping of the geogenic radon potential in France to improve radon risk management: methodology and first application to region Bourgogne. J. Environ. Radioact. 101, 813-820.

Igarashi, G., Saeki, S., Takahata, N., Sumikawa, K., Tasaka, S., Sasaki, Y., Takahashi, M., Sano, Y., 1995. Ground-water radon anomaly before the Kobe earthquake in Japan. Science 269, 60-61.

IGME, 1981. Mapa Geológico de España, Boñar, 1:50 000.

Instituto Tecnológico GeoMinero de España, 1990. Mapa geológico de España, Riaño, 1:50 000.

Ioannides, K., Papachristodoulou, C., Stamoulis, K., Karamanis, D., Pavlides, S., Chatzipetros, A., Karakala, E., 2003. Soil gas radon: a tool for exploring active fault zones. Appl. Radiat. Isot. 59, 205-213.

Iyengar, M.A.R., 1990. The natural distribution of Radium, in: IAEA (Ed.), Technical Reports Series No.310, The Environmental Behaviour of Radium, Vol.1, IAEA, Vienna, pp. 59-128.

Jabaloy, A., Galindo-Zaldívar, J., González-Lodeiro, F., 2002. Palaeostress evolution of the Iberian Peninsula (Late Carboniferous to present-day). Tectonophysics 357, 159-186.

Jackson, M.P.A., Talbot, C.J., 1986. External shapes, strain rates, and dynamics of salt structures. Geol. Soc. Am. Bull. 97, 305-323.

Jackson, M.P.A., Vendeville, B.C., Schultz-Ela, D.D., 1994. Structural dynamics of salt systems. Annu. Rev. Earth Planet. Sci. 22, 93-117.

Jäger, N., 2011. Messungen natürlicher (geogener) elektromagnetischer Emissionen und Untersuchung ihrer Aussagekraft bezüglich aktiver Horizontalspannungen in der oberen Erdkruste im südlichen Kantabrischen Gebirge: Porma-Vorland Traverse, Provinz Castilla y León, Spanien. Unpublished Diploma Thesis. Geologisch-Paläontologisches Institut, Universität Hamburg, Hamburg, 142 pp.

Jaritz, W., 1980. Einige Aspekte der Entwicklungsgeschichte der nordwest-deutschen Salzstöcke. Z. dt. geol. Ges. 131, 387-408.

Jaworowski, Z., 1990. Sources and the global cycle of radium, in: IAEA (Ed.), Technical Reports Series No.310, The Environmental Behaviour of Radium, Vol.1, IAEA, Vienna, pp. 129-142.

Jensen, P.K., 1983. Calculations on the thermal conditions around a salt diapir. Geophys. Prospect. 31, 481-489.

Jönsson, G., 1995. Radon gas - where from and what to do? Radiat. Meas. 25, 1-4.

Jönsson, G., Baixeras, C., Devantier, R., Enge, W., Font, L., Freyer, K., Ghose, R., Treutler, H.C., 1999. Soil radon levels measured with SSNTD's and the soil radium content. Radiat. Meas. 31, 291-294.

Julivert, M., 1960. Estudio geológico de la cuenca de Beleno, Vallés altos del Sella, Ponga, Nalón y Esla, de la Cordillera Cantábrica. Bol. Inst. Geol. Min. Esp. 71, 364 pp.

Julivert, M., 1971. Décollement tectonics in the Hercynian Cordillera of NW Spain. Am. J. Sci. 270, 1-29.

Julivert, M., Truyols, J., Garcia-Alcalde, J., 1981. Mapa geológico de España 1:200.000, Síntesis de la cartografía existente, Mieres. IGME, pp. 1-54.

Keken, P.E., Spiers, C.J., Van den Berg, A.P., Muyzert, E.J., 1993. The effective viscosity of rocksalt: implementation of steady-state creep laws in numerical models of salt diapirism. Tectonophysics 225, 457-476.

Keller, G., Schneiders, H., Schütz, M., Siehl, A., Stamm, R., 1992. Indoor radon correlated with soil and subsoil radon potential - a case study. Environ. Geol. Water Sci. 19, 113-119.

Kemski, J., 1993. Radonmessungen in der Bodenluft zur Lokalisierung von Störungen im Neuwieder Becken (Mittelrhein), in: Meyer, W., Neugebauer, H., von Koenigswald, W., Hoernes, S., Höllermann, P.W. (Eds.), Bonner Geowissenschaftliche Schriften. PhD Thesis. Holos, Bonn, pp. 1-144.

Kemski, J., Klingel, R., Schneiders, H., Siehl, A., Wiegand, J., 1992. Geological structure and geochemistry controlling radon in soil gas. Radiat. Prot. Dosim. 45, 235-239.

Kemski, J., Klingel, R., Siehl, A., 1996a. Das geogene Radon-Potential, in: Siehl, A. (Ed.), Umweltradioaktivität. Ernst & Sohn, Berlin, pp. 179-222.

Kemski, J., Klingel, R., Siehl, A., 1996b. Classification and mapping of radon-affected areas in Germany. Environ. Int. 22, 789-798.

Kemski, J., Siehl, A., Stegemann, R., Valdivia-Manchego, M., 1999. Geogene Faktoren der Strahlenexposition unter besonderer Berücksichtigung des Radonpotenzials. Schriftenreihe Reaktorsicherheit und Strahlenschutz, BMU-1999-534, 133 pp.

Kemski, J., Siehl, A., Stegemann, R., Valdivia-Manchego, M., 2001. Mapping the geogenic radon potential in Germany. Sci. Total Environ. 272, 217-230.

Kemski, J., Klingel, R., Siehl, A., Stegemann, R., Valdivia-Manchego, M., 2002. Transferfunktion für die Radonkonzentration in der Bodenluft und der Wohnraumluft. Schriftenreihe Reaktorsicherheit und Strahlenschutz BMU-2002-598, 206 pp.

Kemski, J., Klingel, R., Stegemann, R., 2004. Validierung der regionalen Verteilung der Radonkonzentration in Häusern mittels Radonmessungen unter Berücksichtigung der Bauweise. BMU-2004-641, 77 pp.

Kemski, J., Klingel, R., Siehl, A., Valdivia-Manchego, M., 2009. From radon hazard to risk prediction-based on geological maps, soil gas and indoor measurements in Germany. Environ. Geol. 56, 1269-1279.

Khutorskoi, M., Teveleva, E., Tsybulya, L., Urban, G., 2009. Heat flow in salt-dome basins of Eurasia: A comparative study. Geotectonics 44, 289-304.

King, B.S., 1986. Gas geochemistry applied to earthquake prediction: an overview. J. Geophys. Res. 91, 12269-12281.

King, C.Y., 1978. Radon emanation on San Andreas Fault. Nature 271, 516-519.

King, C.-Y., 1993. Gas-Geochemical approaches to earthquake prediction. Proceedings of IAEA Meeting on isotopic and geochemical precursors of earthquakes and volcanic eruptions, Vienna, September 1991, pp. 22-37.

King, C.-Y., Minissale, A., 1994. Seasonal variability of soil-gas radon concentration in central California. Radiat. Meas. 23, 683-692.

King, C.Y., King, B.S., Evans, W.C., 1996. Spatial radon anomalies on active faults in California. Appl. Geochem. 11, 497-510.

Klusman, R.W., Webster, J.D., 1981. Preliminary analysis of meteorological and seasonal influences on crustal gas emission relevant to earthquake prediction. Bull. seism. Soc. Am. 71, 211-222.

Koike, K., Yoshinaga, T., Asaue, H., 2009. Radon concentrations in soil gas, considering radioactive equilibrium conditions with application to estimating fault-zone geometry. Environ. Geol. 56, 1533-1549.

Koopmans, B.N., 1962. The sedimentary and structural history of the Valsurvio Dome (Cantabrian Mountains, Spain). Leidse Geol. Meded. 26, 131-232.

Koroleva, M., Alt-Epping, P., Mazurek, M., 2011. Large-scale tracer profiles in a deep claystone formation (Opalinus Clay at Mont Russelin, Switzerland): Implications for solute transport processes and transport properties of the rock. Chem. Geol. 280, 284-296.

Kovach, E.M., 1945. Meteorological influences upon the radon-content of soil gas. EOS Trans., AGU, 26, 241-248.

Kozak, J.A., Reeves, H.W., Lewis, B.A., 2003. Modeling radium and radon transport through soil and vegetation. Journal of Contaminant Hydrology 66, 179-200.

Kozak, K., Swakoń, J., Paszkowski, M., Gradziński, R., Łoskiewicz, J., Janik, M., Mazur, J., Bogacz, J., Horwacik, T., Olko, P., Simopoulos, E.S., 2005. Correlation between radon concentration and geological structure of the Kraków area, Radioactivity in the Environment. Elsevier, pp. 464-469.

Kullmann, J., Schönenberg, R., 1978. Facies differentiation caused by wrench deformation along a deep-seated fault system (León Line, Cantabrian Mountains, north Spain). Tectonophysics 48, T15-T22.

Kraner, H.W., 1964. Measurements of the effects of atmospheric variables on Rn-222 flux and soil-gas concentration, in: Adams, J.A. (Ed.), The Natural Radiation Environment. University of Chicago Press, Chicago, pp. 191-215.

Krishnaswami, S., Seidemann, D.E., 1988. Comparative study of ^{222}Rn, ^{40}Ar, ^{39}Ar and ^{37}Ar leakage from rocks and minerals: Implications for the role of nanopores in gas transport through natural silicates. Geochim. Cosmochim. Acta 52, 655-658.

Kristiansson, K., Malmqvist, L., 1982. Evidence for non diffusive transport of 222 radon in the ground and a new physical model for the transport. Geophysics 47, 1444-1452.

Kristiansson, K., Malmqvist, L., 1984. The depth-dependence of the concentration of $^{222}_{86}Rn$ in soil gas near the surface and its implication for exploration. Geoexploration 22, 17-41.

Künze, N., Koroleva, M., Reuther, C.-D., 2012. ^{222}Rn activity in soil gas across selected fault segments in the Cantabrian Mountains, NW Spain. Radiat. Meas. 47, 389-399.

Langmuir, D., Riese, A.C., 1985. The thermodynamic properties of radium. Geochim. Cosmochim. Acta 49, 1593-1601.

Lehmann, R., Kemski, J., Siehl, A., Stegemann, R., 2001. Approach to identification of radon areas in Germany. Sci. Total Environ. 272, 213-215.

Lepvrier, C., Martínez-García, E., 1990. Fault development and stress evolution of the post-Hercynian Asturian Basin (Asturias and Cantabria, northwestern Spain). Tectonophysics 184, 345-356.

Liesa, C.L., Simón, J.L., 2009. Evolution of intraplate stress fields under multiple remote compressions: The case of the Iberian Chain (NE Spain). Tectonophysics 474, 144-159.

Lombardi, S., Voltattorni, N., 2010. Rn, He and CO_2 soil gas geochemistry for the study of active and inactive faults. Appl. Geochem. 25, 1206-1220.

López-Fernández, C., Pulgar, J.A., Glez.-Cortina, J.M., Gallart, J., Díaz, J., Ruíz, M., 2004. Actividad sísmica en el noroeste de la Península Ibérica observada por la red sísmica local del Proyecto GASPI (1999-2002). Trab. Geol. Univ. Oviedo 24, 91-106.

López-Fernández, C., Pulgar, J.A., Gallart, J., González-Cortina, J.M., Díaz, J., Ruíz, M., 2008. Zonación sismotectónica del NO de la Península Ibérica. Geo-Temas 10, 1031-1034.

Lotze, F., 1945. Zur Gliederung der Iberischen Meseta. Geotekt. Forsch. 6, 78-92.

Lyle, S., 2007. The geology of radon in Kansas. Kansas Geological Survey, Public Information Circular 25, 1-6.

Magri, F., Bayer, U., Clausnitzer, V., Jahnke, C., Diersch, H.J., Fuhrmann, J., Möller, P., Pekdeger, A., Tesmer, M., Voigt, H., 2005. Deep reaching fluid flow close to convective instability in the NE German basin - results from water chemistry and numerical modelling. Tectonophysics 397, 5-20.

Magri, F., Bayer, U., Pekdeger, A., Otto, R., Thomsen, C., Maiwald, U., 2009. Salty groundwater flow in the shallow and deep aquifer systems of the Schleswig-Holstein area (North German Basin). Tectonophysics 470, 183-194.

Malod, J.A., Mauffret, A., 1990. Iberian plate motions during the Mesozoic. Tectonophysics 184, 261-278.

Marcos, A., Pulgar, J.A., 1982. An approach to the tectonostratigraphic evolution of the Cantabrian foreland thrust and fold belt, Hercynian Cordillera of NW Spain. Neues Jahrb. Geol. Palaeontol. 163, 256-260.

Marín, J.A., Pulgar, J.A., Alonso, J.L., 1995. La deformación alpina en al Domo de Valsurvio (Zona Cantábrica, NO de Espana). Rev. Soc. Geol. España 8, 111-116.

Markkanen, M., Arvela, H., 1992. Radon emanation from soils. Radiat. Prot. Dosim. 45, 269-272.

Martinelli, G., 1993. Fluidodynamical and chemical features of radon 222 related to total gases: Implications for earthquake predictions. Proceedings of IAEA Meeting on isotopic and geochmical precursors of earthquakes and volcanic eruptions, Vienna, September 1991.

Maystrenko, Y., Bayer, U., Scheck-Wenderoth, M., 2005a. The Glueckstadt Graben, a sedimentary record between the North and Baltic Sea in north Central Europe. Tectonophysics 397, 113-126.

Maystrenko, Y., Bayer, U., Scheck-Wenderoth, M., 2005b. Structure and evolution of the Glueckstadt Graben due to salt movements. Int. J. of Earth Sci. 94, 799-814.

Maystrenko, Y., Bayer, U., Brink, H.-J., Littke, R., 2008. The Central European Basins System - an Overview, in: Littke, R., Bayer, U., Gajewski, D., Nelskamp, S. (Eds.), Dynamics of Complex Intracontinental Basins - The Central European Basin System. Springer Verlag, Heidelberg, pp. 15-34.

Maystrenko, Y., Bayer, U., Scheck-Wenderoth, M., Littke, R., 2010. Salt Movements within the Central European Basin System. Erdöl Erdgas Kohle 126, 156-163.

McGinnis, D.F., Schmidt, M., DelSontro, T., Themann, S., Rovelli, L., Reitz, A., Linke, P., 2011. Discovery of a natural CO_2 seep in the German North Sea: Implications for shallow dissolved gas and seep detection. J. Geophys. Res. 116, 1-12.

McKenzie, D.P., 1969. The relation between fault plane solutions for earthquakes and the directions of the principal stresses. Bull. seism. Soc. Am. 59, 591-601.

Megumi, K., Mamuro, T., 1974. Emanation and exhalation of radon and thoron gases from soil particles J. Geophys. Res. 79, 3357-3360.

Meier, G., 2003. Ingenieurgeologische Ergebnisse bei der Standsicherheitsanalyse der "Kalkberghöhle" in Bad Segeberg. Berichte von der 14. Tagung für Ingenieurgeologie, Kiel. Institut für Geowissenschaften, Kiel, 2003.

Menetrez, M.Y., Mosley, R.B., 1996. Evaluation of radon emanation from soil with varying moisture content in a soil chamber. Environ. Int. 22, 447-453.

Meschede, M., 1994. Methoden der Strukturgeologie. Enke Verlag, Stuttgart.

Mogro-Campero, A., Fleischer, R.L., 1977. Subterrestrial fluid convection: A hypothesis for long-distance migration of radon within the earth. Earth Planet. Sci. Lett. 34, 321-325.

Mogro-Campero, A., Fleischer, R.L., Likes, R.S., 1980. Changes in subsurface radon concentration associated with earthquakes. J. Geophys. Res. 85, 3053-3057.

Molinari, J., Snodgrass, W.J., 1990. The chemistry and radiochemistry of radium and the other elements of the uranium decay series, in: IAEA (Ed.), Technical Reports Series No.310, The Environmental Behaviour of Radium, Vol.1, IAEA, Vienna pp. 11-56.

Mollo, S., Tuccimei, P., Heap, M.J., Vinciguerra, S., Soligo, M., Castelluccio, M., Scarlato, P., Dingwell, D.B., 2011. Increase in radon emission due to rock failure: An experimental study. Geophys. Res. Lett. 38, 1-4.

Monnin, M., Seidel, J.L., 1991. Radon and Geophysics: Recent Advances. Nucl. Tracks Radiat. Meas. 19, 375-382.

Monnin, M.M., Seidel, J.L., 1992. Radon in soil-air and in groundwater related to major geophysical events: a survey. Nucl. Instr. and Meth. Phys. Res. A 314, 316-330.

Moore, W.S., Reid, D.F., 1973. Extraction of radium from natural waters using manganese-impregnated acrylic fibres. J. Geophys. Res. 78, 8880-8886.

Morawska, L., Phillips, C.R., 1993. Dependence of the radon emanation coefficient on radium distribution and internal structure of the material. Geochim. Cosmochim. Acta 57, 1783-1797.

Morawska, L., Jeffries, C., 1994. Distribution of radium in mineral sand grains and its potential effect on radon emanation. Radiat. Prot. Dosim. 56, 199-200.

Morvan, K., Andres, Y., Mokili, B., Abbe, J.-C., 2001. Determination of radium-226 in aqueous solutions by α-spectrometry. Anal. Chem. 73, 4218-4224.

Müller, B., Zoback, M.L., Fuchs, K., Mastin, L., Gregersen, S., Pavoni, B., Stephansson, O., Ljunggren, C., 1992. Regional patters of tectonic stress in Europe. J. Geophys. Res. 97, 11783-11803.

Müller-Hoeppe, N., Krone, J., Niehues, N., Raitz von Frentz, R., 2000. A new integrated approach to demonstrate the safe disposal of high-level radioactive waste and spent nuclear fuel in a geological repository. Proceedings of International Conference of the Safety of Radioactive Waste Management, Cordoba, Spain. IAEA-CN-78/85, 2000.

Muir Wood, R., 1994. Earthquakes, strain-cycling and the mobilization of fluids, in: Parnell, J. (Ed.), Geofluids: Origin, Migration and Evolution of Fluids in Sedimentary Basins. Geological Society Special Publication pp. 85-98.

Muñoz, J.A., Beaumont, C., Fullsack, P., Hamilton, J., 1996. Evolución del Pirineo central a partir de la comparación entre observaciones y modelos geodinámicos numéricos. Geogaceta 20, 454-457.

Nagihara, S., Sclater, H.G., Beckley, L.M., Behrens, E.W., Lawver, L.A., 1992. High heat flow anomalies over salt structures on the texas continental slope, Gulf of Mexico. Geophys. Res. Lett. 19, 1687-1690.

Nathwani, J.S., Phillips, C.R., 1979. Adsorption of ^{226}Ra by soils in the presence of Ca^{2+} ions. Specific Adsorption (II). Chemosphere 5.

Nazaroff, W.W., 1992. Radon transport from soil to air. Reviews of Geophysics 30, 137-160.

Nijman, W., Savage, J.F., 1989. Persistent basement wrenching as controlling mechanism of Variscan thin-skinned thrusting and sedimentation, Cantabrian Mountains Spain. Tectonophysics 169, 281-302.

Okabe, S., 1956. Time variation of the atmospheric radon content near the ground surface with relation to some geophysical phenomena. Memoirs of the College of Science, University of Kyoto, Series A 28, 99.

Olivet, J.L., Bonnin, J., Beuzart, P., Auzende, J.M., 1984. Cinématique de l`atlantique nord et central. Brest, Centre National pour l`Exploitation des Océans, Rapports scientifiques and techniques 54, 23-25.

Ortner, H., Reiter, F., Acs, P., 2002. Easy handling of tectonic data: the programs TectonicVB for Mac and TectonicsFP for WindowsTM. Comput. Geosci. 28, 1193-1200.

Papastefanou, C., 2010. Variation of radon flux along active fault zones in association with earthquake occurrence. Radiat. Meas. 45, 943-951.

Peacock, D.C.P., Marrett, R., 2000. Strain and stress: Reply. J. Struct. Geol. 22, 1369-1378.

Poliakov, A.N.B., Podladchikov, Y.Y., Dawson, E.C., Talbot, C.J., 1996. Salt diapirism with simultaneous brittle faulting and viscous flow, in: Alsop, G.I., Blundell, D.J., Davison, I. (Eds.), Salt tectonics. Geological Society Special Publication, pp. 291-302.

Pollard, D.D., Saltzer, S.D., 1993. Stress inversion methods: are they based on faulty assumptions? J. Struct. Geol. 15, 1045-1054.

Pulgar, J.A., Alonso, J.L., Espina, R.G., Marín, J.A., 1999. La deformación alpina en el basamento varisco de la Zona Cantabrica. Trab. Geol. Univ. Oviedo 21, 283-294.

Quindós, L.S., Fernandez, P.L., Soto, J., 1991. National survey on indoor radon in Spain. Environ. Int. 17, 449-453.

Quindós Poncela, L.S., Fernández Navarro, P.L., Gómez Arozamena, J., Ródenas Palomino, C., Sainz, C., Martin Matarranz, J.L., Arteche, J., 2003. Natural radiation exposure in the vicinity of spanish nuclear power stations. Health Phys. 61, 594-598.

Quindós Poncela, L.S., Fernández Navarro, P.L., Gómez Arozamena, J., Ródenas Palomino, C., Sainz, C., Martin Matarranz, J.L., Arteche, J., 2004a. Population dose in the vicinity of old Spanish uranium mines. Sci. Total Environ. 329, 283-288.

Quindós Poncela, L.S., Fernández, P.L., Gómez Arozamena, J., Sainz, C., Fernández, J.A., Suarez Mahou, E., Martin Matarranz, J.L., Cascón, M.C., 2004b. Natural gamma radiation map (MARNA) and indoor radon levels in Spain. Environ. Int. 29, 1091-1096.

Quindos, L.S., Fernández, P.L., Sainz, C., Gomez, J., Matarranz, J.L., Suarez Mahou, E., 2005. The Spanish experience on HBRA. Int. Congr. Ser. 1276, 50-53.

Rachkova, N.G., Shuktomova, I.I., Taskaev, A.I., 2010. The state of natural radionuclides of uranium, radium and thorium in soils. Eurasian Soil Science 43, 651-658.

Reid, H.F., 1911. The elastic-rebound theory of earthquakes. University of California Publications, Bulletin of the Department of Geology 6, 413-444.

Reijers, T.J.A., 1985. Evidence for strike-slip movement along the Sabero-Gordón and associated faults in the Luna-Porma area, León, NW Spain. Trab. Geol. Univ. Oviedo 15, 177-187.

Reuther, C.-D., 1977. Das Namur im südlichen Kantabrischen Gebirge (Nordspanien). Krustenbewegungen und Faziesdifferenzierungen im Übergang Geosynklinale-Orogen. Clausth. Geol. Abh. 28, 1-122.

Reuther, C.D., 2012. Grundlagen der Tektonik, Kräften und Spannungen der Erde auf der Spur. Spektrum-Akademischer Verlag, Heidelberg.

Richon, P., Klinger, Y., Tapponnier, P., Li, C.-X., Van Der Woerd, J., Perrier, F., 2010. Measuring radon flux across active faults: Relevance of excavating and possibility of satellite discharges. Radiat. Meas. 45, 211-218.

Richon, P., Perrier, F., Koirala, B.P., Girault, F., Bhattarai, M., Sapkota, S.N., 2011. Temporal signatures of advective versus diffusive radon transport at a geothermal zone in Central Nepal. J. Environ. Radioact. 102, 88-102.

Rigby, J.G., La Pointe, D.D., 1993. Wind and barometric pressure effects on radon in two mitigated houses. The 1993 International radon Conference, Denver, AARST, 61-68.

Ripa di Meana, C., 1990. Commission Recommendation of 21 February 1990 on the protection of the public against indoor exposure to radon. Euratom 90/143, Brüssel.

Roeloffs, E., 1999. Radon and rock deformation. Nature 399, 104-105.

Roest, W.R., Srivastava, S.P., 1991. Kinematics of the plate boundaries between Eurasia, Iberia, and Africa in the North Atlantic from the Late Cretaceous to the present. Geology 19, 613-616.

Rosenbaum, G., Lister, G.S., Duboz, C., 2002. Relative motions of Africa, Iberia and Europe during Alpine orogeny. Tectonophysics 359, 117-129.

Roure, F., Choukroune, P., Berastegui, X., Munoz, J.A., Villien, A., Matheron, P., Bareyt, M., Seguret, M., Camara, P., Deramond, J., 1989. Ecors deep seismic data and balanced cross sections: Geometric constraints on the evolution of the Pyrenees. Tectonics 8, 41-50.

Rupke, J., 1965. The Esla Nappe, Cantabrian Mountains (Spain). Leidse Geol. Meded. 32, 1-74.

Sainz, C., Dinu, A., Dicu, T., Szacsvai, K., Cosma, C., Quindós, L.S., 2009. Comparative risk assessment of residential radon exposures in two radon-prone areas, Ştei (Romania) and Torrelodones (Spain). Sci. Total Environ. 407, 4452-4460.

Sainz Fernandez, C., Quindós-Poncela, L.S., Fuente Merino, I., Arteche Garcia, J.L., Matarranz, L., Quindós Lopez, L., 2008. A brief history of radon measurements and remediation in Spain, Proceedings of the American Association of Radon Scientists (AARST) 2008, International Symposium, Las Vegas NV, United States.

Sannemann, D., 1968. Salt-stock families in northwestern Germany. AAPG Special Volumes M8: Diapirism and Diapirs, 264-270.

Sanz de Galdeano, C.M., 1996. Tertiary tectonic framework of the Iberian Peninsula, in: Friend, P.F., Dabrio, C.J. (Eds.), Tertiary basins of Spain. Cambridge University Press, Cambridge, pp. 9-14.

Scheck-Wenderoth, M., Lamarche, J., 2005. Crustal memory and basin evolution in the Central European Basin System - new insights from a 3D structural model. Tectonophysics 397, 143-165.

Scheck-Wenderoth, M., Maystrenko, Y., Hübscher, C., Hansen, M., Mazur, J., 2008. Dynamics of salt basins, in: Littke, R., Bayer, U., Gajewski, D., Nelskamp, S. (Eds.), Dynamics of Complex Intracontinental Basins - The Central European Basin System. Springer Verlag, Heidelberg, pp. 307-322.

Schery, S.D., Gaeddert, D.H., Wilkening, M.H., 1982. Transport of radon from fracturated rock. J. Geophys. Res. 87, 2969-2946.

Schmitz, J., 1984. Geotektonischer Atlas von NW-Deutschland Blatt Oldesloe C2326 und Lübeck C2330. BGR, 97179, Hannover.

Scholz, C.H., Sykes, L.R., Aggarwal, Y.P., 1973. Earthquake Prediction: A Physical Basis. Science 181, 801-810.

Segovia, N., 1991. Radon and volcanic activity: recent advances. Nucl. Tracks Radiat. Meas. 19, 409-413.

Segovia, N., Mena, M., Monnin, M., Pena, P., Seidel, J.L., Tamez, E., 1997. Radon-in-soil variations related to volcanic activity. Radiat. Meas. 28, 745-750.

Seminsky, K.Z., Bobrov, A.A., 2009. Radon activity of faults (western Baikal and southern Angara areas). Russ. Geol. Geophys. 50, 682-692.

Sibson, R., 1992. Implications of fault-valve behaviour for rupture nucleation and recurrence. Tectonophysics 211, 283-293.

Sibson, R.H., 1994. Crustal stress, faulting and fluid flow. Geological Society, London, Special Publications 78, 69-84.

Singh, M., Singh, N.P., Singh, S., Virk, H.S., 1986. Radon survey for uranium prospection using alpha detectors. International Journal of Radiation Applications and Instrumentation. Part D. Nuclear Tracks and Radiation Measurements 12, 879-882.

Sirocko, F., Szeder, T., Seelos, C., Lehne, R., Rein, B., Schneider, W.M., Dimke, M., 2002. Young tectonic and halokinetic movements in the North-German-Basin: its effect on formation of modern rivers and surface morphology. Geol.Mijnbouw - N. J. G. 81, 431-441.

Sjerp, N., 1967. The Geology of the San Isidro-Porma area (Cantabrian Mountains, Spain). Leidse Geol. Meded. 39, 55-128.

Smith, B., Amonette, A., 2006. The environmental transport of radium and plutonium: a review. Institute for Energy and Environmental Research (IEER), Takoma Park, MD. 20912. Technical Report, 1-31.

Soto, J., Fernández, P.L., Quindós, L.S., Gómez-Arozamena, J., 1995. Radioactivity in Spanish spas. Sci. Total Environ. 162, 187-192.

Spang, J.H., 1972. Numerical Method for Dynamic Analysis of Calcite Twin Lamellae. Geol. Soc. Am. Bull. 83, 467-472.

Sperner, B., Ratschbacher, L., Ott, R., 1993. Fault-striae analysis: A turbo pascal program package for graphical presentation and reduced stress tensor calculation. Comput. Geosci. 19, 1361-1388.

Sperner, B., Zweigel, P., 2010. A plea for more caution in fault-slip analysis. Tectonophysics 482, 29-41.

Spivak, A.A., Sukhorukov, M.V., Kharlamov, V.A., 2008. Pecularities of radon ^{222}Rn emanation with depth. Dokl. Earth Sci. 5, 823-826.

SSK, 2004. Auswertung der vorliegenden Gesundheitsstudien zum Radon, in: Strahlenschutzkommission (Ed.). Bundesanzeiger, Bonn.

Sugisaki, R., Anno, H., Adachi, M., Ui, H., 1980. Geochemical features of gases and rocks along active faults. Geochem. J. 14, 101-112.

Sundal, A.V., Henriksen, H., Lauritzen, S.E., Soldal, O., Strand, T., Valen, V., 2004. Geological and geochemical factors affecting radon concentrations in dwellings located on permeable glacial sediments - a case study from Kinsarvik, Norway. Environ. Geol. 45, 843-858.

Surbeck, H., 2000. Alpha spectrometry sample preparation using selectively adsorbing thin films. Appl. Radiat. Isot. 53, 97-100.

Surbeck, H., 2005. Dissolved gases as natural tracers in Karst hydrogeology; radon and beyond, Multidisciplinary Approach to Karstwater Protection strategy, Unesco Course, Budapest, Hungary.

Swakón, J., Kozak, K., Paszkowski, M., Gradzinski, R., Loskiewicz, J., Mazur, J., Janik, M., Bogacz, J., Horwacik, T., Olko, P., 2004. Radon concentration in soil gas around local disjunctive tectonic zones in the Krakow area. J. Environ. Radioact. 78, 137-149.

Szabo, Z., dePaul, V.T., Fischer, J.M., Kraemer, T.F., Jacobsen, E., 2012. Occurrence and geochemistry of radium in water from principal drinking-water aquifer systems of the United States. Appl. Geochem. 27, 729-752.

Tanner, A.B., 1964. Radon migration in the ground, in: Adams, J.A.S., Lowder, W.M. (Eds.), The natural radiation environment. University of Chicago Press, Chicago.

Tanner, A.B., 1980. Radon migration in the ground: A supplementary review, in: Gesell, T.F., Lowder, W.M. (Eds.), Natural Radiation Environment. III. Symp. Proc., Houston, Tex.

Tanner, A.B., 1986. Indoor radon and its sources in the ground. U.S. Geological Survey, Open-File Report 86-222, 1-5.

Tavani, S., Quintà, A., Granado, P., 2011. Cenozoic right-lateral wrench tectonics in the western Pyrenees (Spain): the Ubierna Fault System. Tectonophysics 509, 238-253.

Taylor, M.H., Dillon, W.P., Pecher, I.A., 2000. Trapping and migration of methane associated with the gas hydrate stability zone at the Blake Ridge Diapir: new insights from seismic data. Mar. Geol. 2000, 79-89.

Tikoff, B., Wojtal, S.F., 1999. Displacement control of geologic structures. J. Struct. Geol. 21, 959-967.

Torgersen, T., Benoit, J., Mackie, D., 1990. Controls on groundwater Rn-222 concentrations in fractured rocks. Geophys. Res. Lett. 17, 845-848.

Tuccimei, P., Mollo, S., Vinciguerra, S., Castelluccio, M., Soligo, M., 2010. Radon and thoron emission from lithophysae-rich tuff under increasing deformation: An experimental study. Geophys. Res. Lett. 37, 1-5.

Turner, F.J., 1953. Nature and dynamic interpretation of deformation lamellae in calcite of three marbles. Am. J. Sci. 251, 276-298.

Toutain, J.-P., Baubron, J.-C., 1999. Gas geochemistry and seismotectonics: A review. Tectonophysics 304, 1-27.

UNSCEAR, 1982. Ionizing radiation: Sources and biological effects. Annex D: Exposures to radon and thoron and their decay products.

USEPA, 2004. Understanding variation in partition coefficient, Kd, values, Volume III: Review of Geochemistry and Available Kd Values for Americium, Arsenic, Curium, Iodine, Neptunium, Radium and Technetium. EPA 402-R-04-002C, U.S. Environmental Protection Agency, Office of Radiation and Indoor Air, Washington D.C.

Vandenhove, H., Verrezen, F., Landa, E.R., 2010. Radium: Radionuclides. Encyclopedia of Inorganic Chemistry.

Van der Pluijm, B., 2011. Structural geology: Natural fault lubricants. Nature Geosci 4, 217-218.

Van der Voo, R., 1969. Paleomagnetic evidence for the rotation of the Iberian Peninsula. Tectonophysics 7, 5-56.

Van Gent, H., Back, S., Urai, J.L., Kukla, P., 2010. Small-scale faulting in the Upper Cretaceous of the Groningen block (The Netherlands): 3D seismic interpretation, fault plane analysis and regional paleostress. J. Struct. Geol. 32, 537-553.

Van Veen, J., 1965. The tectonic and stratigraphic history of the Cardano area, Cantabrian Mountains, northwest Spain. Leidse Geol. Meded. 35, 45-104.

Varhegyi, A., Hakl, J., Monnin, M., Morin, J.P., Seidel, J.L., 1992. Experimental study of radon transport in water as test for a transportation microbubble model. J. Appl. Geophys. 29, 37-46.

Vendeville, B.C., Jackson, M.P.A., 1992a. The rise of diapirs during thin-skinned extension. Marine and Petroleum Geology 9, 331-353.

Vendeville, B.C., Jackson, M.P.A., 1992b. The fall of diapirs during thin-skinned extensions. Marine and Petroleum Geology 9, 354-371.

Vergés, J., Fernández, M., Martínez, A., 2002. The Pyrenean orogen: pre-, syn-, and post-collisional evolution. Journal of the Virtual Explorer 8, 55-74.

Wallace, R.E., 1951. Geometry of shearing stress and relation to faulting. J. Geol. 59, 111-130.

Wanty, R.B., Johnson, S.L., Briggs, P.H., 1991. Radon-222 and its parent radionuclides in groundwater from two study areas in New Jersey and Maryland, U.S.A. Appl. Geochem. 6, 305-318.

Washington, J.W., Rose, A.W., 1992. Temporal Variability of Radon Concentration in the Interstitial Gas of Soils in Pennsylvania. J. Geophys. Res. 97, 9145-9159.

WHO, 2009. World Health Organisation (WHO). WHO Handbook on Indoor Radon: A Public Health Perspective. WHO Press, Geneva, 2009.

Wiederhold, H., Agster, G., Binot, F., Kirsch, R., 2003. Geophysical investigations on the connection between salt structures and aquifers in Schleswig-Holstein, in: Mares, S., Pospisil, L. (Eds.), Proceedings 9th Meeting Environmental and Engineering Geophysics: P-065, Prague.

Wiegand, J., 2001. A guideline for the evaluation of the soil radon potential based on geogenic and anthropogenic parameters. Environ. Geol. 40, 949-963.

Woodcock, N.H., Fischer, M., 1986. Strike-slip duplexes. J. Struct. Geol. 8, 725-735.

Yegorova, T., Maystrenko, Y., Bayer, U., Scheck-Wenderoth, M., 2008. The Glueckstadt Graben of the North-German Basin: new insights into the structure from 3D and 2D gravity analyses. Int. J. Earth Sci. 97, 915-930.

Yoon, M.-K., Baykulov, M., Dümmong, S., Brink, H.-J., Gajewski, D., 2008. New insights into the crustal structure of the North German Basin from reprocessing of seismic reflection data using the Common Reflection Surface stack. Int. J. Earth Sci. 97, 887-898.

Ziegler, P.A., 1982. Geological Atlas of Western and Central Europe. Shell Internationale Petroleum Maatschappij B.V., The Hague.

Zoback, M.L., 1992. First- and second-order patterns of stress in the lithospere: the World Stress Map Project. J. Geophys. Res. 97, 11703-11728.

Web references

Agencia Estatal de Meteorología (Aemet). URL: ftp://ftpdatos.aemet.es/series_climatologicas/valores_mensuales/annual/ (23.05.2011).

BFS, 2009: Bundesamt für Strahlenschutz. Gesundheitliche Auswirkungen von Radon in Wohnungen.URL: http://www.bfs.de/de/ion/wirkungen/radon_ges.html (10.04.2012).

Council directive (2011/0254); European Commission. URL: http://ec.europa.eu/energy/nuclear/radiation_protection/doc/com_2011_0593.pdf (03.05.2012).

IGN, 2011: Instituto Geográfico Nacional (IGN), Servicio de Información Sísmica. URL: http://www.ign.es/ign/layoutIn/sismoFormularioCatalogo.do (03.15.2012)

Ministerio de Medio Ambiente, Medio Rural y Marino (MARM): Sistema de Información Geográfica de Datos Agrarios (SIGA). URL: http://sig.marm.es/siga/ (03.05.2012)

San Francisco State University (SFSU), SFSU Creep Project Homepage. URL: http://funnel.sfsu.edu/creep/ (03.05.2012)

Figure Captions

Table Captions

Curriculum vitae

Nadine Künze

Born: 12.01.1981 in Freiburg im Breisgau

Address: Wohlwillstraße 14 Haus 3, 20359 Hamburg, Germany

E-Mail: nadine.kuenze@uni-hamburg.de

Education:

05/2009 – present	Research assistant, Geologisch-Paläontologisches Institut, University of Hamburg. **PhD thesis subject:** ^{222}Rn activity in soil gas as an indicator of active creep processes on geological faults
03/2009	Graduation (Diploma) **Diploma Thesis:** Mineralogical investigations on corundum and inclusions from Madagascar and Tansania.
10/2004 – 08/2005	Exchange student in Geology at “Universidad de Granada”, Granada, Spain
04/2002 – 03/2009	Studies of Geology and Paleontology (Diploma), University of Hamburg, Hamburg, Germany. Emphasis: Structural Geology and Mineralogy.
06/2000	Abitur at St. Ursula Gymnasium, Freiburg im Breisgau, Germany